# CRUSTAL AND UPPER MANTLE STRUCTURE OF OMAN AND THE NORTHERN MIDDLE EAST

A Dissertation

Presented to the Faculty of the Graduate School

of Cornell University

in Partial Fulfillment of the Requirement for the Degree of

Doctor of Philosophy

by

Ali Ibrahim Al-Lazki

January 2003

## BIOGRAPHICAL SKETCH

Ali Ibrahim Al-Lazki was born in December 12, 1969. In 1992 he graduated from Sultan Qaboos University, Sultanate of Oman, with a B. Sc. degree majoring in earth sciences and a minor in physics. After graduation he joined the Department of Earth Sciences in Sultan Qaboos University (SQU) as a demonstrator (teaching assistant) position. His main interest was to continue his education in the field of geophysics. In 1995, he finished his Masters degree in geophysics from the University of Tulsa, Oklahoma, USA, and went back to Oman to continue his teaching assistant job. Sultan Qaboos University was involved in a national project to establish earthquakes monitoring network. This was his first involvement with earthquakes and seismology. Convinced by his colleagues in the earthquake committee that there was a need for a seismologist to maintain the planned network, he thought of seismology as an option at that time. Thereafter, in 1997 Ali was accepted at Cornell University in a Ph.D. program in the field of Seismology/Geophysics.

*To my wife Asiya, my daughters Rayyan and Balqees,*

*and my larger family.*

*Thank you for your support.*

# ACKNOWLEDGMENTS

First of all, I would like to express my gratitude and thankfulness to my Committee chair (Muawia Barazangi), Dogan Seber (Committee member), and Eric Sandvol for their extended support and generosity in the long hours and efforts in bringing about this dissertation. I am thankful to my other committee members Larry Brown and William Philpot for their assistance throughout my studies at Cornell University. This research is also the result of the generous exchange of information and ideas from instructors and colleagues at the Department of Earth and Atmospheric Sciences at Cornell University. My sincere gratitude to the many people I met throughout my stay here at Cornell University and in other places who contributed in one way or another to this research. In particular, I am thankful to Weldon Beuchamp, Graham Brew, Carrie Brindisi, Alex Calvert, Khaled Al-Damegh, Francisco Gomez, George Hade, Steve Gallow, Christopher Harig, Matt Ricker, David Steer, Marisa Valve, and Aaron Wade. I am thankful to the Oman Ministry of Oil and Gas in allowing access to seismic and well data. Also thanks to Petroleum Development Oman for their assistance in obtaining the seismic reflection and well data. Special thanks to the Department of Minerals in the Oman Ministry of Commerce and Industry for their continuing support and providing Oman Geological Maps and other data. Special Thanks to Waris Warsi, Salam Al-Hashmi, and Khalfan Al-Tobi at the Oman Earthquake Observatory Center, Sultan Qaboos University, for their commitment in obtaining earthquake data from the four temporary stations in Oman. Thanks to Samir Hanna at the Department of Earth Sciences, Sultan Qaboos University, for his continuing support and help throughout my Ph.D. program here at Cornell University and in Oman.

I am grateful to the help and assistance of my colleagues at Bogazici University in Turkey: Niyazi Turkelli, Ekrem Zor, Tolga Bekler, and Sadi Kuleli. Thanks to the local and federal governments of Turkey for their help and assistance in the field work in eastern Turkey.

The research was funded partially by a scholarship from the Sultan Qaboos University, Sultanate of Oman, and partially was funded by the National Science Foundation (Grant No. EAR-9804780).

TABLE OF CONTENTS

LIST OF TABLES

LIST OF FIGURES

# CHAPTER ONE
# An Introduction

This dissertation focuses on studying the crustal structure on the southeast margin and foreland of Arabia in Oman, and upper mantle rheology and structure at the zone of interaction between the Arabian, Eurasian, and African plates (Figure 1.1). At the center of the study area, the Arabian plate is bounded in the east by the Indian plate along the Owen and Murray Transform Fault zones, in the northeast and north it is bounded by the Eurasian plate along the Zagros-Bitlis Suture zones, and in the west, northwest, and southwest it is bounded by the African plate along the Dead Sea Fault, the Red Sea, and the Gulf of Aden (Figure 1.1). Northwest of Arabia, the Hellenic and the Cyprean arcs define the convergence boundary between the African plate and the Anatolian plate in eastern Mediterranean Sea (Figure 1.1).

One of the most important events throughout geologic history of the region is the closure of the Neo-Tethys ocean. It began in Early Cretaceous along the eastern and northeastern boundaries of the Arabian-Africa Plate and lasted to Pliocene times (Sengor and Yilmaz, 1981). Ophiolite emplacement is a process that commonly accompanied the closure and subduction of the Neo-Tethys ocean. At present day a belt of Neo-Tethyan ophiolites follows the suture zone between the Arabian-Eurasian plate boundary and farther west within the Anatolian plate (Figure 1.1). While at the north and northeast boundaries of the Arabian plate the closure of the Neo-Tethys and final suturing processes have concluded and resulted in the building of the Iranian-Anaoltian plateaus, at the southeast Arabian plate boundary, a piece of the Neo-Tethys oceanic lithosphere (Semail Ophiolites) was emplaced in the late Cretaceous, but the closure process is still ongoing by subducting the remnant basin of Oman at the Makran Subduction zone (Figure 1.1).

**Figure 1.1**: A map showing simplified tectonic plate boundaries and major fault zones in the study area. Shown in two gray scale grades are ophiolites and basement outcrops. AP: Anatolian Plate, CA: Cyprean Arc, EAF: East Anatolian Fault, HA: Hellenic Arc, NAF: North Anatolian Fault.

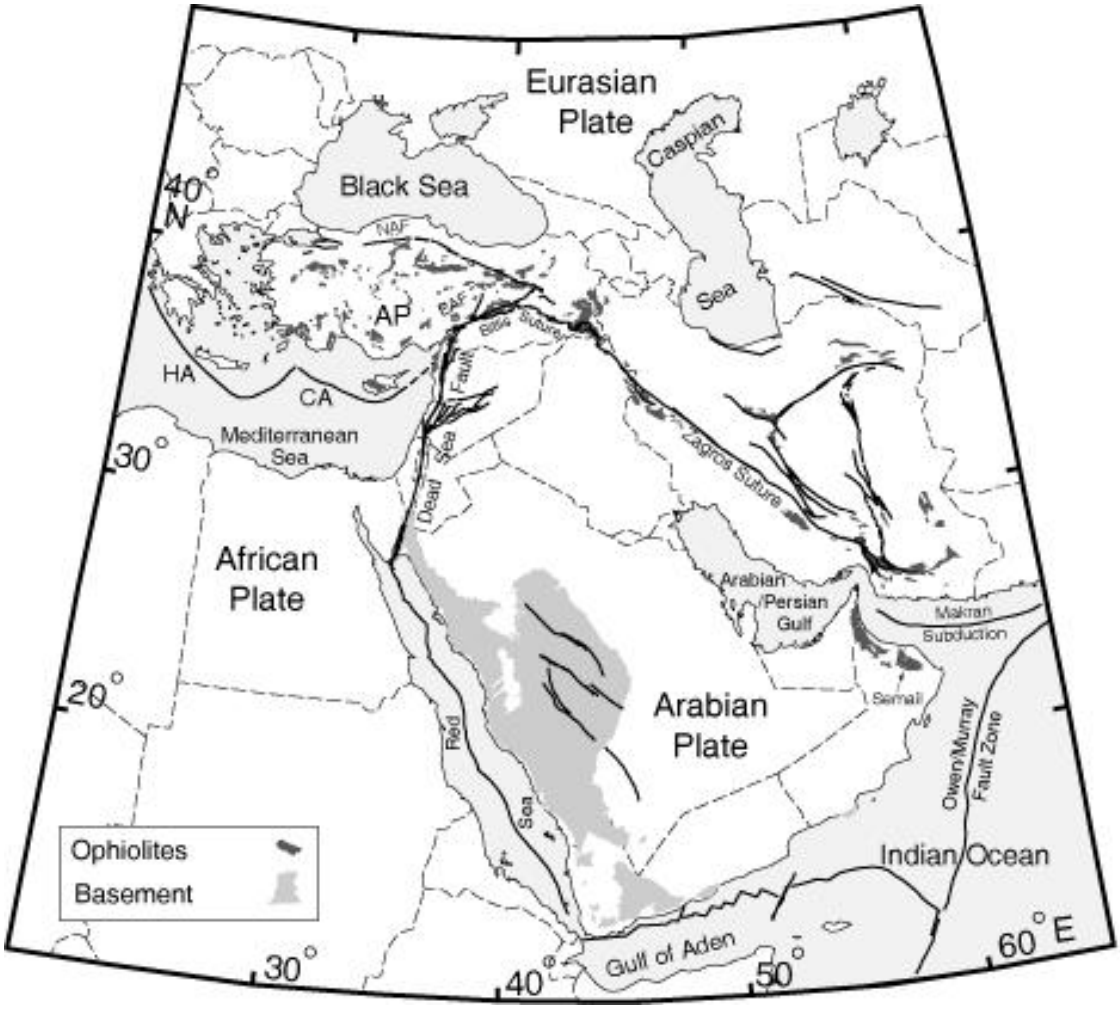
Eurasian Plate
Caspian Sea
Black Sea
40° N
NAF
AP
EAF
Bitlis Suture
HA
CA
Fault
Mediterranean Sea
30°
Dead Sea
Zagros Suture
African Plate
Arabian Persian Gulf
Makran Subduction
20°
Arabian Plate
Somali
Owen/Murray Fault Zone
Red Sea
Ophiolites
Basement
Indian Ocean
Gulf of Aden
30°
40°
50°
60° E

At a later stage, the opening of the Red Sea and Gulf of Aden is thought to have occurred episodically (Hempton, 1987). An initial phase occurring in the period Middle-Late Eocene and a later phase occurred in the Early Pliocene (~14.5 Ma) (Hempton, 1987). This separation of Arabia from Africa accommodated by the left lateral Dead Sea Fault System is thought to be responsible for the reorganization of relative plate motions in the Anatolian Plateau (Eurasian plate) (Sengor and Yilmaz, 1981). In early Pliocene, continued N-S convergence between Arabia and Eurasia resulted in the extrusion of an Anatolian plate along the North Anatolian Fault (NAF) and the East Anatolian Fault (EAF) zones (Bozkurt, 2001). The Anatolian plate's westward escape is converging along the Hellenic and Cyprean subduction zones, where Africa's oceanic lithosphere is being subducted.

Chapter two of this dissertation presents a detailed study of the crustal structure along 255 km long transect that includes the hinterland, the mountains, and the foreland of Oman. The main objective of this study is to investigate the crustal-scale structure of the eastern Arabian margin, across the 3,000 meters high Oman Mountains. Various geophysical and geological data are used to model the crustal thickness along the transect. We used exploration seismic and well data to constrain the upper 7-8 km of the sedimentary column, receiver function to infer Moho depth along the transect, and gravity modeling to constrain Moho lateral variations and infer a basement depths along the transect. Furthermore, integrated geological and geophysical data shed valuable information about the processes that accompanied the Semail Ophiolite emplacement.

Chapter three focuses on the young continent-continent collision zone between northern Arabia and Eurasia along the Bitlis-Zagros Suture zone. We use Pn tomography to further our knowledge about the mantle lithosphere rheology and structure and its contribution to lithosphere dynamics at the young Bitlis-Zagros

continent-continent collision zone. Pn velocities higher than 8 km/s are used to infer stable mantle lid, while Pn velocities less than 8 km/s are used to infer mantle lid instability.

Chapter four presents evidence on upper mantle rheology using Pn velocity and structure and using Pn anisotropy at the junction of the Arabian, Eurasian, and African plates. This research looks at the larger scale picture of the three plates' interactions and use Pn velocity and anisotropy to contrast regions underlain by stable mantle lid from those unstable and to investigate uppermost mantle processes. This study, also, focuses on regions underlain by small scale (< 200 km) very low Pn velocity anomalies that indicate thinned to absent mantle lid. This study compares Pn velocity with Sn attenuation map of the region. It also compares observed Pn azimuthal anisotropy with shear wave SKS polarization anisotropy to infer asthenospheric mantle deformation.

**REFERENCES**

Bozkurt, E. 2001. Neotectonics of Turkey - a synthesis. Geodinamica Acta : The Europian Journal of Geodynamics, v. 14, no. 1-3, p. 3-30.

Hempton, M.R. 1987. Constraints on Arabian plate motion and extensional history of the Red Sea. Tectonics, v. 6, no. 5, p. 687-705.

Sengor, A.M.C. and Y. Yilmaz 1981. Tethyan evolution of Turkey: a plate tectonic approach. Tectonophysics, v. 75, p. 181-241.

# CHAPTER TWO

# A Crustal Transect on the Southeast Arabian Margin Across the Oman Mountains*


## ABSTRACT

The unique tectonic setting of the Oman Mountains, the Semail Ophiolite, and the ongoing hydrocarbon exploration have led to extensive geological research focused on sedimentary units and ophiolite stratigraphy of Oman. Few studies, however, investigated the crustal-scale structure of the southeastern Arabian continental margin. Here we construct a NE-SW oriented crustal transect in the northern Oman Mountains across the Jabal Akhdar Mountain and the foreland region, covering a distance of 255 km. Along the transect the upper 8 km of the crust is primarily constrained using 152 km of 2-D seismic reflection profiles, 15 exploratory wells, and 1:100,000 to 1:250,000 scale geological maps. Seismic receiver function analysis of teleseismic earthquake waveform data produced by three temporary digital seismic stations provided the first reliable constraints on Moho depth beneath three locations along the transect. Bouguer gravity modeling was subsequently used to further interpret depth to Moho along the transect and depth to the metamorphic basement.

Four principal findings are documented. First, we interpret the presence of a mountain root beneath the Jabal Akhdar Mountain with a lateral extent of about 60 km along the transect. A Moho depth of 41-44 km was obtained ~25 km southwest of the Jabal Akhdar Mountain. The Moho depth increases to 48-51 km beneath the


*Published in part as Ali I. Al-Lazki, Dogan Seber, Eric Sandvol, and Muawia Barazangi, Institute for the Study of the Continents and Department of Earth and Atmospheric Sciences, Cornell University, Ithaca, New York, GeoArabia, Vol. 7, No. 1, 47-78, 2002, Gulf PetroLink, Bahrain.

northeastern limb of Jabal Akhdar Mountain and decreases to a depth of 39-42 km at ~25 km northeast of the Akhdar Mountain, in the coastal plains. Second, based on Bouguer gravity modeling, we infer an average of 9 km depth to the metamorphic basement in the core of the Jabal Akhdar Mountain and the area immediately southwest of the mountain. A relatively shallow depth to basement, 7-8 km, is found to coincide with Jabal Qusaybah south of the Hamrat Ad Duru range. Third, based on surface, subsurface and gravity modeling, the Nakhl Ophiolite block is found to extend beyond the shoreline for approximately 80 kilometers from its most southern surface outcrop. The Nakhl block averages in thickness ~5 km, whereas the ophiolite body south of the Jabal Akhdar Mountain is found to have a maximum thickness of 1 km. The underlying unit of the Hawasina sediments is found to average in thickness between 2-3 km in the Hamrat Ad Duru Zone and 2 km in the Coastal Zone. Finally, based on interpretation of seismic reflection profiles in the area southwest of Jabal Akhdar Mountain, we document the presence of NW-SE oriented, basement involved strike-slip faults deforming Miocene to Pliocene sediments.

## INTRODUCTION AND GEOLOGIC SETTING

The present-day Arabian Plate is surrounded by different types of known plate boundaries (Figure 2.1). In the west, a divergent boundary running south from the Gulf of Aqaba to the Red Sea and the Gulf of Aden marks stages of early continental rifting (Gulf of Aqaba) to the final stages of development of a mature oceanic lithosphere (southern Red Sea and Gulf of Aden). In the northwest, the Dead Sea transform fault system separates the Arabian Plate from the African Plate. The northern and the northeastern boundaries are continent-continent collision zones between the Arabian and the Eurasian plates forming the Bitlis and the Zagros sutures. The Zagros collision in the east continues south and transforms into a continent-

**Figure 2.1**: Map showing simplified plate boundaries surrounding the Arabian Plate. Green arrows represent plate motion relative to the nearest plate, and pink arrows represent absolute plate motion. (After Kensaku Tamaki, Ocean Research Institute, University of Tokyo, {http://manbow.ori.u-tokyo.ac.jp}).

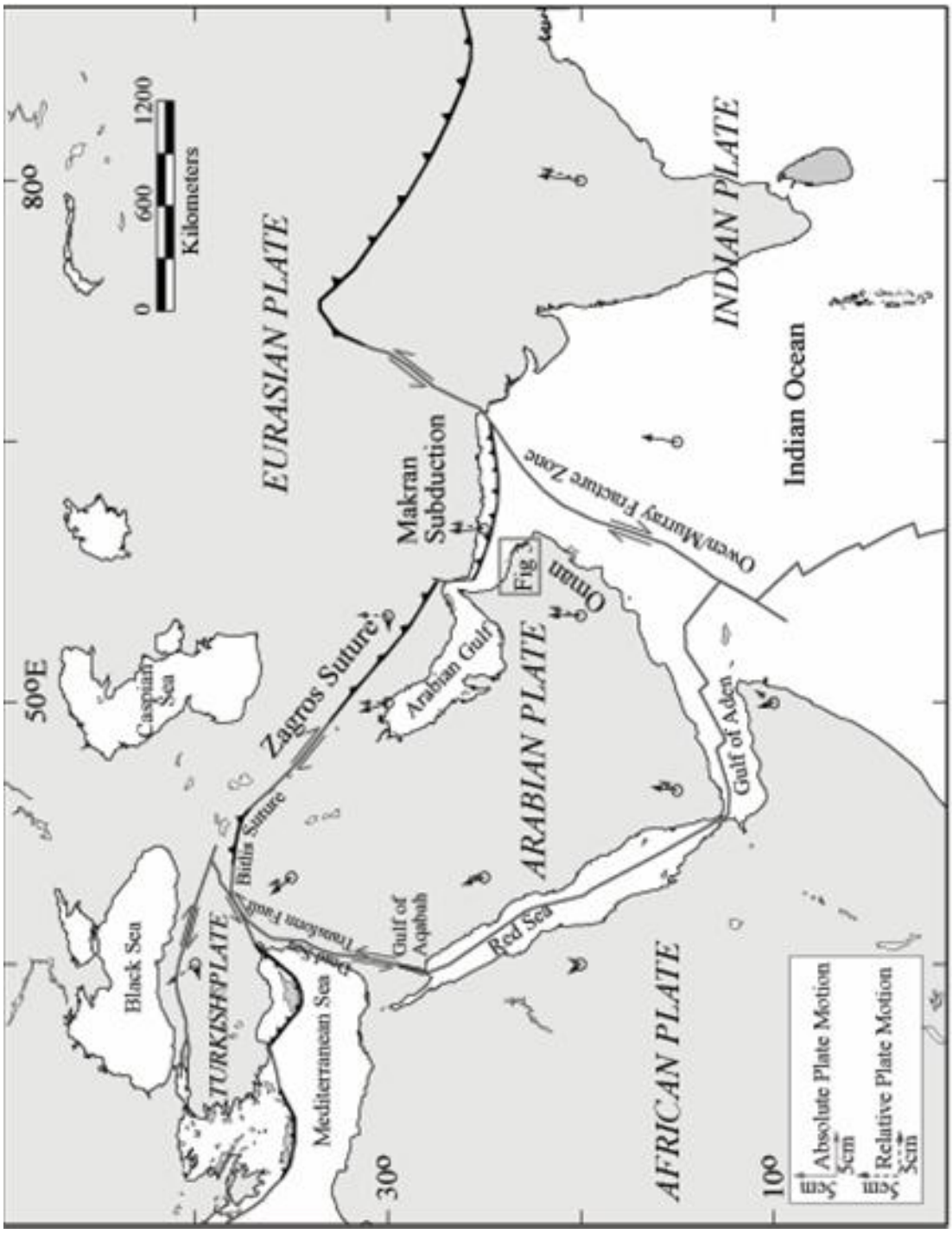
80°
0
600
1200
Kilometers
EURASIAN PLATE
INDIAN PLATE
Indian Ocean
Makran Subduction
Owen/Murray Fracture Zone
Fig. 3
Oman
50°E
Caspian Sea
Zagros Suture
Arabian Gulf
ARABIAN PLATE
Bitlis Suture
Black Sea
Transform Fault
Gulf of Aqabah
Red Sea
Gulf of Aden
Mediterranean Sea
TURKISH PLATE
AFRICAN PLATE
30°
10°
Absolute Plate Motion
3cm
Relative Plate Motion
3cm

oceanic subduction zone in the Makran subduction zone. The Owen and Murray transform faults mark the southeastern boundary of the Arabian plate that separate Arabia from the Indian Plate (Figure 2.1).

The study area is located in northern Oman and includes the southeastern margin and the foreland regions of the Arabian Plate. Tectonically, the most prominent feature along the southeastern Arabian margin is the Northern Oman Mountains, also known as the Hajar Mountains. The Northern Oman Mountains cover a length of ~700 km and vary between 40 to 130 km in width, with elevations up to 3000 meters above sea level.

Five tectonic sequences are recognized throughout the Oman region and are described below from the structurally lowest to the highiest sequence as shown in Figure 2.2. Rifting events initiated in the Precambrian/Cambrian, and the Early Permian periods started the development of two distinctive stratigraphic sequences: the pre-Permian Sequence (Late Proterozoic to Early Permian) made of alternations of clastics and carbonates, and the Hajar Supergroup (HSG) sequence (Late Permian-Mid Cretaceous), dominantly made of marine carbonates (Figure 2.2). The Late Cretaceous ophiolite emplacement is one of the most important tectonic events that affected the southeastern Arabian margin (Glennie et al., 1973; Boudier and Coleman, 1981; Coleman, 1981; Lippard, 1983). This tectonic event led to the emplacement of the Allochthonous Sequence; comprised of the Semail Ophiolite, with thickness of 10-12 km (Shelton, 1990) and deep oceanic and shallow marine sediments of the Hamrat Ad Duru and Sumeini Groups, respectively. The emplacement event is documented to span the period Cenomanian to Coniacian, (Hopson et al., 1981; Pallister and Hopson, 1981; Boudier et al., 1985; Nicolas et al., 1996; Searle and Cox, 1999). In this study, we refer to both the Hawasina and Sumeini Groups as the Hawasina Sediments. Lithologic units of the Muti Formation deposited in the period Turonian-

**Figure 2.2**: A Geologic column of the Oman Mountains and Interior Oman showing major sedimentary groups (e.g., Haima) and key formations names (e.g., Muti) in the region. The geologic column includes the major tectonic events that have affected the southeastern Arabian margin and the surrounding regions. (Modified from Le Metour et al. 1995).

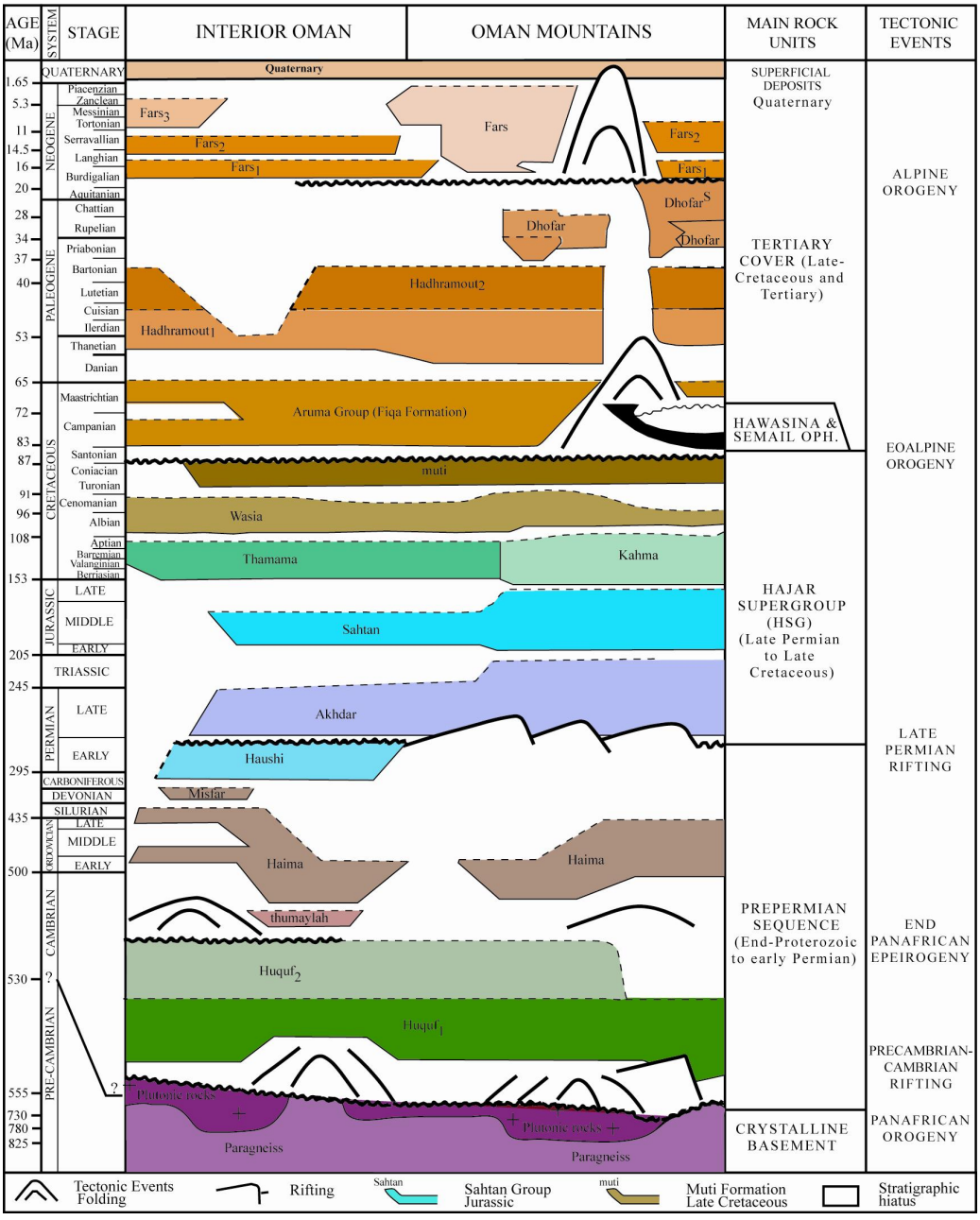
AGE (Ma)
SYSTEM
STAGE
INTERIOR OMAN
OMAN MOUNTAINS
MAIN ROCK UNITS
TECTONIC EVENTS
QUATERNARY
Quaternary
SUPERFICIAL DEPOSITS Quaternary
1.65
Piacenzian
5.3
Zanclean
Messinian
11
Tortonian
Serravallian
14.5
Langhian
16
Burdigalian
20
Aquitanian
NEOGENE
Fars3
Fars
Fars2
Fars1
ALPINE OROGENY
28
Chattian
34
Rupelian
37
Priabonian
40
Bartonian
Lutetian
Cuisian
53
Ilerdian
Thanetian
Danian
PALEOGENE
Dhofar
Dhofar S
Dhofar
TERTIARY COVER (Late-Cretaceous and Tertiary)
Hadhramout2
Hadhramout1
65
Maastrichtian
72
Campanian
83
Santonian
87
Coniacian
Turonian
91
Cenomanian
96
Albian
108
Aptian
Barremian
Valanginian
Berriasian
153
CRETACEOUS
Aruma Group (Fiqa Formation)
HAWASINA & SEMAIL OPH.
EOALPINE OROGENY
muti
Wasia
Thamama
Kahma
LATE
MIDDLE
EARLY
JURASSIC
Sahtan
HAJAR SUPERGROUP (HSG) (Late Permian to Late Cretaceous)
205
TRIASSIC
245
LATE
EARLY
PERMIAN
Akhdar
Haushi
LATE PERMIAN RIFTING
295
CARBONIFEROUS
DEVONIAN
SILURIAN
Misfar
435
LATE
MIDDLE
EARLY
ORDOVICIAN
Haima
Haima
500
CAMBRIAN
thumaylah
PREPERMIAN SEQUENCE (End-Proterozoic to early Permian)
END PANAFRICAN EPEIROGENY
530
?
Huqu$f_2$
Huqu$f_1$
PRECAMBRIAN-CAMBRIAN RIFTING
PRE-CAMBRIAN
?
555
Plutonic rocks
730
780
825
Plutonic rocks
Paragneiss
Paragneiss
CRYSTALLINE BASEMENT
PANAFRICAN OROGENY
Tectonic Events Folding
Rifting
Sahtan
Sahtan Group Jurassic
muti
Muti Formation Late Cretaceous
Stratigraphic hiatus

Coniacian/Santonian mark a transition from a passive continental margin to the foreland basin of Muti (Robertson, 1987; Bechennec et al., 1994). The syntectonic unit of Aruma Group (Fiqa Formation) deposited in the Campanian-Maastrichtian period (Bechennec et al., 1994) records the ophiolite advancement in the foreland region. In this study, we will consider the mapped Fiqa and Muti Formations separately when establishing stratigraphic relationships, and consider them jointly as the Aruma Group when establishing regional lateral continuity (Figures 2.2 and 2.4). Finally, the post emplacement period was followed by the deposition of the Tertiary Cover, which spans the Tertiary and the Quaternary period (Figure 2.2). The Tertiary period includes the Miocene Zagros collision event.

Two prominent domal structures are observed in the northern Oman Mountains: the Jabal Akhdar (JA), reaching an elevation of 3000 meters, and the Saih Hatat (SH) (Figure 2.3). The Jabal Akhdar and Saih Hatat provide a window to the stratigraphy of the Pre-Permian and the HSG Sequences. The structures of the JA and SH mountains received extensive investigations concerning timing and mechanism of deformation, and several alternative models have been proposed. One of the models is a fault-bend fold style of deformation responsible for the formation of Jabal Akhdar and Saih Hatat Mountains (e.g., Cawood et al., 1990; Hanna, 1990). However, the proposed geometry and the existence of the fault-bend fold are controversial. Mount et al. (1998) concluded that the Jabal Akhdar Mountain is the result of a compressional event that initiated in the Oligocene, involving a high angle reverse fault below the southern limb of the mountain, i.e., fault-propagation fold structure. Recently, LeMetour et al. (1995) concluded that the Late Permian rifting horst and graben structures at the continental shelf edge are possibly inherited in the structures of the Jabal Akhdar and Saih Hatat Mountains. In this study, we find that the structure of Jabal Akhdar Mountain cannot be described by a single deformation style or a

**Figure 2.3**: Topography map of the study area showing wells and seismic reflection lines (blue) locations (see Figure 2.1 for location). Shown in this map are the three structural zones: Coastal Zone, Hamrat Ad Duru Zone, and Interior Zone. The yellow triangles and circles show seismic station locations and the corresponding approximate Ps-Moho impingement location, respectively. Abbreviated text shown on map stands for the following names, SH: Saih Hatat, JQ: Jabal Qusaybah, JS: Jabal Salakh, JM: Jabal Madmar, JN: Jabal Nakhl, MFZ: Maradi Fault Zone, N: Natih structure, and F: Fahud structure. Base map is a shaded relief representation of topography data available at Cornell University.

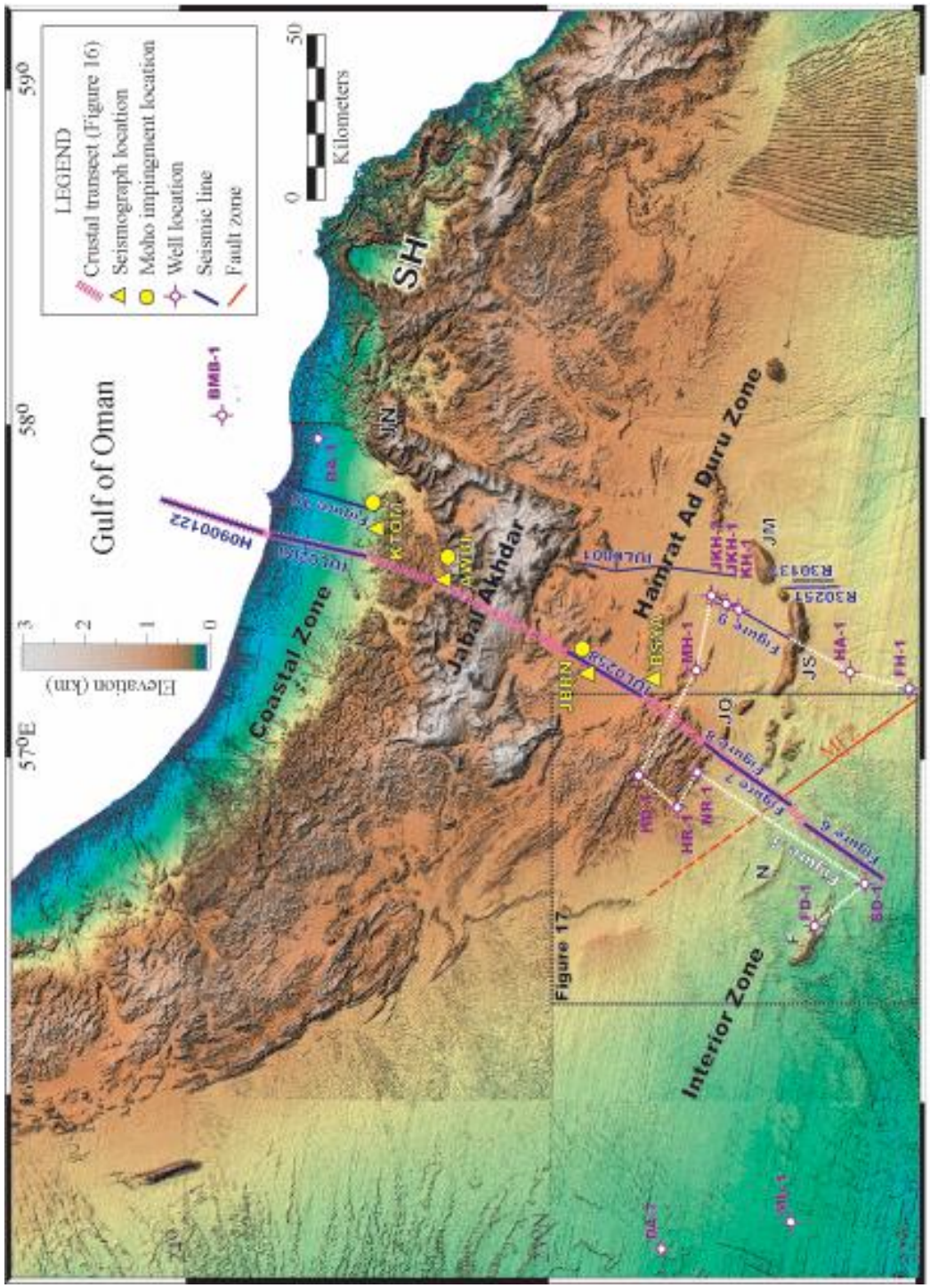
LEGEND
Crustal transect (Figure 16)
Seismograph location
Moho impingment location
Well location
Seismic line
Fault zone
0
50
Kilometers
Elevation (km)
3
2
1
0
57°E
58°
59°
Gulf of Oman
SMB-1
H09001Z2
Coastal Zone
Jabal Akhdar
Hamrat Ad Duru Zone
Interior Zone
SH
JN
JO
JS
JSI
JBEN
MWH
KTOT1
BSW1
JKH-1
KH-1
MH-1
HA-1
FH-1
HR-1
SD-1
JD-1
R30137
R30251
Figure 17

single event, but is rather an integration of multiple and different events that lead to the present-day structures.

A limited number of geophysical studies investigated the southeastern Arabian margin and continental crust in the Oman region. The study by Manghnani and Coleman (1981) estimated an average crustal thickness of ~40 km with a maximum thickness of ~43 km below the Saih Hatat Mountain based on 2-D Bouguer gravity modeling. Recent work by Ravaut (1997) and Ravaut et al. (1997a) estimated an average crustal thickness of ~43 km in the southeastern margin with a maximum crustal thickness of ~47 km beneath the northern Oman Mountains. The study was primarily based on Bouguer gravity modeling with limited subsurface information and constraints.

The main objective of this study is to construct a complete crustal-scale transect across the southeastern Arabian margin, the Oman Mountains, and the foreland region. The transect starts offshore in the coastal plains crossing the Jabal Akhdar Mountain and ends in the interior of Oman, southeast of Natih and Fahud structures (see Figure 2.3). The multidisciplinary approach we used in this study integrates data and results from three different methodologies: seismic reflection and well data interpretation, earthquake receiver function analysis, and Bouguer gravity modeling. We used 2-D seismic reflection profiles and well data to constrain the upper 8 km of the crust, the receiver function methodology to constrain Moho depth at three locations, and Bouguer gravity modeling to further constrain the lateral extent of Moho and infer depth to the metamorphic basement.

Along the transect, we divide the study area into four structural zones from north to south: (1) the Coastal Zone occupying the area north of Jabal Akhdar Mountain, on the coastal plains and the offshore region; (2) The Mountain Zone, which corresponds to the Jabal Akhdar Mountain; (3) the Hamrat Ad Duru Zone that

occupies the area directly south of Jabal Akhdar Mountain and shows the most significant surface deformation, within the Hawasina sediments; and (4) the Interior Zone which shows minimal surface deformation south of Jabal Qusaybah (see Figure 2.3). In this study, we also group the Interior and Hamrat Ad Duru Zones as the foreland region, and the Mountain and the Coastal Zones as the hinterland region.

## SEISMIC REFLECTION AND WELL ANALYSIS

### Data

Data used in seismic interpretation include a total of 152 km 2-D reflection profiles along the transect (Figure 2.3), 100 km of which are digital, and 52 km are analog paper copies. Seismic reflection data processing involved mainly depth conversion of the 2-D seismic profiles using stack and migration velocities. Stack and migration velocities were also used to perform line depth conversion on the analog data. A total of 15 exploratory wells were used to identify and correlate with stratigraphic units mapped in seismic reflection profiles (Figure 2.3). Well data included information on formations tops, age, lithology, and biostratigraphic descriptions prepared by different oil companies for exploration purposes. In this study, we used 100,000 and 250,000 scale geologic maps of Oman (Bechennec et al., 1986a, b; Beurrier et al., 1986; Chevrel et al., 1992; Rabu et al., 1986 Wyns et al., 1992) to construct a complete geologic cross section. These maps provided lithology, age, and most importantly dip information for the Jabal Akhdar Mountain, where no seismic or exploratory well information were available.

**Methodology**

Seismic reflection profiles directly along the transect provided the most complete coverage in the Interior and the Coastal Zones. Seismic correlation and interpretation provided important stratigraphic and structural relations of the HSG and the overlying sequences. Correlation of the pre-Permian Sequence was proceeded with limited confidence at time depths below 3 sec two way travel time (twt) that correspond approximately to the top of Huqf Group (Lower Cambrian). The top of metamorphic basement was almost impossible to identify in all seismic profiles in the Interior, the Hamrat Ad Duru, and the Coastal Zones. Depth converted time sections using interval stack and migration velocities showed in some cases a depth difference of ~200-300 meters at the 1 sec (twt) level, and deeper levels (Figure 2.4). We used well information whenever possible to correct the depth converted seismic sections, where wells intersected with seismic lines. In cases where wells did not intersect with a seismic line we made sure that the depth converted seismic section correlates with nearby wells and to wells across the transect. Along the entire transect only JKH-1, and SD-1 well data included sonic velocity information to ~1 km maximum depth (Figure 2.4). This deficiency restricted us from further comparing depth conversion velocities with well log sonic velocity data. DA-7 and ML-1 wells, located 50 km and 80 km, respectively, northwest of the transect, provided sonic velocity information for the entire HSG Sequence and were important in approximating depth conversion differences with the migration and stack velocities used in the study area (Figure 2.4). The sonic velocity of the upper "half" of the HSG Sequence shown in Figure 2.4, marked by the top of Natih and the base of Jurassic, is 4700 m/s and 5120 m/s for the DA-7, and ML-1 wells, respectively. This velocity discrepancy is attributed to lateral thickness variation of some lithologic units. The lower portion of the HSG Sequence,

**Figure 2.4**: Well log correlation diagram showing sonic velocity in solid black lines and interval seismic velocities in dashed blue lines. Seismic interval velocities overlain on SD-1 and JKH-2 are obtained from lines S50295, and IUL0001 (see Figure 2.3), respectively. Blue text is the averaged velocity for delineated intervals (see Figure 2.3 for location).

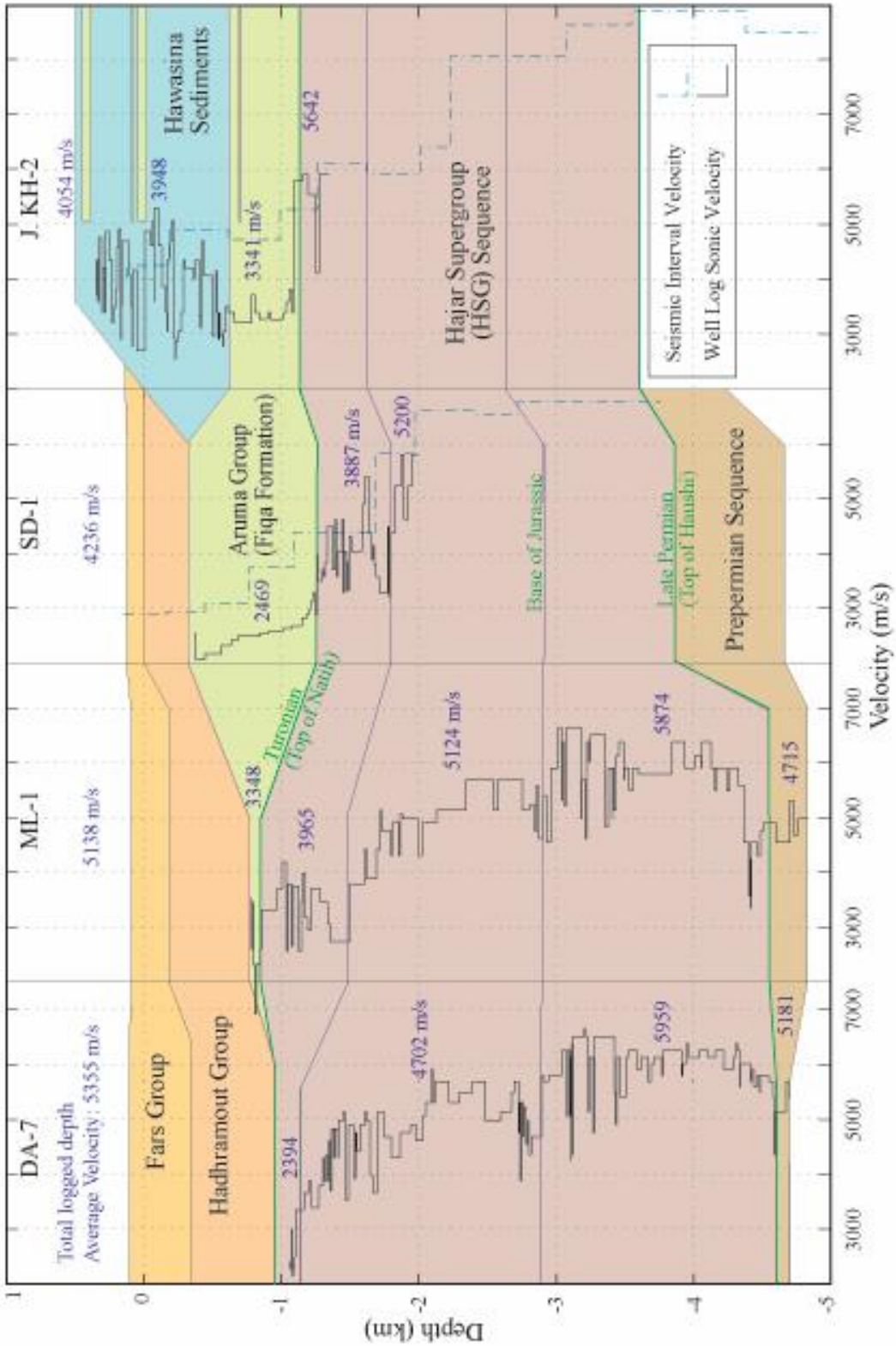
DA-7
Total logged depth
Average Velocity: 3355 m/s
ML-1
5138 m/s
SD-1
4236 m/s
J. KH-2
4054 m/s
Hawasina Sediments
3948
Fars Group
Hadhramout Group
Aruma Group (Fiqa Formation)
2469
3341 m/s
3642
Hajar Supergroup (HSG) Sequence
3887 m/s
5200
Base of Jurassic
Late Permian (Top of Haushi)
Prepermian Sequence
Turonian (Top of Natih)
3348
3965
5124 m/s
5874
4715
2394
4702 m/s
5959
5181
Seismic Interval Velocity
Well Log Sonic Velocity
Depth (km)
Velocity (m/s)

marked by base of Jurassic, and top of Haushi, for ML-1, and DA-7 wells, shows a small sonic velocity difference, with ~5900 m/s average sonic.

**Well Correlation**

Well data provided good lateral correlation for the HSG Sequence, the Aruma Group, the Tertiary Cover, and the Allochthonous Sequence in the foreland region (Figure 2.5). The Natih Formation (Albian) top delineates the top of HSG Sequence. The full thickness of the HSG Sequence is ~2.4 km (Figure 2.5) in the Hamrat Ad Duru Zone, at MH-1 well, and in the Interior Zone varied from ~2.6 km at FD-1/SD-1 well to ~2 km at FH-1. The tops of Haushi, Haima, and Huqf Groups that constitute the pre-Permian Sequence were penetrated in FD-1, and FH-1 wells (see Figures 2.5) in the foreland. In the foreland region the Aruma Group is identified in well data as the Fiqa Formation only, with no mention of the Muti Formation. Determined age of the Fiqa Formation in well data is the period Turonian-Maastrichtian, which includes the Muti Formation age mapped at the surface by Chevrel et al. (1992). In some well logs the Fiqa Formation is identified as the "Shargi shale member" and in others, simply as claystone lithology (HD-1, and MH-1). The Fiqa Formation thickness varies throughout the foreland region. It is thickest (1350 m) in the Hamrat Ad Duru Zone, at JKH-1 (Figure 2.5). The thickness of the Fiqa Formation averages 595 m along the correlation section of the wells HD-1, MH-1, and JKH-2 shown in Figure 2.5. However, the thickness of the Fiqa Formation in JKH-1 and KH-1 is twice (1284 m) that observed in the latter three wells (Figure 2.5). The considerable variation of Fiqa thickness in such a short distance could be attributed to either localized structural thickening of the unit in JKH-1 and KH-1, possibly by reverse faulting, or possible misidentification of the Fiqa Formation with the Hawasina Sediments. The Hawasina

**Figure 2.5**: Fence diagram showing correlation of the Hajar Supergroup (HSG) Sequence in the Interior and Hamrat Ad Duru Zones (see Figure 2.3 for location). Red lines represent correlation between units within the HSG Sequence, and blue line marks the top of Aruma Group (Muti and Fiqa Formations). Age and stratigraphic identification is based on interpretation of oil exploration companies. Defined groups (GP) and correlated formations are after Le Metour et al. (1995), Pratt and Smewing (1990), Rabu et al. (1990), and Nolan et al. (1990).

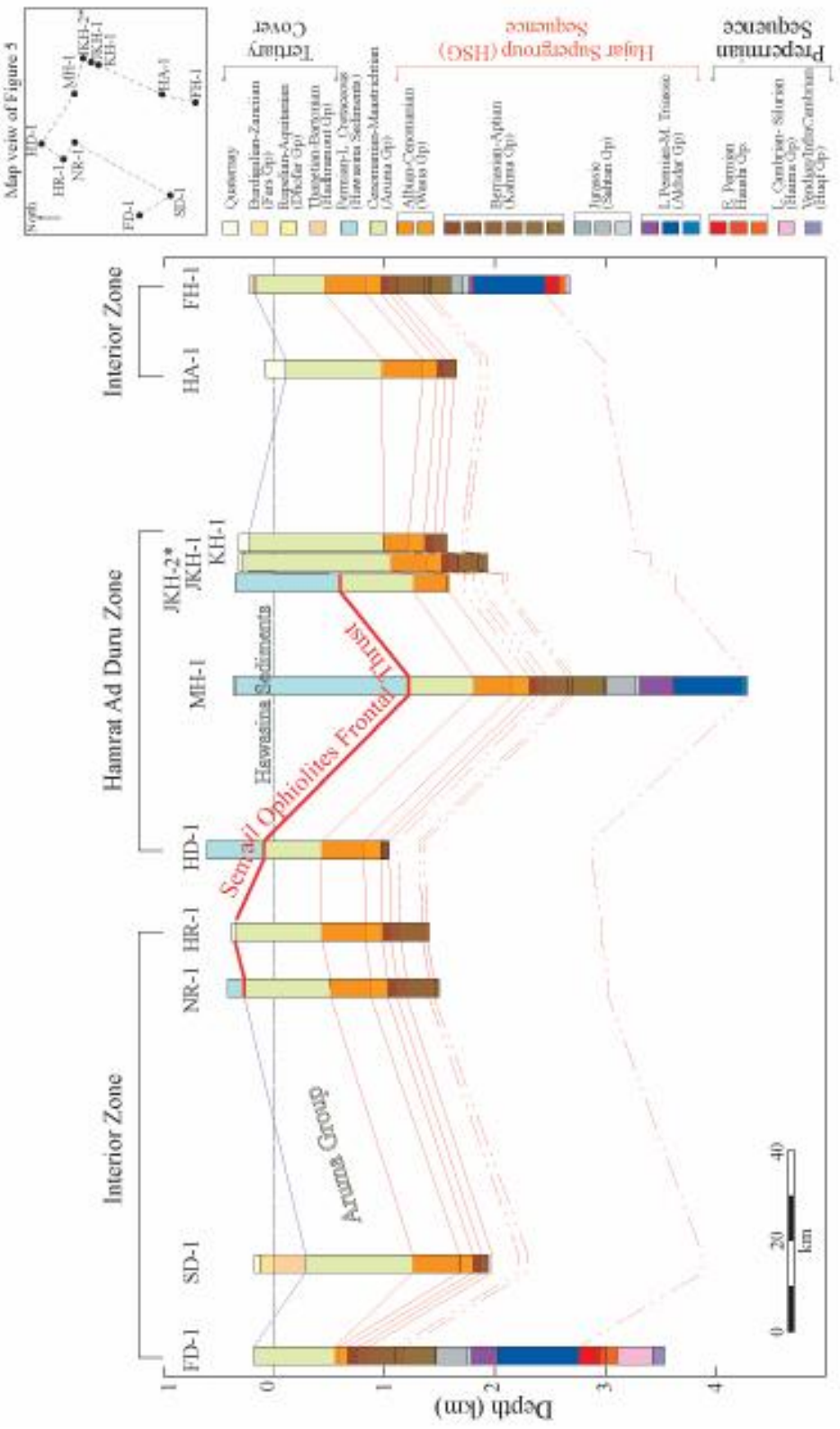
Map view of Figure 3
North
FD-1
HD-1
HR-1
NR-1
MH-1
JKH-2*
JKH-1
KH-1
SD-1
HA-1
FH-1
Tertiary Cover
Quaternary
Dariyalian-Zanclean (Fars Gp)
Rupelian-Aquitanian (Ghidar Gp)
Thanetian-Bartonian (Hadrumaut Gp)
Permian-L. Cretaceous (Haushi Sediments)
Cenomanian-Maastrichtian (Aruma Gp)
Albian-Cenomanian (Wasia Gp)
Barremian-Aptian (Kahmah Gp)
Jurassic (Sahtan Gp)
L.Permian-M. Triassic (Akbar Gp)
U. Permian (Haushi Gp)
L. Cambrian- Silurian (Haima Gp)
Vendian/Infra-Cambrian (Huqf Gp)
Thick Supergroup (HSG) Sequence
Pre-cratonian Sequence
Interior Zone
Hamrat Ad Duru Zone
Interior Zone
FD-1
SD-1
NR-1
HR-1
HD-1
MH-1
JKH-2*
JKH-1
KH-1
HA-1
FH-1
Haushi Sediments
Aruma Group
Semail Ophiolites Frontal Thrust
Depth (km)
0
1
2
3
4
0
20
40
km

Sediments directly overlie the Aruma Group, and are found to occur primarily in the Hamrat Ad Duru Zone (Figure 2.5). The Hawasina Sediments are shown to extend to NR-1 location (see Figure 2.5) with a thickness of 154 m, located at the boundary of the Hamrat Ad Duru and the Interior Zone (Figure 2.5). The Hawasina Sediments are made of imbricate stacks of alternating sheets of overthrusted sheets of Guwayza sandstone and limestone members, and thrusted sheets of the underlying Aruma Group (Robertson, 1987). For the purpose of sequence correlation we have cumulatively included the thickness of thrusted sheets of Aruma Group with its *in situ* thickness (Figure 2.5). Well data in the Hamrat Ad Duru Zone do not include the Tertiary Cover Sequence and only SD-1 and FH-1 in the Interior Zone includes sediments of the Tertiary Cover Sequence.

Fewer exploration wells have been drilled in the Coastal Plains and the offshore area. BA-1 and BMB-1 (see Figure 2.3 for location) are the only well data available to us in the coastal and offshore areas. BA-1 located ~30 km east of the transect penetrates the basal parts of the Hadhramout Group (Thanetian-Bartonian) at a maximum depth of 2448 m. Northeast of BA-1 well, BMB-1 well reaches a maximum depth of 4631 m. BMB-1 location and lateral structural complexity prohibited its projection to our transect. It is noteworthy that the BMB-1 well penetrates units of shale, marly sand, and shalely marl deposited in the period Massrtichtian-Campanian equivalent to the Alkhawd Formation. The Alkhawd Formation equivalent in BMB-1 well is 1195 m thick, overlain by only 305 m Eocene age Hadhramout Group, which is thinner than its equivalent in BA-1 well (1200 m).

## Seismic Interpretation

### *Interior Zone: Line S50295*

The upper 1s (twt) of line S50295 includes the Tertiary Cover Sequence and the Aruma Group (Fiqa and Muti Formations) overlying the HSG Sequence (Figure 2.6). In this 2-D reflection profile, as well as other profiles the top of the Muti Formation is inferred by downlapping reflectors of the overlying Fiqa Formation. The downlapping reflectors provide a structural relationship between the interpreted Muti Formation and the Fiqa Formation, and not a distinctive chronostratigrphy of the Muti Foramtion. In line S50295 the Fiqa Formation shows a SW reflector progradation, onlapping the top of Muti Formation. The green reflector at ~200 ms (twt) marks the termination of prograding reflectors, overlain by conformable strata of the Tertiary Cover (Figure 2.6). Generally, the Aruma Group is shown to thicken towards the NE, but the basal Muti Formation is interpreted to thicken towards the SW.

A system of negative flower structures is observed in line S50295 and other 2-D seismic profiles throughout the Interior Zone, and in some parts of Hamrat Ad Duru Zone. The flower structures in line S50295 exhibit minimal vertical displacement with subtle reflector offsets at the top of the Natih Formation, and gentle folding of the overlying layers of the Aruma Group and the Tertiary Cover (Figure 2.6). Below ~2 s (twt) the flower structures converge to a single steep fault that is shown to offset the tops of Haushi Group (Late Permian) and Huqf Group (Lower Cambrian) marker reflectors (Figure 2.6). Fault continuity or surface exposure, especially for the two flower structures in the NE portion of the profile is obscured within the Fiqa Formation. Alternatively, the fault tips may be within the Fiqa shales and did not cross into the Tertiary. However, the base of Tertiary Cover reflector (green), Hadhramout Group (Paleocene) does show gentle folding near the surface shown in Figure 2.6.

**Figure 2.6**: Interpretation of a migrated 2-D seismic reflection profile (see Figure 2.3 for location). Red lines are inferred normal faults with possible continuation shown as dashed lines. The normal faulting system form negative flower structures that offset reflectors below 3 seconds. These flower structures are associated with a wrench faulting system observed in the foreland region. The upper one second of the section shows reflectors of the Fiqa Formation onlapping southwestward. The orange colored solid line represents the top of Hajar Supergroup Sequence and MPLF corresponds to Miocene-Pliocene Fars Group.

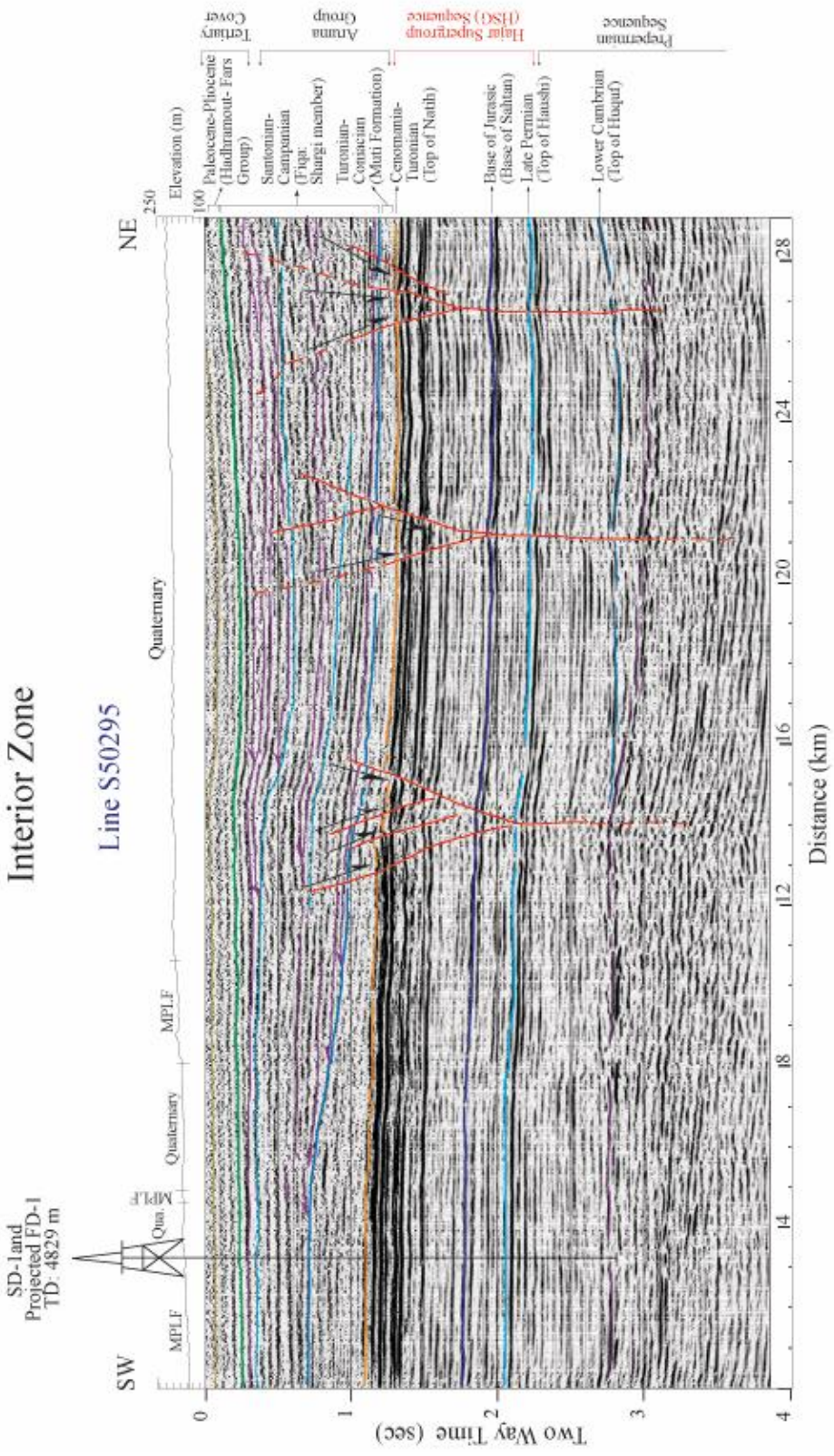
Interior Zone
Line S50295
SW
NE
SD-1 and
Projected FD-1
TD: 4829 m
MPLF
Qtna.
Quaternary
MPLF
Quaternary
MPLF
Elevation (m)
250
100
Paleocene-Pliocene
(Hadhramout- Fars
Group)
Santonian-
Campanian
(Fiqa:
Shargi member)
Turonian-
Coniacian
(Muti Formation)
Cenomanian-
Turonian
(Top of Natih)
Base of Jurassic
(Base of Sahtan)
Late Permian
(Top of Haushi)
Lower Cambrian
(Top of Huqf)
Tertiary
Cover
Aruma
Group
Haja Supergroup
(HSG) Sequence
Pregerman
Sequence
0
1
2
3
4
Two Way Time (sec)
14
16
18
120
124
128
Distance (km)

***Interior Zone: Line S50274***

In line S50274 (Figure 2.7) the distinctive reflector marker of the top of Natih Formation and the top of Haushi Group are shown to clearly delineate the HSG Sequence. The Muti Formation top is interpreted at ~0.9 s (twt) level in the NE end of line S50274 and at ~1.35 s in the SW. Hanna and Nolan (1989) interpreted the Maradi Fault Zone (MFZ) as a right lateral strike slip fault reactivated in the Pliocene-Pliestocene times. In line S50274 we interpret the MFZ as basement associated, right lateral strike-slip fault that includes a reverse component (Figure 2.7). The reverse component is inferred from 0.35-0.4 s (~900 m) time difference of the Natih reflector marker between the NE and SW sides of the MFZ (Figure 2.7). The center of the structure between 2 to 6 km distance shows internal collapse, possibly by normal faulting, towards the center of the structure (Figure 2.7). In line S50274, note that the NE arm of the triangular zone of the MFZ separates surface outcrops of Fiqa Formation in the NE from the outcropping, southward steeply dipping ($72^{O}$), Umm Er Radhuma Formation and the Berzman Formation (Tertiary Cover Sequence) (Figure 2.7). It is important to note the relative thickness of the Aruma Group and the Tertiary Cover in the SW side of the MFZ is ~1.6 s (twt), compared to the NE side of the MFZ where Fiqa Formation is found have a thickness ~1.2 (twt). In the SW, the thickness of the Aruma Group and the Tertiary Cover is correlated with the thickening observed at the NE end of above interpreted line S50295 (1.3 s). Therefore, we interpret the MFZ to include a reverse faulting component, possibly related to the earlier Late Cretaceous emplacement process. Later the deformed zone was followed by a transtensional event, strike slip faulting, in the Pliocene-Pliestocene as dated by Hanna and Nolan (1989).

**Figure 2.7**: (a) A migrated 2-D seismic reflection profile of line S50274 crossing the Maradi Fault Zone. The fault zone includes two styles of deformation: a strike slip component (a flower structure) and a reverse component inferred from the depth difference of the Natih Formation (orange line) reflector across the fault zone (see Figure 2.3 for location). (b) A line interpretation of S50274 line showing relative motion within the Maradi Fault Zone and marker reflectors. Abbreviated text MPlbz and Eur stands for Miocene-Pliocene Berzman Formation and Eocene Um Er Radhuma Formation.

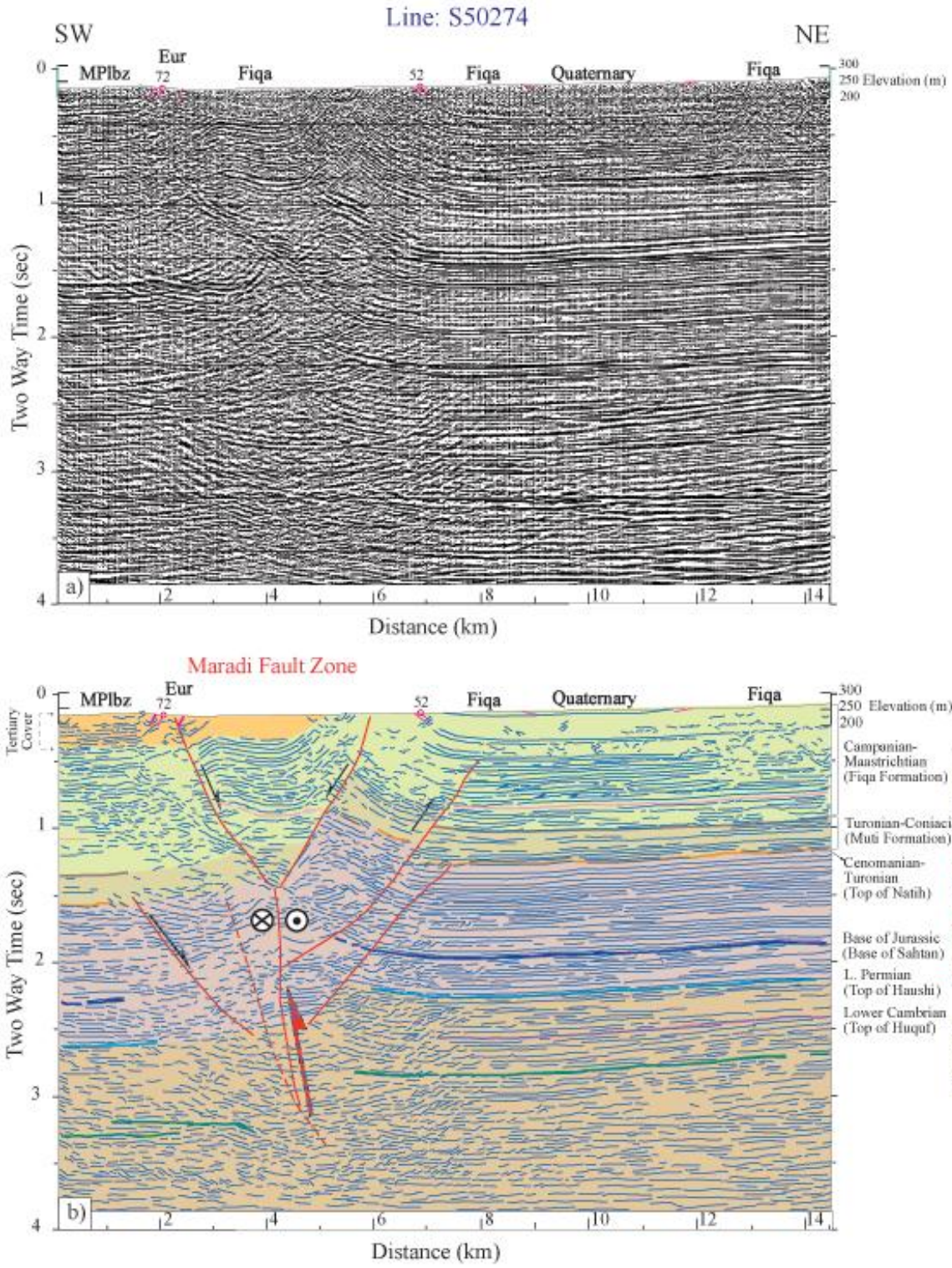
Line: S50274
SW
NE
MPlbz
Eur
72
Fiqa
52
Fiqa
Quaternary
Fiqa
300
250 Elevation (m)
200
Two Way Time (sec)
0
1
2
3
4
a)
2
4
6
8
10
12
14
Distance (km)
Maradi Fault Zone
Tertiary Cover
Campanian-Maastrichtian (Fiqa Formation)
Turonian-Coniacian (Muti Formation)
Cenomanian-Turonian (Top of Natih)
Base of Jurassic (Base of Sahtan)
L. Permian (Top of Haushi)
Lower Cambrian (Top of Huquf)
Aruma Group
Hajar Supergroup (HSG) Sequence
Preperminan Sequence
b)

***Interior Zone: Line R40984***

Directly north of line S50274 (Figure 2.7) lies line R40984 (Figure 2.8) with about 8 km overlap. However, correlation between the two lines is possible as reflectors are sub-horizontal and no significant deformation exists in the overlap area. In line R40984 the top of HSG Sequence is distinct in the SW section as far as its intersection with the subsurface structure of Jabal Qusaybah (JQ). The top of HSG then becomes less obvious and its interpretation is based on correlation with the NE side of JQ and surface outcrops. The HSG sequence in this section is overlain by the Aruma Group only (Figure 2.8). The Jabal Qusaybah anticline is part of the arc shaped range from Jabal Salakh to Jabal Madmar shown in Figure 2.3. In this section Jabal Qusaybah is found to separate the southernmost extent of the Hawasina Sediments in the Hamrat Ad Duru Zone from the Interior Zone (Figure 2.8). The Jabal Qusaybah structure shows subsurface symmetry indicated by the top of HSG Sequence marker reflector found at ~1 s (twt), at both NE and SW sides of Jabal Qusabah (Figure 2.8). We interpret the structure of Jabal Qusaybah to be supported by a salt lens structure and its possible intrusion in the host rock is at ~2 s (twt) (Figure 2.8b). A set of normal faults is interpreted to affect the western limb of the Jabal Qusaybah structure, which could be related to the same event forming the negative flower structures observed in line S50295 (Figure 2.6). The Fiqa Formation reflectors are observed to onlap the SW limb of the Jabal Qusaybah structure (Figure 2.8). Reflectors at the base of the Fiqa Formation are also interpreted to downlap the top of the Muti Formation and prograde towards the SW (Figure 2.8).

***Hamrat Ad Duru Zone: Line R41019***

Line R41019 (Figure 2.9) located east of the transect in the Hamrat Ad Duru Zone has the highest signal to noise ratio and better shows stratigraphic relations

**Figure 2.8**: (a) A migrated 2-D seismic reflection profile of line R40984 crossing in the subsurface northern bounds of Jabal Qusaybah anticline structure (see Figure 2.3). (b) A line interpretation of the seismic line R40984 showing a normal fault system southwest of Jabal Qusaybah. Note we also interpret a zone of strike-slip faulting (flower structure) south of Jabal Qusaybah.

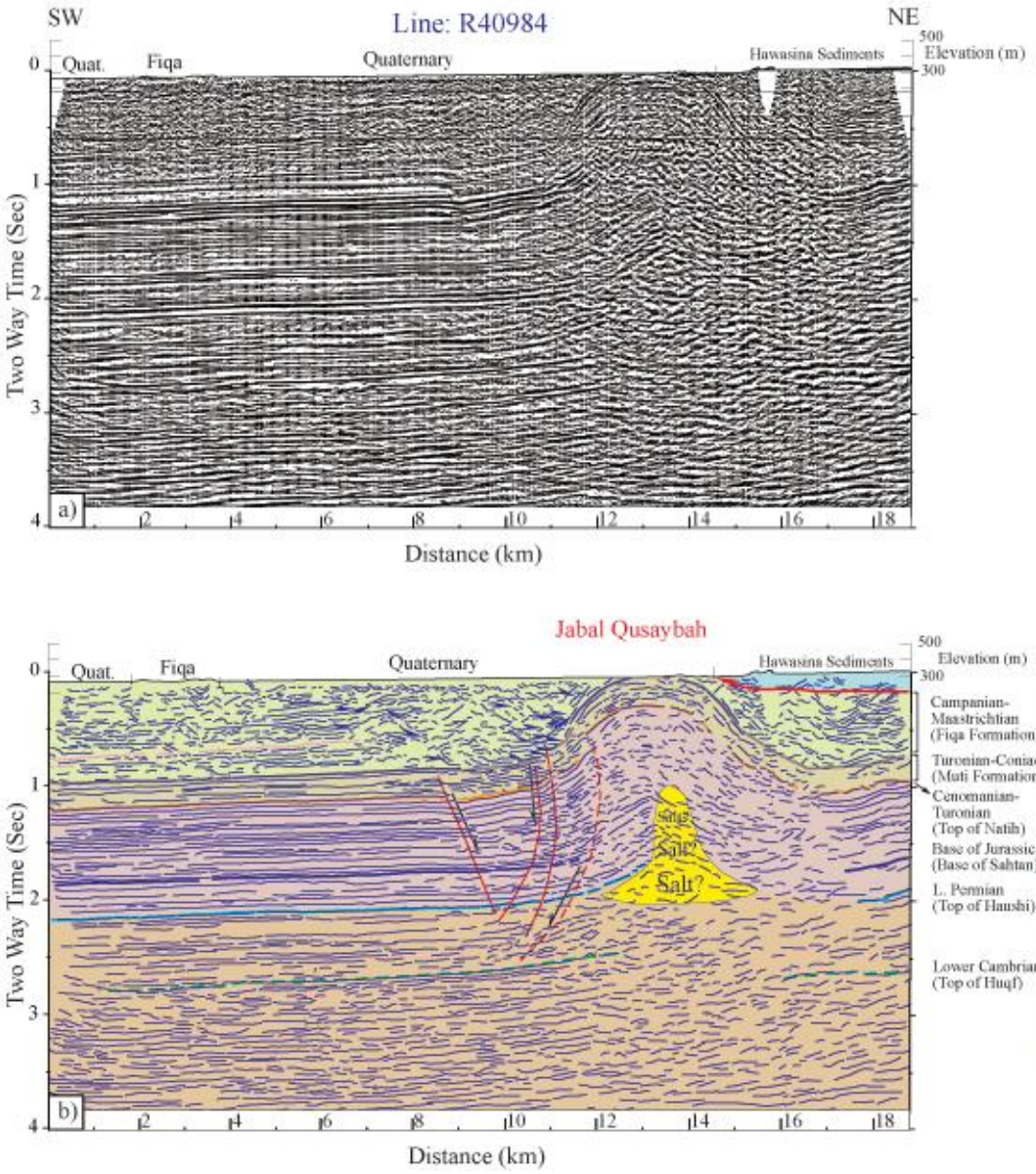
SW
Line: R40984
NE
Quat.
Fiqa
Quaternary
Hawasina Sediments
500
Elevation (m)
300
Two Way Time (Sec)
a)
Distance (km)
Jabal Qusaybah
Campanian-
Maastrichtian
(Fiqa Formation)
Turonian-Coniacian
(Muti Formation)
Cenomanian-
Turonian
(Top of Natih)
Base of Jurassic
(Base of Sahtan)
L. Permian
(Top of Haushi)
Lower Cambrian
(Top of Huqf)
Salt?
Salt?
Salt?
Arumaf
Group
Haushi Supergroup
(HSG) Sequence
Precambrian
Sequence
b)

**Figure 2.9**: (a) A migrated 2-D seismic reflection profile of line R41019 in the Hamrat Ad Duru Zone, overlain by line interpretation (see Figure 2.3 for location). The line interpretation shows reflectors of the Fiqa Formation down-lapping onto the top of Muti Formation in a southwesterly direction. Also important stratigraphic markers are shown.

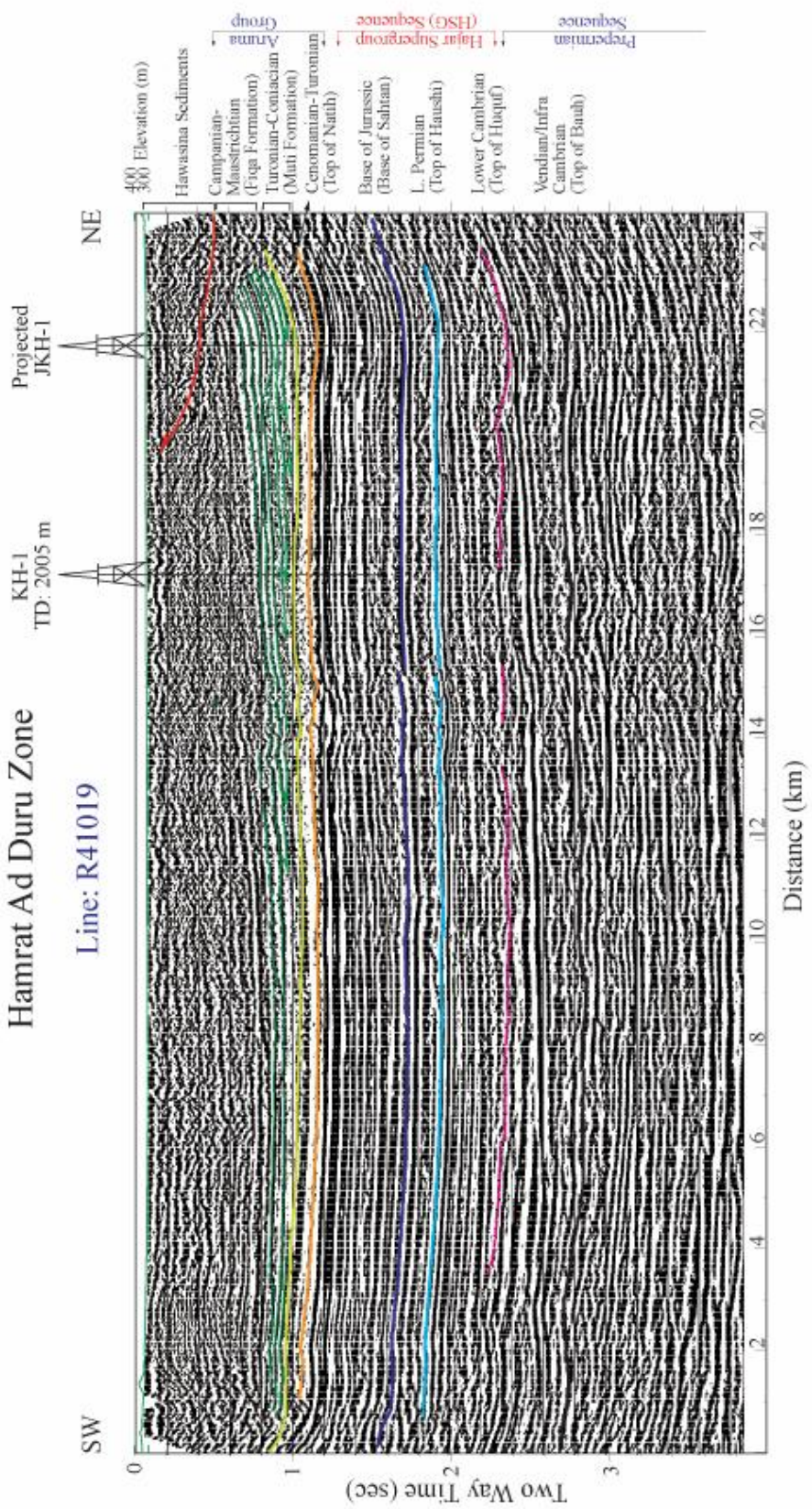
Hamrat Ad Duru Zone
Line: R41019
SW
NE
KH-1
TD: 2005 m
Projected
JKH-1
400
300 Elevation (m)
Hawasina Sediments
Campanian-
Maastrichtian
(Fiqa Formation)
Turonian-Coniacian
(Muti Formation)
Cenomanian-Turonian
(Top of Natih)
Base of Jurassic
(Base of Sahtan)
L. Permian
(Top of Haushi)
Lower Cambrian
(Top of Huquf)
Vendian/Infra
Cambrian
(Top of Bauh)
Arumaa
Group
Haiar Supergroup
(HSG) Sequence
Pre-permian
Sequence
0
1
2
3
Two Way Time (sec)
2
4
6
8
10
12
14
16
18
20
22
24
Distance (km)

within the Aruma Group. In this profile the HSG Sequence top is marked by the Natih Formation reflector at ~1.2 second (twt) and its base is marked by the top of Haushi Group (Late Permian) reflector at ~2 seconds. The HSG Sequence shows minor change in thickness compared to the Interior Zone (Figure 2.9). It is noteworthy that the top of HSG is identified in seismic profiles throughout the Hamrat Ad Duru Zone, which establishes its continuity with the surface outcrop at the southern limb of Jabal Akhdar Mountain. Line R41019 also shows the top of Huqf Group (Lower Cambrian) and the top of Buah Formation (Vendian/Infracambrian) (Figure 2.9). Downlapping reflectors of the Fiqa Formation mark the top of Muti Formation, which is shown to be thinner than what is interpreted in previous profiles in the Interior Zone. The downlapping reflectors of Fiqa Formation (dark green) show steeper dips, especially in the NE half of the line (Figure 2.9). The downlapping reflectors indicate progradation towards the SW direction.

***Coastal Zone: Line IUL0205***

A gap in seismic and well data coverage across the Jabal Akhdar Mountain Zone limited the subsurface information within the mountain. To provide other constraints we used structural information obtained from 1:200,000 scale geological maps to correlate the pre-Permian Sequence, the HSG Sequence, and the overlying units across the Mountain Zone.

In the Coastal Zone we show the interpretation of line IUL0205 (Figure 2.10) instead of IUL0203. Line IUL0205 is parallel to IUL0203 and shows almost identical structural features, but with a better resolution. The Coastal Zone (Figure 2.10) is characterized by a widespread ophiolite blocks overlain in the northern parts by the Tertiary sediments and Quaternary alluvial deposits (Tertiary Cover Sequence). Continuity of the top of the HSG Sequence could not be identified in all seismic

**Figure 2.10**: (a) Line interpretation of 2-D seismic reflection profile of line IUL0205. The 2-D section delineates the Semail Ophiolites (Nakhl block) and stratigraphic units overlying it. (b) Seismic stratigraphy showing retrograding sequence complex along the continental shelf margin. A, B, C, and D are progradational sequences within the retrograding complex. The retrograding complex is indicative of episodic uplift of the Northern Oman Mountain during the Oligocene. Abbreviated text SD stands for Sheeted Dykes (upper unit of the ophiolites).

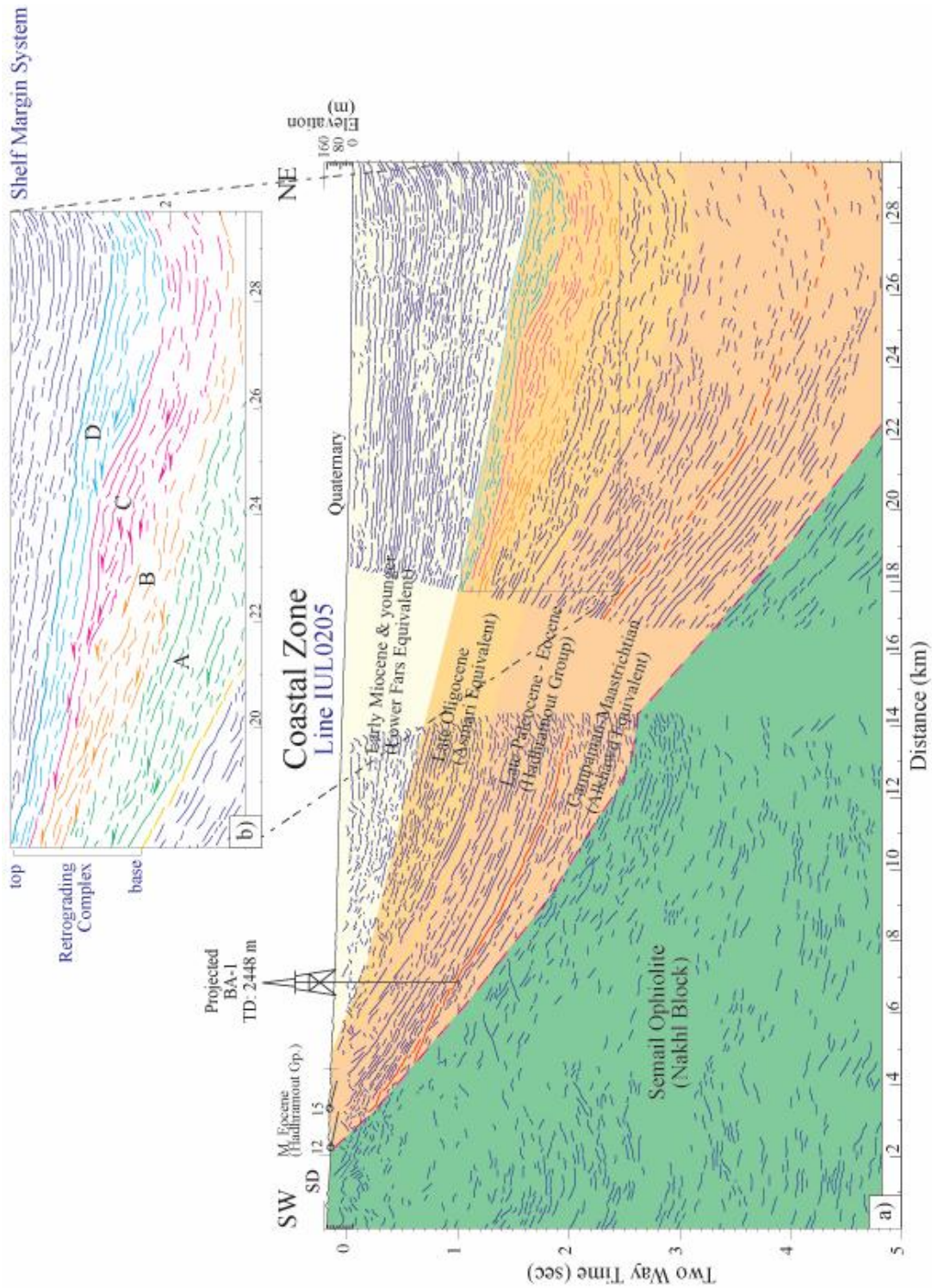
Shelf Margin System
top
Retrograding Complex
base
A
B
C
D
b)
Coastal Zone
Line IUL0205
SW
NE
Elevation (m)
160
80
0
Quaternary
Early Miocene & younger (Lower Fars Equivalent)
Late Oligocene (Asmari Equivalent)
Late Paleocene - Eocene (Hadhramout Group)
Campanian-Maastrichtian (Aruma Equivalent)
Semail Ophiolite (Nakhl Block)
Projected BA-1 TD: 2448 m
SD
M. Eocene (Hadhramout Gp.)
a)
Two Way Time (sec)
Distance (km)

reflection coverage in the Coastal Zone. The extensive thickness of the Nakhl Ophiolite block and the Tertiary Cover most likely masks the HSG Sequence that we observed in the foreland region. Chaotic to reflection free character is observed within the 2.5-10 km thick Nakhl Ophiolite block (Shelton, 1990) shown in Figure 2.10. The Nakhl Ophiolite block extent continues at the surface towards the southwest until the northern limb of the Jabal Akhdar structure. The Nakhl Ophiolite block includes both the mantle and the crustal units of the ophiolite body, separated at the surface by a thrust boundary dipping towards the north. The crustal section of the Nakhl Ophiolite block averages a dip of ~20$^{O}$N (Nicolas et al., 1996). At the surface, a minor, yet distinct linear feature of Hadhramout Group outcrops in the northern bounds of the ophiolite body, striking NW-SE, and dipping 15$^{o}$ north. Line IUL0205, located 8 km east of the transect (see Figure 2.3) shows the upper boundary of the ophiolite body dipping at ~25$^{o}$N based on the depth converted section of IUL0205 (Figure 2.10). Northwest of the transect Hawasina sediments are observed to overlie the volcanic section of the Semail Ophiolites. But, along the Coastal Zone section of the transect geological maps show no units equivalent to the Hawasina nappes atop the Nakhl Ophiolite block. Seismic lines IUL0203 and IUL0205 (Figure 2.3) showed no indication of discordant units above the Nakhl Ophiolite block. Three seismic stratigraphic sequences are distinguished overlying the Nakhl Ophiolite block shown in Figure 2.10: (1) the Alkhawd Formation Equivalent and the Hadhramout Group (Late Campanian-Eocene), (2) the Asmari Equivalent (Late Oligocene), and (3) the Lower Fars Equivalent (Early Miocene-Recent). On line IUL0205 the Alkhawd Formation equivalent unconformably overlies the top of the Nakhl Ophiolite block. The Alkhawd Formation thickens towards the NE and is pinched-out at the surface in the SW. Cyclic shallow to deep, shelf environment carbonates of the Hadhramout group overly the Alkhawd Formation equivalent (unpublished report, Amoco Oman

Petroleum Company, 1985). The base of the Hadhramout Group reflectors shows an ambiguous boundary relation with the Alkhawd Formation top, where well penetration could have resolved this ambiguity. A regional erosional unconformity of early Oligocene age recorded in well BA-1 (unpublished report, Amoco Oman Petroleum Company, 1985) marks an uplift period that followed the deposition of the Hadhramout Group. Later in the Middle to Late Oligocene times, seismic reflection interpretation indicates a period of marine transgression that led to the deposition of the Asmari Formation, equivalent to shallow outer shelf to marginal marine environment (unpublished report, Amoco Oman Petroleum Company, 1985). Shown in the seismic profile, the sea transgression was perturbed by episodic margin uplifts indicated by seaward migration of facies A, B, C and D (Figure 2.10). Within each cycle, transgression is indicated by reflectors onlapping the top of the older cycle (Figure 2.10). The Lower Fars Group equivalent and the Quaternary alluvial deposits form a wedge-shaped seismic pattern, indicative of a continued margin uplift throughout the Miocene, possibly until the Quaternary time (Figure 2.10). The seismic reflection gap between 14 and 16 km distance is an offset of the NE dipping Hadhramout Group (Figure 2.10). This offset is observed to effect the Hadhramout Group, and can be traced on seismic lines parallel to IUL0205 extending for ~45 km across the transect line. This offset could be the result of a magmatic intrusion process that is reported by Al-Harthy et al. (1991) to have occurred during the Tertiary period on the northern flanks of Jabal Akhdar and Saih Hatat structures. Northeast of the transect Hawasina sediments are observed to overlie the volcanic section of the Semail Ophiolites. But, along the Coastal Zone section of the transect geological maps show no units equivalent to the Hawasina nappes atop the Nakhl Ophiolite block. Seismic lines IUL0203 and IUL0205 (see Figure 2.3 for location) showed no indication of discordant units above the Nakhl Ophiolite block.

## MOHO DEPTH ESTIMATES FROM RECEIVER FUNCTIONS

### Methodology

Receiver function is a single-station teleseismic technique used to study P-wave train to isolate structural effects under a seismic station. Generally, the receiver function technique utilizes converted seismic phases, such as P to S (Ps) and converted P-wave multiples reflecting within the crust. For earthquakes at distances of more than $30^{O}$ seismic P-waves are steeply incident beneath a seismic station, and dominate the vertical component of ground motion, whereas a converted phase, such as Ps, is largely contained in the horizontal components of ground motion (e.g. Clayton and Wiggins, 1976; Burdick and Langston, 1977; Cassidy, 1992; Zandt and Ammon, 1995; Sandvol et al., 1998b). The locally generated Ps phase amplitude is sensitive to the S-velocity structure beneath the station (Cassidy, 1992), and its arrival time relative to the first P-wave is used to estimate the depth of conversion. Since the largest velocity change in the lithosphere is along the Moho boundary, receiver functions are mainly used for Moho depth estimation (e.g. Sandvol et al., 1998a and b).

A seismic wave propagating from a source to a seismic station includes information about the source mechanism, the velocity structure surrounding the source, the velocity structure along the ray path, and the crust and upper mantle structure below the recording station (Burdick and Langston, 1977). For the recording of teleseismic earthquakes the converted Ps phase is isolated from the source effects by deconvolving the vertical component of ground motion with the radial components of the P waveform to produce the time series know as receiver function (Zandt and Ammon, 1995). Whereas, the radial component is used to estimate the Moho depth, the tangential component provides information about any possible dip in the Moho

interface. Details of the receiver function technique we used are described in Sandvol et al. (1998b) and will not be discussed here.

**Data and Analysis**

We used teleseismic data recorded by two short-period (1 Hz), 3-component, portable digital instruments deployed in four different locations along the transect (Figure 2.3). Each station was operated for at least two months and recorded with a sampling interval of 50 samples per second (Table 2.1). The stations occupied locations within cities and villages where power supply was available and accessibility to the site was not restricted. Recorded teleseismic earthquakes were largely from the western Pacific (Japan, Philippines, Taiwan, New Guinea, and Indonesian islands) (Figure 2.11). These events provided the necessary distance required for receiver function analysis. Most of the recorded earthquakes were associated with subduction zones (Figure 2.11). We used the time difference between the primary P-wave arrival and the converted P to S-wave (Ps) arrival to estimate depth to Moho along the transect (Figure 2.12). The average time differences between Ps-Moho and P are 4.7, 5.6, and 4.9 seconds for the stations KTOM, AWBI, and JBRN, respectively (Figure 2.12). We observed no obvious converted Moho phase, Ps-Moho, at the fourth station BSYA, possibly due to site problems. The receiver function of station KTOM showed the clearest signal that exceeded the noise level. In all stations the tangential components of the receiver function gave no indication of steeply dipping Moho, as shown by the low amplitudes in the tangential component at the arrival times of the Ps
phase. During our analysis of the receiver functions, we observed an intracrustal phase conversion, Ps-crust, beneath stations JBRN and BSYA.

In order to estimate the depth to Moho using the receiver functions shown in Figure 2.12, accurate velocity information beneath each station is required.

**Table 2.1**: Seismic station information: latitude, longitude, and the corresponding elevation. Included as well are the recording days for each station (used in receiver function study).

| Station Name | Latitude (Degree) | Longitude (Degree) | Elevation (m) | Recording time (days) |
|---|---|---|---|---|
| KTOM | 23.48 | 57.69 | 107 | 142 |
| AWBI | 23.30 | 57.53 | 397 | 37 |
| JBRN | 22.91 | 57.26 | 552 | 43 |
| BSYA | 22.73 | 57.24 | 348 | 80 |

**Figure 2.11**: Map centered on Oman showing locations of teleseismic earthquakes that were used to obtain the final receiver function response for the stations KTOM, AWBI, JBRN, and BSYA (see Figure 2.3 for location). Recorded events location, magnitude, and depth information were obtained from the USGS event catalog (Mb: body wave moment magnitude).

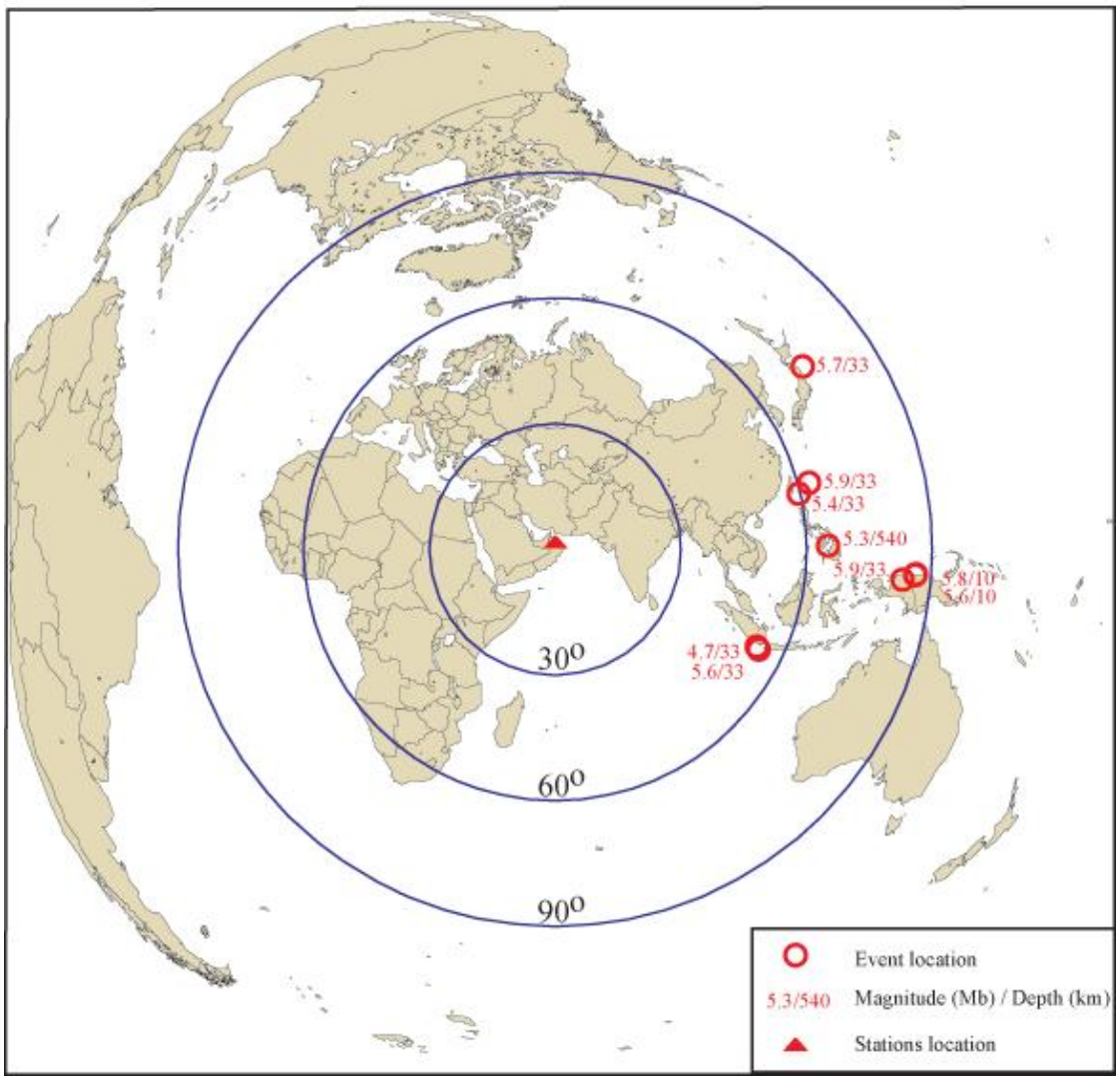
5.7/33
5.9/33
5.4/33
5.3/540
5.9/33
5.8/10
5.6/10
4.7/33
5.6/33
30°
60°
90°
Event location
5.3/540 Magnitude (Mb) / Depth (km)
Stations location

**Figure 2.12**: Radial (R) and Tangential (T) component stacks of receiver functions for the stations KTOM, AWBI, JBRN, and BSYA. P denotes a direct P-wave arrival, Ps-Moho denotes P to S-wave converted phase at Moho, R denotes radial, T denotes tangential, and Ps-mc denotes intracrustal P-wave phase conversion at a mid-crustal discontinuity. Values given in brackets denote (distance between station and event/back azimuthal direction from station to event).

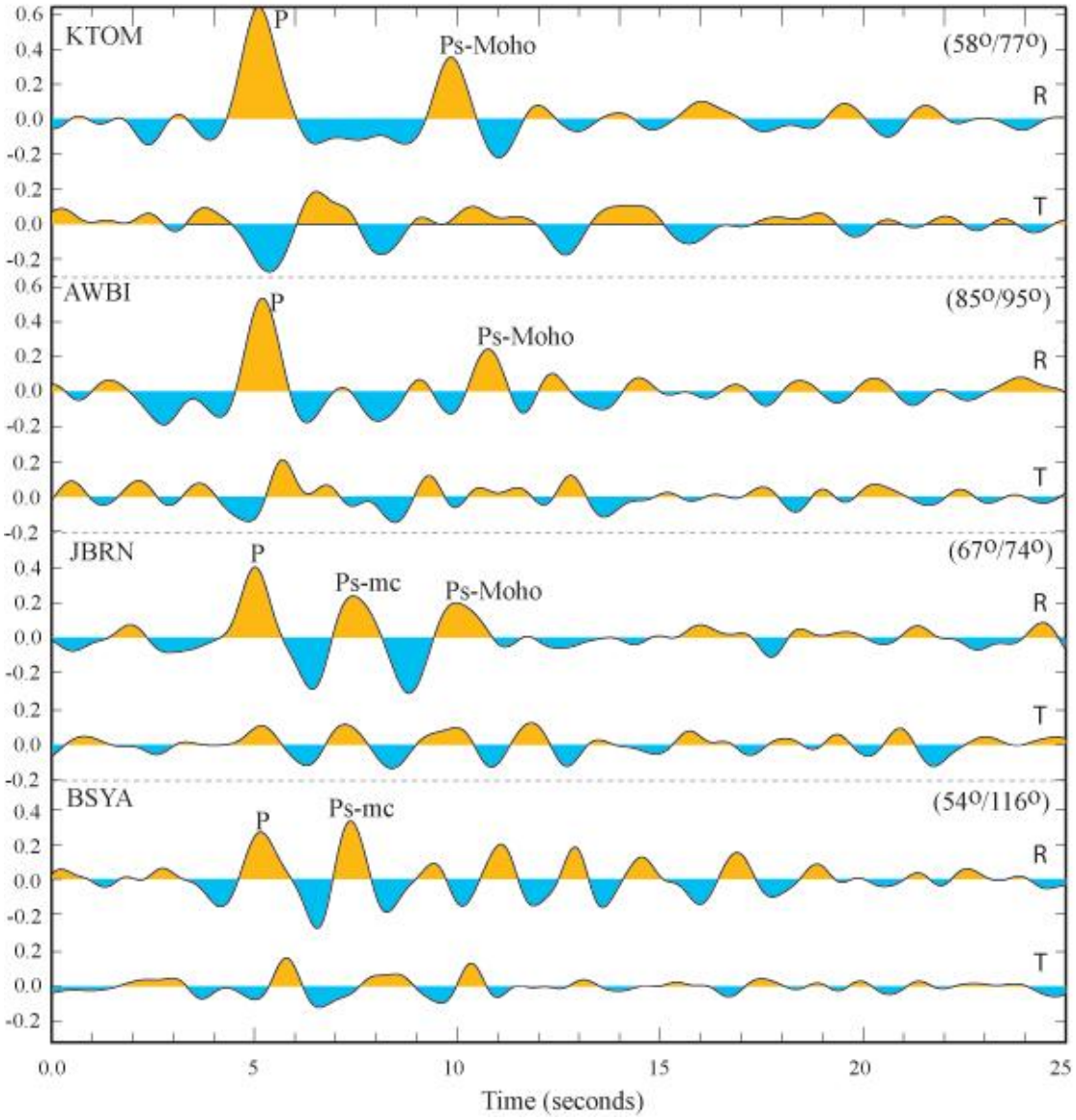
KTOM
P
Ps-Moho
(58°/77°)
R
T
AWBI
P
Ps-Moho
(85°/95°)
R
T
JBRN
P
Ps-mc
Ps-Moho
(67°/74°)
R
T
BSYA
P
Ps-mc
(54°/116°)
R
T
0.6
0.4
0.2
0.0
-0.2
0.0
5
10
15
20
25
Time (seconds)

Unfortunately, we do not have average crustal velocity information directly beneath the stations. However, a number of studies on the eastern Arabian shield provide estimates of the average P-wave velocity of the crust in the region. Mooney et al. (1985) reported an average crustal velocity of 6.6 km/s; and Badri (1990) reported a 6.5 km/s average crustal velocity. We used these average velocities as representative for the southeastern Arabian margin and the foreland region. However, the study area has significant sediment thickness that could affect the average crustal velocities. To estimate the effect of the sedimentary section we used available, average sonic velocity for the total depth of DA-7 and ML-1 wells. At the latter two wells the average velocity for ~5 km sedimentary section is between 5.2 km/s to 5.4 km/s (Figure 2.5). In this region, sedimentary units younger than Late Cretaceous age have an average velocity of 3 km/s. The thickness of these sediments varies throughout the region, but along the transect the maximum thickness is only 1-1.5 km, which will have ~2% effect on the averaged crustal velocity. Since we do not have absolute velocity values of the entire crust, and have only average measurements from a nearby region, we used a range of velocity values with a minimum limit of 6.4 km/s and a maximum limit of 6.8 km/s for the whole crust to take into account any potential uncertainty. An additional velocity error is introduced by the converted phase (Ps) wavelength, where the interface resolution is dependent on the frequency of the impinging wave. Hence we estimate an additional error of ~1 km. Based on a 6.6 km/s crustal velocity, and a 0.25 Poisson's ratio value (Zandt and Amon, 1995), the calculated Moho depth for KTOM station is 41 km (Figures 2.3 and 2.13). Also, taking into account potential errors, we estimate the Moho depth beneath this station to be 41±2 km. Due to the incident angle of the incoming seismic wave, the actual Moho impingement is at 8 km east of KTOM location based on the assumed seismic velocity above. In this zone (Coastal Zone) the ophiolite blocks are estimated to vary

in thickness between 10-20 km (Shelton, 1990). Ophiolites in north Oman have an average compressional velocity of about 6.9 km/s (Christensen and Smewing, 1981). The ophiolite block accounts for at least 25% of the average continental crust thickness in the region (45 km). This high velocity could result in a small decrease in the estimated Moho depth at KTOM station by about 4 km, which is about the total estimated error. The actual impingement location of the AWBI station falls within the northern limb of the Jabal Akhdar Mountain, which isolates it from the high velocity ophiolite effect in this region. AWBI station, located in the northern limb of the Jabal Akhdar Mountain gave a Moho depth of 49±2 km, which is about 5 km deeper than the Moho depth beneath KTOM station. The station of JBRN located directly south of the Jabal Akhdar Mountain (Figure 2.3), produced a Moho depth of 43±2 km (Figure 2.13). The actual Moho impingement of JBRN is located within the Hamrat Ad Duru Zone, where, the ophiolite body is only ~500 meters thick (based on seismic and gravity modeling) and would not produce significant errors in the calculated depth (Figure 2.3).

**GRAVITY MODELING**

Seismic reflection profiles along with well log data provided thickness information for the upper 8 km along the transect. However, seismic reflection profiles alone could not provide the total depth to basement along the transect. Similarly, the receiver function provided accurate Moho depths beneath three points along the transect, but would not further predict Moho topography in other parts of the transect. In addition, the Jabal Akhdar Mountain Zone does not include seismic nor well data coverage. In order to determine the subsurface structure along the entire transect, we used gravity modeling constrained by the existing seismic, well logs, and receiver function results. Gravity modeling is a non-unique methodology. However, our use of

**Figure 2.13**: Velocity-depth trade off curves for stations KTOM, AWBI, and JBRN. For a 6.6 km/sec average crustal velocity, we estimate a Moho depth of 41±1 km, 49±1km, and 43±1 km for the stations KTOM, AWBI, and JBRN, respectively. The depth error bar here is estimated for a velocity minimum of 6.4 km/sec and maximum of 6.8 km/sec velocity error.

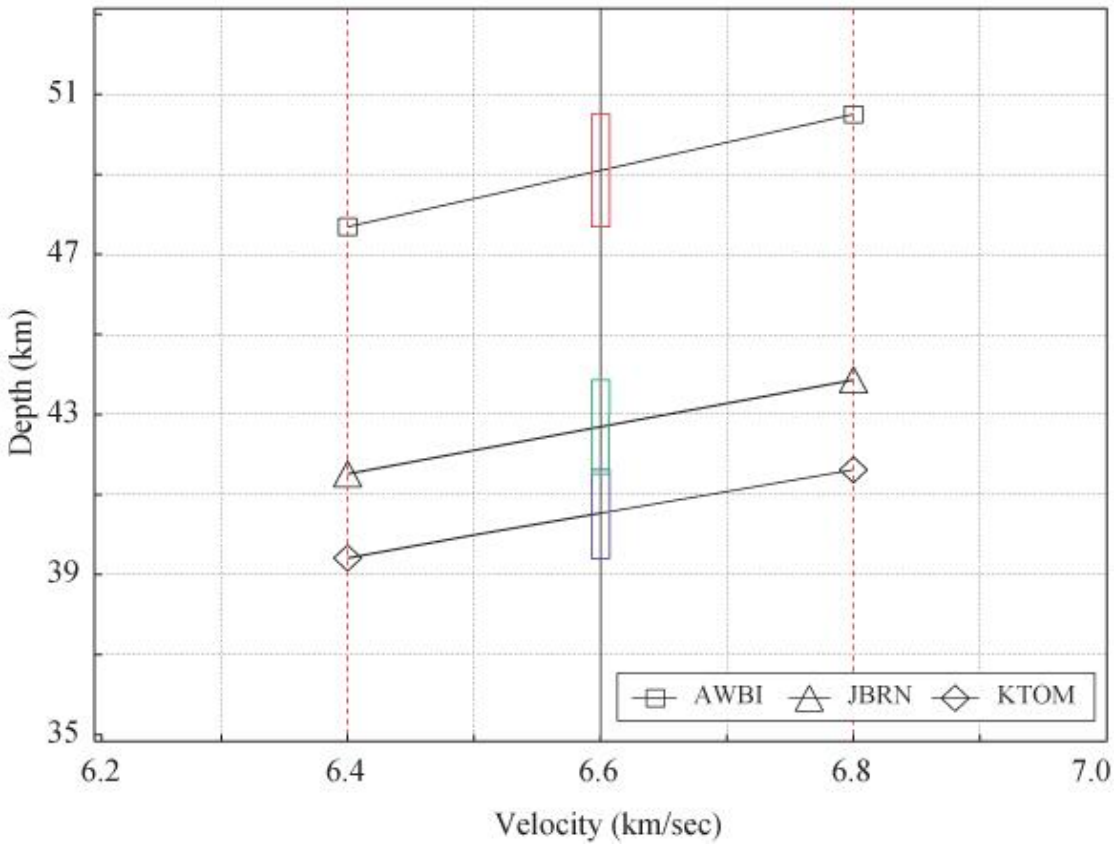
51
47
43
39
35
Depth (km)
6.2
6.4
6.6
6.8
7.0
Velocity (km/sec)
AWBI
JBRN
KTOM

seismic, well logs, and receiver function results made gravity modeling a more useful tool. We used GMSYS gravity modeling software of the Northwest Geophysical Associates Incorporation, which uses a 2.5-D body model, allowing limits on the lateral extent of each modeled body.

**Data**

In this study, we used Bouguer gravity data of Oman compiled by Ravaut and Warsi (1997). The determined Bouguer gravity anomalies are based on the international gravity formulae and are corrected for a 2.67 g/cm$^3$ slab. We used their available Bouguer point values along a 50 km wide swath at a 5 km interval along the transect (Figure 2.14). In areas with no digital information, we obtained the average Bouguer values from their published gravity map of Oman (Ravaut and Warsi, 1997) with the same sampling interval and swath width. We also extracted surface elevation data at a 5 km sampling interval (Figure 2.14). We modeled the average gravity value of the 50 km swath shown in Figure 2.14. Density information of modeled stratigraphic units was primarily obtained from well logs of corrected bulk density values and/or transient sonic velocity. We used Gardner's equation (Gardner et al., 1974) to convert transient sonic velocity values to density values. JKH-2, FH-1, and SD-1 wells provided density values for the Hawasina Sediments (2.45 g/cm$^3$) and the Aruma Group (2.28 g/cm$^3$). Density value for the HSG Sequence (2.6 g/cm$^3$) was obtained from ML-1 and DA-7 wells located northwest of the transect (see Figure 3). Density values of the ophiolite (3.07 g/cm$^3$) and the upper mantle (3.3 g/cm$^3$) were obtained from previous studies conducted in the same region (Ravaut, 1997a). In this study, density value of the pre-Permian Sequence is set to 2.5 g/cm$^3$ as an average value, which is smaller than the density value of the overlying HSG Sequence (2.6 g/cm$^3$). We approximated the pre-Permian Sequence density to ~2.5-2.55 g/cm$^3$ that

**Figure 2.14**: **(a)** Graph showing maximum, minimum, and average Bouguer gravity anomalies in a 50 km swath along the transect (see Figure 2.3 for location). **(b)** Graph showing maximum, average, and minimum elevation profiles along the transect. Gravity and elevation values are calculated for a 5 km sampling interval along the complete transect.

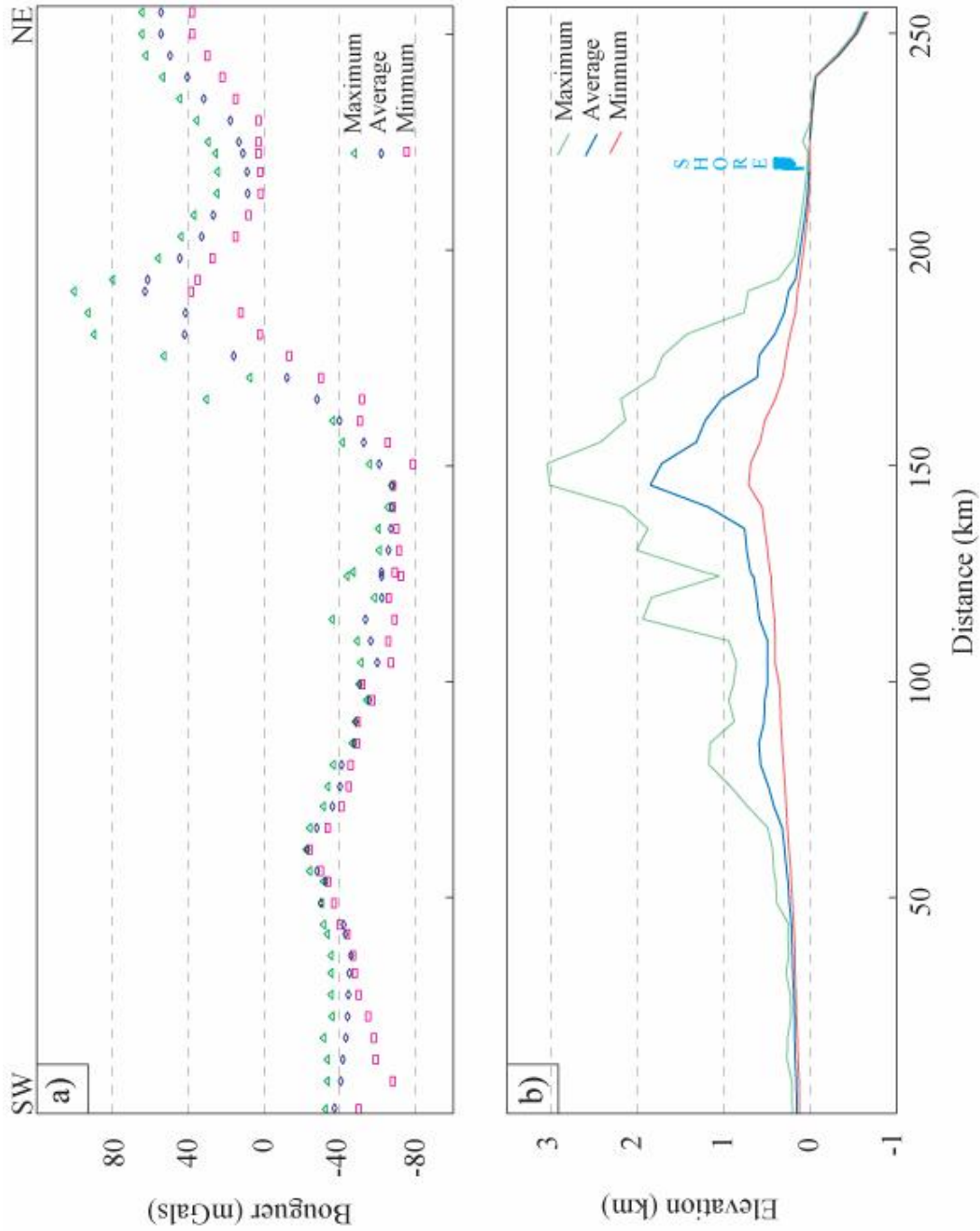
SW
NE
a)
Maximum
Average
Minimum
80
40
0
-40
-80
Bouguer (mGals)
b)
Maximum
Average
Minimum
S H O R E
3
2
1
0
-1
Elevation (km)
50
100
150
200
250
Distance (km)

accommodates for the Ara salt (2.2 g/cm$^3$) which is known to extend throughout the study area, with enormous thickness variation between 0-2000 meters (Mattes and Morris, 1990; Mount et al., 1998). The estimated pre-Permian Sequence density 2.5-2.55 g/cm$^3$ was found to be the most suitable value for the pre-Permian Sequence that resulted in a good model fit with the observed gravity values. We have estimated a comparable density value for the middle and lower crust of 2.7 g/cm$^3$. Known constraints in the Coastal Zone include the upper boundary of the ophiolite block dip angle, 25$^O$N, and density of the ophiolite and the overlying sequences. BA-1 well provided density information for the Hadhramout group (2.45 g/cm$^3$) and for the Eocene-Recent sediments (2.2 g/cm$^3$). In the Coastal Zone, we approximated the density of the Alkhawd Formation equivalent as that of the Hadhramout group. The edge of the continental margin is found at ~40 km farther northeast of the end of the transect. It drops off to ~3000 m depths into the Oman remnant basin. Therefore, we allowed termination of the Shelf and the pre-Permian Sequences towards the NE end of the model. Also, we allowed the basement depth to shallow at the northern end of the model.

Moho depth obtained for the stations KTOM, AWBI, and JBRN were used to constrain the Moho structure across the Jabal Akhdar Mountain. In all models, we allowed the Moho depth south of Jabal Akhdar Mountain to vary about the determined Moho depth at JBRN station (43 km). In the northeastern part we varied the Moho depth below what is obtained from KTOM station to accommodate the crustal thinning towards the oceanic areas of the Gulf of Oman. In addition, we allowed the Moho depth to vary beneath the Jabal Akhdar Mountain to accommodate for any possible crustal thickening beneath the Mountain.

Observed Bouguer gravity values along the transect vary from –80 mGal beneath the Jabal Akhdar Mountain to +100 mGal about 40 km NE of the mountain

(Figure 2.14). In the foreland region, in the southwest portions of the transect, Bouguer values are uniform at about -40 mGal with ~20 mGal variation. As we approach the Jabal Akhdar Mountain the Bouguer values decrease and reach their minimum in the Jabal Akhdar Mountain. From this point northward, the Bouguer gravity values increase sharply towards the continental margin. A shorter wavelength positive anomaly is superimposed on the regional anomaly, just NE of the Jabal Akhdar Mountain. This anomaly corresponds to the Nakhl ophiolite block. Farther north, the anomaly increases to a maximum +60 mGal reflecting crustal thinning and proximity to the oceanic crust of the Gulf of Oman. A superimposed negative anomaly coupled with the ophiolite positive anomaly correspond to a small intra-margin basin.

The ophiolite emplacement resulted in different grades of metamorphism in the Northern Oman Mountains that varied from high temperature, low pressure, amphibolite and green schist facies; at the base of the of ophiolite, to high pressure, low temperature, eclogite and blueschist facies (El-Shazly and Coleman, 1990). The Saih Hatat structure is described to have been subject to high grades of metamorphism forming eclogite facies in its northern bound at the coastline area (El-Shazly and Coleman, 1990). However, the Akhdar structure is categorized to have received only early phases of well-developed cleavage deformation. (Le Metour et al., 1994). To accommodate this low metamorphic gradient we included a density increase towards the NE, across the Jabal Akhdar Mountain to the Coastal Zone. The low gradient density increase affects lithologic units overlain by the Hawasina Sediments and the Semail Ophiolites.

## Gravity Analysis

### *Model-A*

In general, basement topography in the foreland region is found to mimic the observed gravity response (Figure 2.15, Model A). Gravity modeling shows a relative basement high at ~7 km depth beneath the Jabal Qusaybah structure. The relative anomaly beneath Jabal Qusaybah is part of a basement high, averaging ~ 9 km deep, that extends for ~60 km from the MFZ to the center of Hamrat Ad Duru Zone. Basement depth south of the MFZ and the northern end of the Hamrat Ad Duru Zone averages at ~13 km. A small anomaly of less than 10 mGals corresponds to the ophiolite body directly south of the Jabal Akhdar Mountain. Basement depth in the core of Jabal Akhdar Mountain is shown at ~9 km and implies a thickened pre-Permian Sequence below the core of the Jabal Akhdar Mountain (Figure 2.15). The considerably thickened pre-Permian Sequences at the core of Jabal Akhdar Mountain corresponds to a short wavelength gravity response, that could not be compensated by depth changes at the mountain root. The northern limb of the Jabal Akhdar Mountain, however, shows an extensively thinned pre-Permian Sequence, below the Allochthonous Sequence of the Semail Ophiolites and the Hawasina Sediment. North of the Jabal Akhdar Mountain a positive and a negative anomaly couple, overrides the regional anomaly and correspond to the north dipping ophiolite body and the intra-margin Tertiary basin, respectively. The determined average thickness of the ophiolite block, north of Jabal Akhdar Mountain is ~5 km, and extends laterally for about 95 km north. Below the ophiolite body, the Hawasina Sediments average in thickness to ~1 km along the Coastal Zone, but thicken extensively to ~4 km below the surface outcrop of the ophiolite block, directly north of the Jabal Akhdar Mountain (Figure 2.15). Based on Model-A, the modeled Hawasina Sediments are substantial in

**Figure 2.15**: Cross sections showing the entire crust and upper mantle obtained from gravity modeling. Model-A: Density values of 2.7 gm/cc and 2.5 gm/cc for the lower crust and the pre-Permian Sequence, respectively. A minimum lateral density variation is allowed in this model. Model-B: For a 2.7 gm/cc and 2.55 gm/cc for the lower crust and the pre-Permian Sequence, allowing relatively more lateral variation in density values along the transect. Density values are allowed to increase along both sections, from southwest to northeast, for both models.

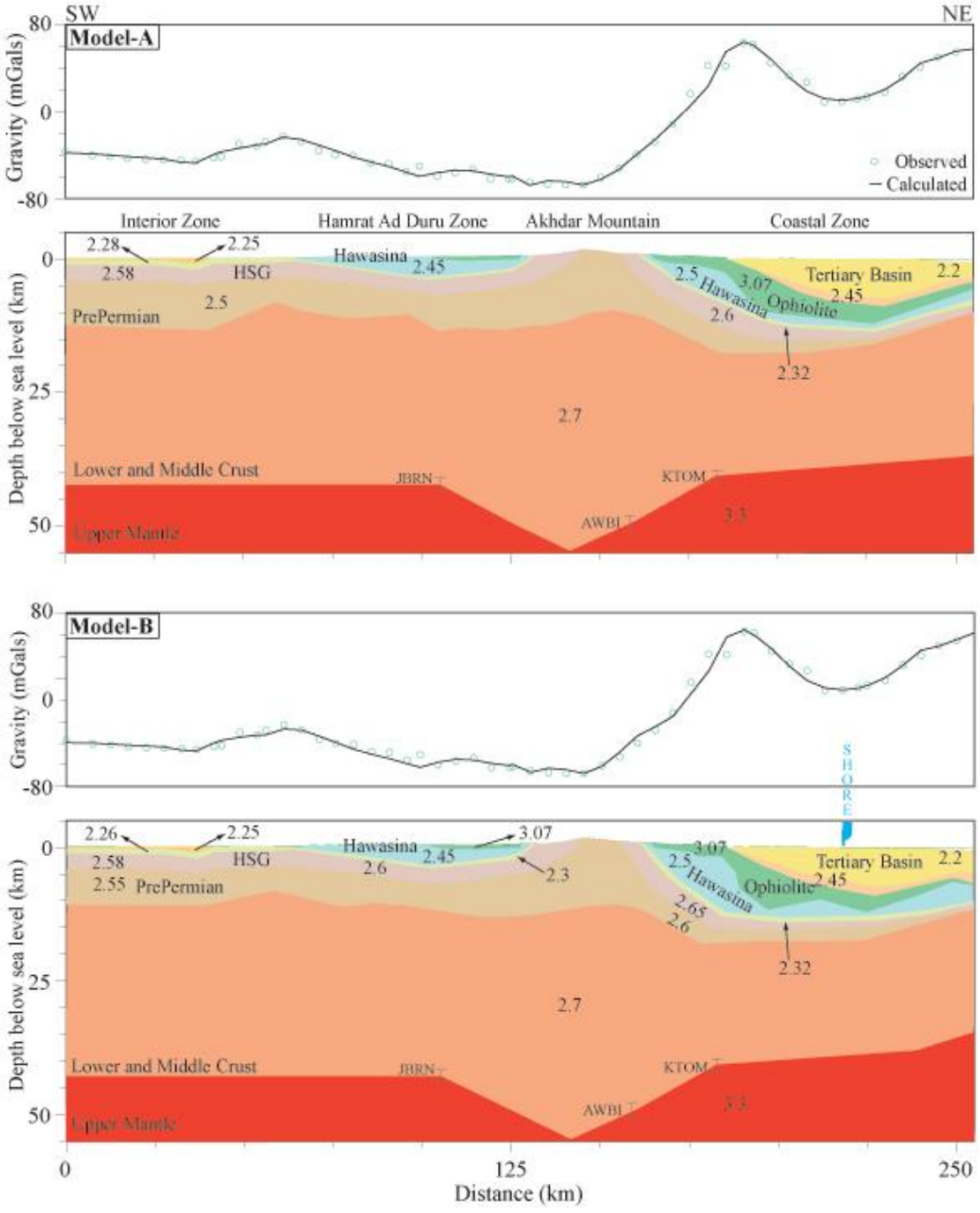
SW
NE
Model-A
Gravity (mGals)
80
0
-80
Observed
Calculated
Interior Zone
Hamrat Ad Duru Zone
Akhdar Mountain
Coastal Zone
Depth below sea level (km)
2.28
2.25
2.58
HSG
Hawasina
2.45
2.5
3.07
Tertiary Basin
2.2
2.45
Hawasina
Ophiolite
2.6
PrePermian
2.5
2.32
2.7
Lower and Middle Crust
JBRN
KTOM
AWBI
3.3
Upper Mantle
Model-B
SHORE
2.26
2.25
3.07
2.58
HSG
Hawasina
2.45
2.6
2.3
2.55
PrePermian
2.65
2.6
0
25
50
0
125
250
Distance (km)

thickness and are comparable to the Hawasina Sediments south of the Jabal Akhdar Mountain. Note the Hawasina Sediments south of Jabal Akhdar are fixed, since they are constrained by seismic and well data. Geometry of the ophiolite body persisted in all models in which it required a leading and a trailing wedge in various density models, with variable thicknesses between 5 to 8 km. Depth to basement in the Coastal Zone reaches its maximum at ~17 km below the surface outcrop of the ophiolite body, and shallows towards the NE, imposing thinning of the HSG and pre-Permian Sequences (Figure 2.15).

***Model-B***

In this model we included a semi-gradual density increase of 0.05 g/cm$^3$, from SW to NE, for the Pre-Permian and HSG Sequences, the Hawasina Sediments, and the Aruma Group (Figure 2.15). The depth to basement shallows by about 2.5 km in the Interior and Hamrat Ad Duru Zones, with a 2.55 g/cm$^3$ pre-Permian Sequence density. Since the density contrast between the pre-Permian Sequence and the lower crust is reduced, the thickness of the pre-Permian Sequence was therefore reduced. Consequently, only large topographic differences, such as Jabal Qusaybah anomaly were clearly resolved in the foreland region. North of the Jabal Akhdar and the Coastal Zone this density change results in a dip increase of the northern limb of the mountain (Figure 2.15). This consequently increased the thickness of the Hawasina Sediments at the expense of the ophiolite body. Thickness-density trade-off between the Hawasina Sediments and the ophiolite bodies resulted in an irregular ophiolite body, which we did not consider the favoured ophiolite model. To further constrain the model in the Coastal Zone, we require information on the extent of the HSG and pre-Permian Sequences beneath the ophiolite body, or the knowledge of the ophiolite body thickness in addition to the density of the lower and middle crust.

Model-A, is our favored model, but Model-B provides an alternative and an error estimate for the preferred model (Figure 2.15).

## DISCUSSION

Compilation of multidisciplinary results based on seismic reflection, well data, receiver function analysis, and gravity modeling combined with surface geology provided reliable constraints to construct a complete crustal transect across the foreland region, the Mountain and the Coastal Zones (Figure 2.16). Furthermore, data analysis and interpretation provided structural and stratigraphic relations that added to the understanding of processes that accompanied the Semail Ophiolite emplacement and later developments along the margin and the foreland region.

### The Foreland Region

Robertson (1987), Boote et al. (1990), and Bechennec et al. (1994), amongst other researchers, collectively summarized the nature of the Semail Ophiolite emplacement along the Arabian margin and the foreland regions, and proposed three distinct evolutionary processes: doming, complete margin subsidence, and final foreland subsidence during and after the ophiolite advancement onto the margin and inland. Based on the interpretation of seismic lines S50295 (Figure 2.6), R41019 (Figure 2.9) and other seismic lines in the foreland region (not shown on our map), our seismic stratigraphy interpretation conforms well to their three observed processes.

The first process, doming in the Turonian period is marked by an erosion unconformity off the top of Natih Formation (Albian) throughout the foreland (Bechennec et al., 1994). We observe relatively more erosion of the top of Natih Formation that has affected the Hamrat Ad Duru Zone and the Fahud area (FD-1 well) (Figure 2.5). The second stage of emplacement, where complete margin subsidence is

marked by the development of the Muti basin throughout the foreland region and the Mountain Zone (Robertson, 1987; Boote et al., 1990; Bechennec et al., 1994). As evident from seismic stratigraphy, the Muti Formation (Turonian-Santonian) overlies the Natih Formation throughout the foreland region, indicative of regional subsidence (Figures 2.7, 2.8, and 2.9). The third stage of the emplacement is where the advancement of the Allochthonous Sequence on the margin and inland is marked by the development of the extensive Fiqa basin (Campanian-Maastrichtian) (Bechennec et al., 1994). The Fiqa Formation records the stratigraphic interaction as the allochthonous body progresses towards the foreland (Figures 2.6 and 2.9). Southerly prograding reflectors of the Fiqa Formation are interpreted to downlap the top of the Muti Formation which is indicative of a localized topographic high moving southwards (Figures 2.6 and 2.9). This localized high could be attributed to the Semail Ophiolite emplacement peripheral bulge, migrating southwards. The southerly prograding reflectors are shown to onlap the southwestern edge of the Fahud area where, possibly, the advancing peripheral bulge ceased in the Interior Zone of Oman (Figure 2.6). Our observations conform to Robertson (1987) and conflicts with Warbuton et al. (1990) who advocate a none-migrating peripheral bulge. Note that as the peripheral bulge advanced, the region was submerged in deep open marine, outer shelf to upper bathyal environment accumulating the Fiqa Formation (Robertson, 1987; Bechennec et al., 1994).

Structural development of Jabal Qusaybah is concluded to have occurred during the Santonian. This is in agreement with Hanna and Smewing (1996) who showed that the Jabal Salakh structural growth began in the Late Cretaceous period during the Aruma Group deposition. Shown in Figure 8, the Muti Formation and HSG Sequence are both folded, indicating a deformation time that postdates the deposition of Muti Formation. Also, reflectors of the Fiqa Formation are shown to onlap the

**Figure 2.16**: The complete transect of the crust and parts of the upper mantle from the interior of Oman in the southwest, across the Jabal Akhdar Mountain and in the hinterland in the northeast. Also, shown observed and model Bouguer gravity values, with the corresponding elevation along the transect. The transect depicts important stratigraphic sequences and formations, and structural relations. Red lines indicate faults and black arrows indicate relative motion along the fault. 2-D seismic profiles location along the transect are indicated by dashed blue and green rectangles. The Semail Ophiolites frontal thrust is delineated at the sole of the Hawasina Sediments, and a bold red line indicates the sole of the igneous ophiolite body. Dip information of the Jabal Akhdar Mountain are shown along the surface of the structure. The transect also shows locations of deployed seismic stations (yellow triangles) and the corresponding, projected, impinging locations are shown as error bars.

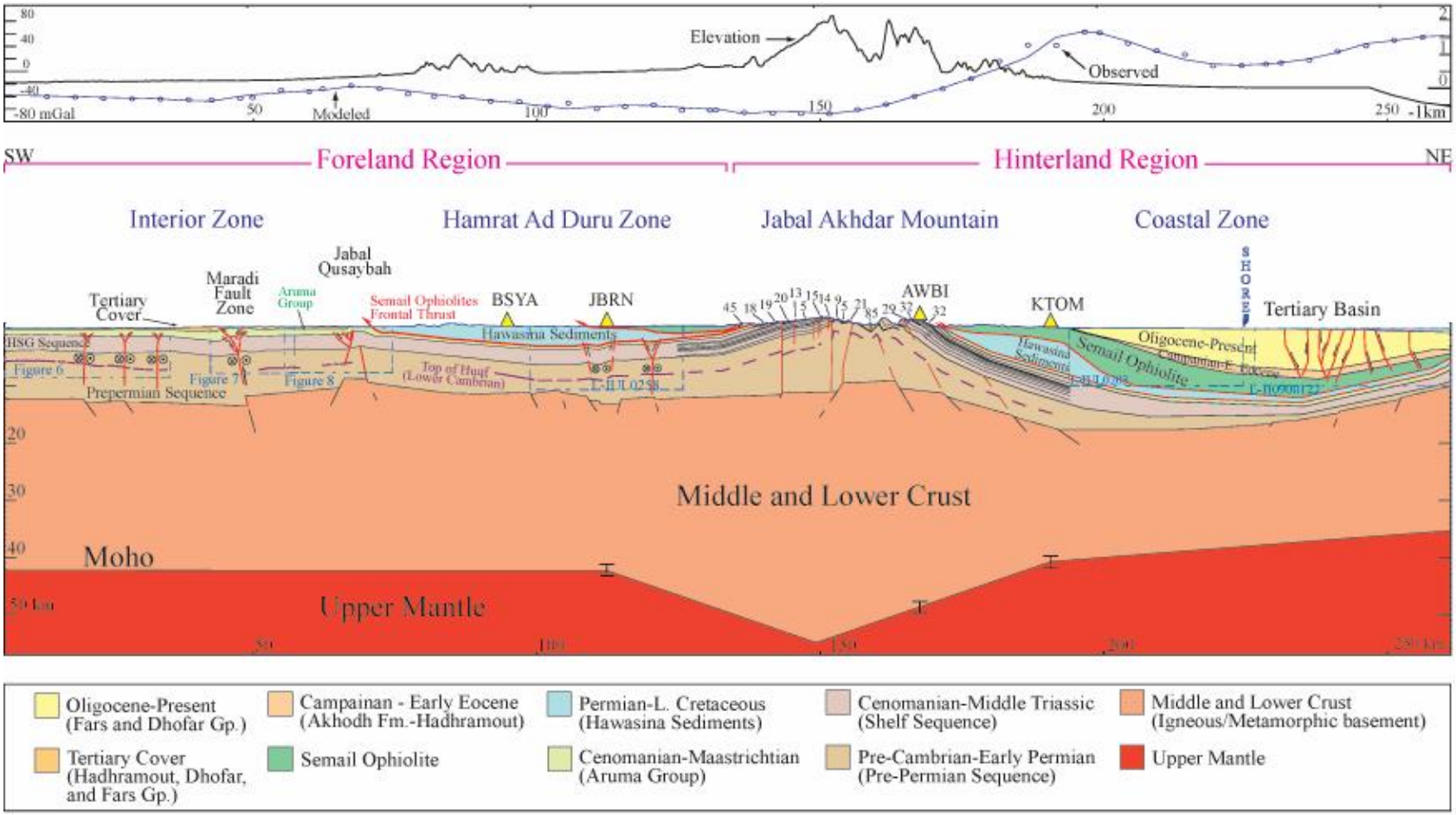
Elevation
Observed
Modeled
-80 mGal
SW
Foreland Region
Hinterland Region
NE
Interior Zone
Hamrat Ad Duru Zone
Jabal Akhdar Mountain
Coastal Zone
Tertiary Cover
Maradi Fault Zone
Aruma Group
Jabal Qusaybah
Semail Ophiolites
Frontal Thrust
BSYA
JBRN
AWBI
KTOM
SHORE
Tertiary Basin
Hawasina Sediments
Semail Ophiolite
Oligocene-Present
Campainan-E. Eocene
HSG Sequence
Figure 6
Figure 7
Figure 8
Prepermian Sequence
Top of Huqf (Lower Cambrian)
Middle and Lower Crust
Moho
Upper Mantle
Oligocene-Present (Fars and Dhofar Gp.)
Campainan - Early Eocene (Akhodh Fm.-Hadhramout)
Permian-L. Cretaceous (Hawasina Sediments)
Cenomanian-Middle Triassic (Shelf Sequence)
Middle and Lower Crust (Igneous/Metamorphic basement)
Tertiary Cover (Hadhramout, Dhofar, and Fars Gp.)
Semail Ophiolite
Cenomanian-Maastrichtian (Aruma Group)
Pre-Cambrian-Early Permian (Pre-Permian Sequence)
Upper Mantle

southern side of Jabal Qusaybah anticline (Figure 2.8). Reflectors below the HSG Sequence, at ~2.0 s (twt) show no conclusive evidence of neither folding nor faulting, which infer a salt supported structure.

Farther east, the Maradi Fault Zone is observed to act as a barrier, where NR-1, and HR-1 wells, located north of the MFZ include no deposits of the Early Eocene-Pliocene Hadhramout and the Fars Group (Tertiary cover) (see Figures 2.5 and 2.17). Also, in the NE side of the MFZ, the top of HSG Sequence is elevated at ~900 meters relative to the SW side of the fault. The absence of the Tertiary cover NE of MFZ could be the result of two possibilities: a differential uplift or diffrential subsidence. Where in the former the Tertiary cover was removed by erosion in the higher NE and in the latter case the Tertiary cover was not deposited at all in the NE side of MFZ. Based on our observation, we interpret the MFZ to be a basement associated fault with two styles of deformation: a reverse faulting component as a pre-MFZ (possibly earlier in the late Cretaceous) and a strike-slip fault component dated as a Plio-Pliestocene event by Hanna and Nolan (1989) (see Figures 2.7 and 2.17).

Consistent observations, in different seismic profiles (some of which not included in Figure 2.3), show flower structures that form a NW-SE wrench fault system affecting the entire HSG Sequence, the Muti Formation, and the Aruma Group in the Interior Zone and the Hamrat Ad Duru Zones (Figures 2.6, 2.7, and 2.8). In most seismic profiles the flower structure offsets are traced to continue to the overlying Muti Formation and Fiqa Formation but in some cases faulting within the Fiqa Formation becomes ambiguous as shown in Figure 2.6. In this study, we interpret the Fahud and Natih structures to have developed as a double plunging pericline structures possibly associated with the strike slip movement along the already weakened zone of the pre-MFZ. The MFZ is parallel to the system of NW-SE wrench faults (Figure 2.17). The structures of Natih and Fahud strikes are at ~20$^{o}$ with respect

**Figure 2.17**: A geology map extracted from 1:250,000 scale Oman Geological Maps, (1992) of part of the foreland region (see Figure 2.3 for location). The map view depicts the structural relations between the Maradi Fault Zone (MFZ) and the structures of Natih and Fahud. Abbreviated text shown in the legend stands for the following: MPlbz: Miocene-Pliocene Berzman Formation, Mda: Middle Miocene Dam Formation, Edm: Middle Eocene Dammam Formation, Ers: Early Eocene Rus Formatio, Eur: Early Eocene Um Er Radhuma Formation, LKfq: Late Cretaceous Fiqa Formation, Ant: Albian Natih Formation, and HW: Hawasina Sediments. The map shows locations of selected, depth converted section, with no vertical exaggeration. The depth sections are used to infer subsurface structural relation between MZF, Fahud and Natih structures with NW-NE wrench faulting system, observed as flower structures in each section. Within each depth section, red lines denote faults, with black arrows showing the relative motion. Blue lines delineate random reflector to enhance the structural attributes shown in each section. Section-A and Section-B are interpreted as positive flower structures while Section-C as a negative flower structure.

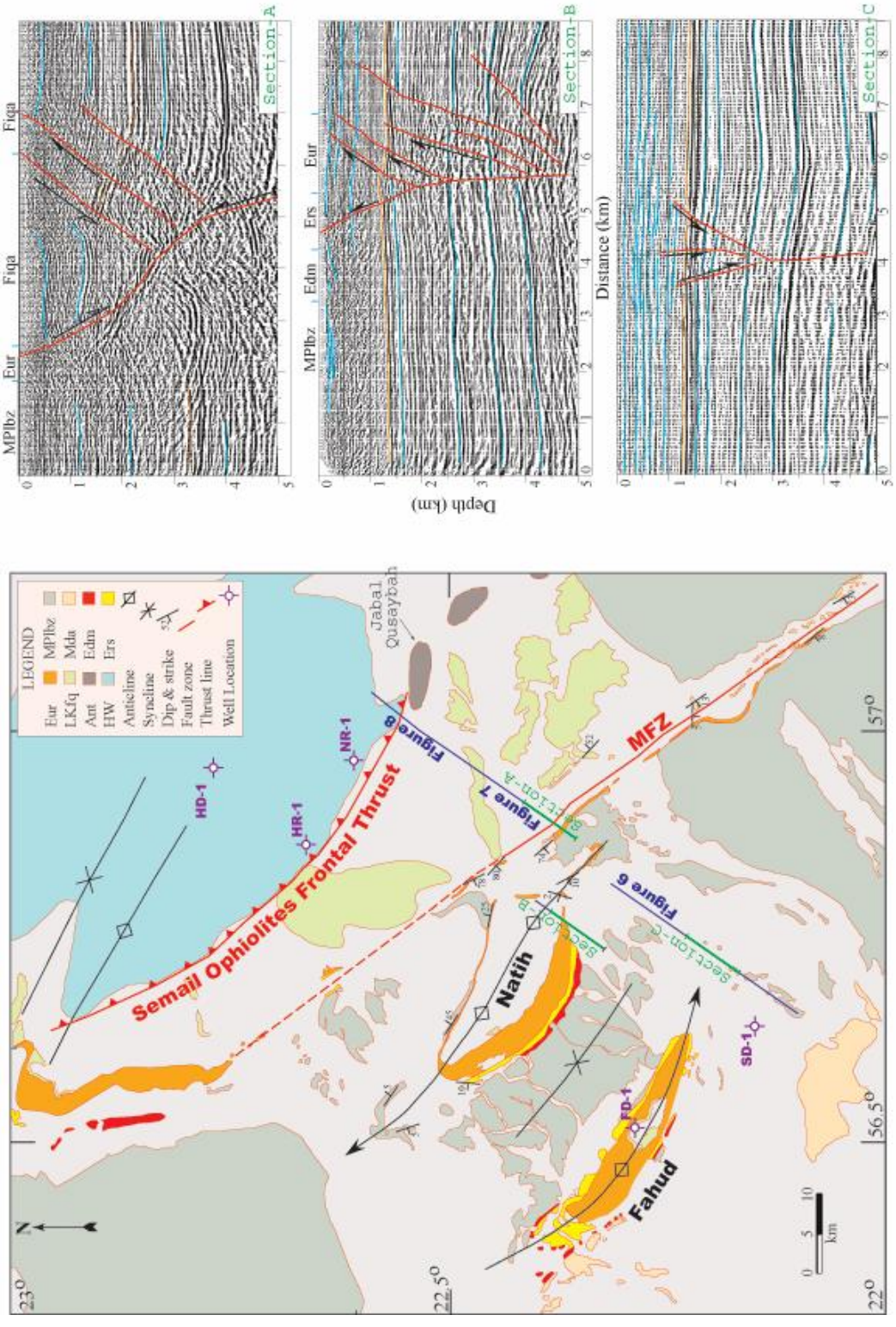
Section-A
Section-B
Section-C
MPlbz
Eur
Figa
Edm
Ers
Depth (km)
Distance (km)
LEGEND
MPlbz
Mda
Edm
Ers
Eur
LKfq
Ant
HW
Anticline
Syncline
Dip & strike
Fault zone
Thrust line
Well Location
Semail Ophiolites Frontal Thrust
MFZ
Natih
Fahud
Jabal Qusaybah
HD-1
HR-1
NR-1
SD-1
FD-1
Figure 8
Figure 7
Figure 6
Section-A
Section-B
Section-C
23°
22.5°
22°
57°
56.5°
0 5 10
km

to the NW-SE fault system (Figure 2.17). This wrench fault system is observed in seismic lines throughout the foreland region which implies a regional event, possibly transcurrent. In Figure 2.17, Section-B intersects the southeastern end of Natih structure that shows a positive flower structure. As seen in the geology map of Figure 2.17 the deformation of the Natih and Fahud structures includes the Miocene-Pliocene Berzman Formation that overlies the Hadhramout group. The timing of this event is in agreement with earlier work by Hanna and Nolan (1989). These authors date the Maradi Fault Zone as a reactivated Plio-Pliestocene, right lateral strike-slip fault. Therefore, we suggest that the Tertiary deformation in the foreland region is largely transcurrent with no conclusive evidence of a major compressioanl event during Tertiary times (Figure 2.17).

**The Hinterland Region**

The present day Jabal Akhdar Mountain and the northern Oman Mountains pose three important questions: (1) What is the support mechanism of the present-day topography? (2) What type of structural style is involved in the architectural formation of Jabal Akhdar Mountain, and its timing? And (3) What is the timing of uplift of the Northern Oman Mountain?

In this study we conclusively answer (1) and propose a solution for (3). We are not able to provide specific solutions for question (2) for it requires more detailed structural analysis and deeper seismic imaging, but we do propose a mechanism for the formation of the Jabal Akhdar Mountain.

Answering question (1), Moho depths determined from data produced by the seismic stations JBRN, AWBI, and KTOM delineate the root beneath the Jabal Akhdar Mountain. The root beneath the Jabal Akhdar Mountain is confirmed by gravity modeling. Station AWBI, which shows the deepest Moho (48-51 km) of the

three locations, does not correspond with the highest elevation in the mountain. As shown in Figure 2.16, the highest topography coincides with the lowest gravity point, located 10 km southwest of AWBI station. Assuming an isostatically compensated Airy model, the highest elevation, 3000 m, would correspond to about 55 km Moho depth (Figure 2.16). Manghnani and Coleman (1981) and Ravaut et al. (1997) gravity modeling results gave a ~43 km and ~47 km maximum depth below the structure of the Jabal Akhdar Mountain, respectively, which is shallower than Moho depth found beneath AWBI station. Both Manghnani and Coleman (1981) and Ravaut et al. (1997) used a density of 2.9 g/cm$^3$ average for the continental crust, which we find too high. Our gravity modeling differ with both authors as well, where our initial model includes more constrains on the upper 8 km of the sedimentary section and includes determined Moho depths across the Jabal Akhdar Mountain, using new seismological observations.

We associate the initiation of the thickening of the crust below the Jabal Akhdar Mountain to the Late Cretaceous Semail Ophiolite emplacement where this deformational event had a large southward compressional component.

Addressing question (2): two styles of deformation have been proposed to form the present-day Jabal Akhdar Mountain by a fault bend fold (Michard et al., 1984; Cawood et al., 1990; Hanna, 1990) or by a propagation fault fold (Mount et al., 1998). We interpret the present-day structure of Jabal Akhdar Mountain as the result of deformation concentrated along zones of weakness, perhaps shear zones, related to the Permian rifting event. We infer the initiation of the development of the Jabal Akhdar structure to be contemporaneous with the third stage of the Semail Ophiolite emplacement, where the allochthonous load has finally collided with the margin edge. Nolan et al. (1990) concluded that the Alkhawd Formation mapped around the flanks of Jabal Nakhl and Saih Hatat includes clast composition that records the unroofing

and erosion of the Saih Hatat and Jabal Akhdar culminations. The proposed timing is also deduced collectively from different observations described below.

Gravity modeling showed that the basement top in the core of the Jabal Akhdar structure is at ~9 km depth, coinciding with the extensively deformed pre-Permian Sequence, showing stratal dips of 85$^{o}$ (Figure 2.16). The exposed HSG Sequence flanking the pre-Permian Sequence does not show extreme deformation, but shows gently dipping strata in the southern limb, and steeper dipping strata in the northern limb of Jabal Akhdar Mountain. The southern limb strata average dip is ~15$^{o}$ S, and the northern limb strata average dip is ~28$^{o}$ N. Also, gravity modeling shows considerable thinning of the pre-Permian Sequence, in the northern limb of the Jabal Akhdar Mountain. This sudden decrease in the pre-Permian Sequence thickness at the northern limb could be associated with Permian rifting event forming the southeastern edge of the Arabian Plate margin. Also shown in Figure 2.16 is that a considerable load of the Semail Ophiolite and the Hawasina Sediments occur north of the mountain which possibly contribute to the steepness of the northern limb of the mountain. Note the density thickness trade-off between the ophiolite and the Hawasian sediments in the coastal zone.

Addressing question (3): Based on the observation of Figures 2.9 and 2.10 we infer a major uplift episode starting in the Late Oligocene time. This conclusion is confirmed by a number of observations. In line IUL0205 (Figure 10) north of the Jabal Akhdar Mountain, interpretation of seismic stratigraphic units show 25$^{o}$-30$^{o}$N dipping strata of the Alkhawd Formation and the Hadhramout Group (Tertiary Cover). This observation provides a timing of the Northern Oman Mountain episodic uplift in the Late Oligocene period. This timing is in agreement with fission track dating of the uplift of the structure of the Jabal Akhdar Mountain by Mount et al. (1998). Moreover, the Hamrat Ad Duru Zone seismic data show (Figure 2.9) southerly dipping reflectors

of the Fiqa Formation (forming downlaps) indicative of continued uplift in the mountains, hence tipping the reflectors towards the south. This observation indicates that the mountain uplift has continued after the Maastrichtian, i.e., after the deposition of Fiqa Formation. This uplift episode is shown to affect the Interior Zone but with lesser magnitude than that of the Hamrat Ad Duru and the Mountain Zones. In summary, the uplift and unroofing of the Oman Mountain possibly started within the Late Cretaceous period indicated by the intermontain deposits of Alkhawd Formation and its equivalent in the Coastal Zone (Figure 2.10). The major uplift initiated in the Late Oligocene time is probably related to nearby plate boundary processes including the Zagros collision zone and the Makran subduction system. The end of the Cretaceous and Tertiary boundary is an important time period where it should be considered. Due to the lack of information about this particular boundary especially well data, we were unable to cover it adequately in our discussion both in the foreland region and the Coastal Zone. However, it is important to determine the unconformity continuity or its absence at the subsurface in the Coastal Zone.

Finally, the offshore area shows the development of an extensive sedimentary basin that postdates the Oligocene, which could be the extension of the Sohar basin documented by Ravaut et al. (1998). The basin extends northwards for approximately 60 km at the end of the crustal model of Figure 2.16. The basin is deepest along the shoreline, reaching a depth of about 7 km below sea level. The northernmost seismic section in the offshore area is primarily characterized by gravity faults (Figure 2.16).

## CONCLUSIONS

Four main results are presented in this study. (1) The southeastern Arabian continental crust averages about ~40 km thickness in the foreland region, ~50 km beneath the Jabal Akhdar Mountain, and ~35 km in the Coastal Zone. (2) Based on

gravity modeling, the pre-Permian Sequence in the core of the Jabal Akhdar Mountain is estimated to be ~9 km thick. This observation conforms well with most structural models of the Jabal Akhdar Mountain that require thickening, either by duplexing, blind thrust faulting, or decollement below the core and the southern limb of the Jabal Akhdar Mountain. (3) Based on surface, subsurface and gravity modeling, the Nakhl Ophiolite block is found to extend beyond the shoreline for approximately 80 kilometers from its most southern surface outcrop. The Nakhl block averages in thickness ~5 km, whereas the ophiolite body south of the Jabal Akhdar Mountain is found to have a maximum thickness of 1 km. The underlying unit of the Hawasina sediments is found to average in thickness between 2-3 km in the Hamrat Ad Duru Zone and 2 km in the Coastal Zone. (4) Basement-related wrench faulting system is mapped in the foreland region striking NW-SE, and predominantly transtensional. These wrench faults are found to offset preexisting older structures such as the Salakh-Madmar range. Furthermore, we conclude that the Tertiary period does not show any major compressional events within the foreland region.

**ACKNOWLEDGMENTS**

The authors would like to thank the Oman Ministry of Oil and Gas in allowing the access to seismic reflection and well data in the study area. In particular, we thank the Department of Minerals for their support throughout the study and also in permitting us to use the gravity data. We also thank the Petroleum Development Oman Company for providing and assistance in obtaining the seismic reflection and well data. The receiver function data were made possible by the generosity of the Department of Earth Sciences, Sultan Qaboos University. The recorded data are the result of the dedicated staff of the Earthquake Monitoring Project under the leadership of Waris Warsi. Special thanks to Samir Hanna, at the Department of Earth Sciences, Sultan Qaboos University, for his valuable comments and suggestions on the manuscript. We also thank our colleagues at Cornell University: Graham Brew, Francisco Gomez, Alexander Calvert, Marisa Vallve, Carrie Brindisi, Christine Sandvol, David Steer, and Khaled Al-Damegh for their assistance and constructive comments throughout this study.

**REFERENCES**

Al-Harthy, M.S., R.G. Coleman, M.W. Hughes-Clarke, and S.S. Hanna 1991. Tertiary basaltic intrusions in the Central Oman Mountains. In TJ. Peters, A. Nicolas and R.G. Coleman (Eds), Ophiolite Genesis and Evolution of the Oceanic Lithosphere, Ministry of Petroleum and Minerals, Sultanate of Oman, p. 675-682.

Amoco Oman Petroleum Company, unpublished report, A.O.P., 1985. Barka-1 well.

Badri, M. 1990. Crustal structure of central Saudi Arabia determined from seismic refraction profiles. Tectonophysics, v. 185, no. 3-4, p. 357-374.

Bechennec, F., J. Le Metour, J.-P. Platel and J. Roger 1994. Doming and down-warping of the Arabian Platform in Oman in relation to Eoalpine tectonics. In M.I. Al-Husseini (Eds.), Middle East Petroleum Geosciences, GEO'94, Gulf PetroLink, 2, p. 167-178.

Bechennec, F., M Beurrier, G. Hutin and D. Rabu, 1986a. Geological map of Barka. Ministry of Petroleum and Minerals, Sultanate of Oman.

Bechennec, F., M. Beurrier, G. Hutin and D. Rabu, 1986b. Geological map of Bahla. Ministry of Petroleum and Minerals, Sultanate of Oman.

Beurrier, M., F. Bechennec, G. Hutin and D. Rabu, 1986. Geological map of Rustaq. Ministry of Petroleum and Minerals, Sultanate of Oman.

Boote, D.R.D., D. Mou and R.I. Waite 1990. Structural evolution of the Suneinah foreland, central Oman Mountains. In A.H.F. Robertson, M.P. Searle and A.C. Rice (Eds.), The Geology and Tectonics of Oman Mountains, Geological Society Special Publication, 49, p. 397-418.

Boudier, F., J.L. Bouchez, A. Nicolas, M. Cannat, G. Ceuleneer, M. Misseri and R. Montigny 1985. Kinematic of oceanic thrusting in the Oman Ophiolite: Model for plate convergence. Earth and Planetary Sciences Letters, v. 75, p. 215-222.

Boudier, F. and R.G. Coleman 1981. Cross section through the peridotite in the Semail Ophiolite, Southeastern Oman Mountains. Journal of Geophysical Research, v. 86, no. B4, p. 2573-2592.

Burdick, L.J. and A.C. Langston 1977. Modeling crustal structure through the use of converted phases in teleseismic body-wave forms. Bulletin of the Seimological Society of America, v. 67, no. 3, p. 677-691.

Cassidy, J.F. 1992. Numerical experiments in broadband receiver function analysis. Bulletin of the Seimological Society of America, v. 82, no. 3, p. 1453-1474.

Cawood, P.A., F.K. Green and T.J. Calon 1990. Origin of culmination within the Southeast Oman Mountains at Jabal Majhool and Ibra Dome. In A.H.F. Robertson, M.P. Searle and C. Rice (Eds.), The Geology and Tectonics of the Oman Region, Geological Society Sepecial Publication, 49, p. 429-445.

Chevrel, S., F. Bechennec, J. Le Metour, J. Roger and R. Wyns 1992. Geological map of Jubuayl Fahud. Ministry of Petroleum and Minerals, Sultanate of Oman.

Christensen, N.I. and J.D. Smewing 1981. Geology and seismic structure of the Northern section of the Oman Ophiolite. Journal of Geophysical Research, v. 86, no. B4, p. 2545-2555.

Clayton, R.W. and R.A. Wiggins 1976. Source shape estimation and deconvolution of teleseismic body waves. The Geophysical Journal of the Royal Astronomical Society, v. 47, p. 151-177.

Coleman, R.G. 1981. Tectonic setting for Ophiolite obduction in Oman. Journal of Geophysical Research, v. 86, no. B4, p. 2497-2508.

El-Shazly, A.K. and R.G. Coleman 1990. Metamorphism in the Oman Mountains in relation to the Semail Ophiolite emplacement. In A.H.F. Robertson, M.P. Searle and A.C. Ries (Eds.), Geology and Tectonics of the Oman Region, Geological Society Special Publication, 49, p. 473-493.

Gardner, G.H., L.W. Gardner and A.R. Gregory 1974. Formation velocity and density - the diagnostic basic for stratigraphic traps. Geophysics, v. 39, p. 770-780.

Glennie, K.W., M.G.A. Boeuf, M.W.H. Clarke, M. Moody-Stuart, W.F.H. Pilaar and B.M. Reinhardt 1973. Late Cretaceous nappes in Oman Mountains and their geologic evolution. Bulletin of the American Association of Petroleum Geologists, v. 57, p. 5-26.

Hanna, S.S. 1990. The Alpine deformation of the central Oman Mountains. In A.H.F. Robertson, M.P. Searle and A.C. Ries (Eds.), The Geology and Tectonics of the Oman Region, Geological Society Special Publication, 49, p. 341-359.

Hanna, S.S. and S.C. Nolan 1989. The Maradi fault zone: evidence of Late Neogene tectonics in the Oman mountains. Journal of the Geological Society, London, v. 146, p. 867-871.

Hanna, S.S. and J.D. Smewing 1996. The stratigraphy and structure of the Madamar-Salakh-Qusaybah range and Natih-Fahud area in the Oman Mountains. Journal of Science and Technology, Sultan Qaboos University, Oman, v. 1, p. 1-19.

Hopson, C.A., R.G. Coleman, R.T. Gregory, J.S. Pallister and E.H. Baily 1981. Geologic section through the Semail Ophiolite and associated rocks along the Muscat-Ibra transect, Southeastern Oman Mountains. Journal of Geophysical Research, v. 86, p. 2527-2544.

Le Metour, J., F. Bechennec and J. Roger 1994. Late Permian birth of the Neo-Tethys and development of its southern continental margin in Oman. Gulf PetroLink, Bahrain, p. 643-654.

Le Metour, J., J.C. Michel, F. Bechennec, J.P. Platel and J. Roger 1995. Geology and mineral wealth of the Sultanate of Oman. Ministry of Petroleum and Minerals Sultanate of Oman, 285 p.

Lippard, S.J. 1983. Cretaceous high pressure metamorphism in NE Oman and its relation to subduction and ophiolite nappe emplacement. Journal of the Geological Society of London, v. 140, p. 97-104.

Manghnani, M.H. and R.G. Coleman 1981. Gravity profiles across the Semail Ophiolite, Oman. Journal of Geophysical Research, v. 86, no. B4, p. 2509-2525.

Mann, A. and S.S. Hanna 1990. The tectonic evolution of pre-Permian rocks, Central and Southeastern Oman Mountains. In A.H.F. Robertson, M.P. Searle and A.C. Ries (Eds.), The Geology and Tectonics of the Oman Region, Geological Society Special Publication, 49, p. 307-325.

Mattes, B.W. and S.C. Morris 1990. Carbonate/evaporite deposition in the Late Precambrian - Early Cambrian Ara Formation of Southern Oman. In A.H.F. Robertson, M.P. Searle and A.C. Ries (Eds.), The Geology and Tectonics of the Oman Region, Geological Society Special Publication, 49, p. 617-636.

Michard, A., J.L. Bouchez and M. Ouazzani-Touhami 1984. Obduction-related planar and linear fabrics in Oman. Journal Structural Geology, v. 6, p. 39-49.

Mooney, W.D., M.E. Gettings, H.R. Blank and J.H. Healy 1985. Saudi Arabian seismic-refraction profile: a travel time interpretation of crustal and upper mantle structure, Tectonophysics, v. 111, p. 173-246.

Mount, V.S., R.I.S. Crawford and S.C. Bergman 1998. Regional structural style of the central and southern Oman Mountains: Jebel Akhdar, Saih Hatat, and the northern Ghaba Basin. GeoArabia, v. 3, no. 4, p. 475-489.

Nicolas, A., F. Boudier and B. Ildefonse 1996. Variable crustal thickness in the Oman ophiolite: implication for oceanic crust. Journal of geophysical research, v. 101, no. B8, p. 17,941-17,950.

Nolan, S.C., P.W. Skelton, B.P. Clissold and J.D. Smewing 1990. Maastrichtian to early Tertiary stratigraphy and palaeogeography of the Central and Northern Oman Mountains. In A.H.F. Robertson, M.P. Searle and A.C. Ries (Eds.), The Geology and Tectonics of the Oman Region, Geological Society Special Publication, 49, p. 495-519.

Pallister, J.S. and C.A. Hopson 1981. Semail Ophiolite plutonic suite: Field relations, phase variation, cryptic variation and layering, and model for a spreading ridge magma chamber. Journal of Geophysical Research, v. 86, no. B4, p. 2593-2644.

Rabu, D., F. Bechennec, M Beurrier and G. Hutin, 1986. Geological map of Nakhl. Ministry of Petroleum and Minerals, Sultanate of Oman.

Ravaut, P. 1997. Le Anomalies De Pesanteur en Oman Implications sur la structure et l'evolution tectonique de la chaine nord-omanaise, Universite Montpellier, Montpellier. Ph.D. Dissertation. p. 255.

Ravaut, P., D. Carbon, J-F. Ritz, R. Bayer, H. Philip 1998. The Sohar Basin, western Gulf of Oman: description and mechanisms of formation from seismic and gravity data. Marine and Petroleum Geology, v. 15, no. 4, p. 359-377.

Ravaut, P., R. Bayer, R. Hassani, D. Rousset and A.A. Yahya'ey 1997. Structure and evolution of the northern Oman margin: gravity and seismic constraints over the Zagros-Makran-Oman collision zone. Tectonophysics, v. 279, p. 253-280.

Ravaut, P. and W. Warsi, 1997. Bouguer Anomaly Map of Oman. Ministry of Petroleum and Minerals, Sultanate of Oman, Muscat.

Robertson, A. 1987. The transition from a passive margin to an upper Cretaceous foreland basin related to ophiolite emplacement in the Oman Mountains. Geological Society of America Bulletin, v. 99, no. 11, p. 633-653.

Sandvol, E., D. Seber, M. Barazangi, F. Vernon, R. Mellors and A. Al-Amri 1998a. Lithospheric Seismic Velocity Discontinuities beneath the Arabian Shield. Geophysical Research Letters, v. 25, no. 15, p. 2873-2876.

Sandvol, E., D. Seber, A. Calvert and M. Barazangi 1998b. Grid search modeling of receiver functions: Implications for crustal structure in the Middle East and North Africa. Journal of Geophysical Research, v. 103, no. B11, p. 26,899-26,917.

Searle, M. and J. Cox 1999. Tectonic setting, origin, and obduction of the Oman ophiolite. Geological Society of America Bulletin, v. 111, no. 1, p. 104-122.

Shelton, A.W. 1990. The interpretation of gravity data in Oman: Constraints on the Ophiolite emplacement mechanism. In A.H.F. Robertson, M.P. Searle and A.C.

Rice (Eds.), The Geology and Tectonics of the Oman Region, Geological Society of London, 49, p. 459-471.

Warbuton, J., T.J. Burnhill, R.H. Graham and K.P. Isaac 1990. The Evolution of the Oman Mountains foreland basin. In A.H.F. Robertson, M.P. Searle and A.C. Ries (Eds.), The Geology and Tectonics of Oman Region, Geological Society Sepecial Publication, 49, p. 419-427.

Wyns, R., F. Bechennec, S. Chevrel, J. Le Metour, and J. Roger 1992. Geological map of Nazwa. Ministry of Petroleum and Minerals, Sultanate of Oman.

Zandt, G. and C.J. Ammon 1995. Continental Crust Composition Constrained by the Measurement of the Crustal Poisson's ratio. Nature, v. 374, no. 9, p. 152-154.

# CHAPTER THREE

## Tomographic Pn velocity and anisotropy structure beneath the Anatolian plateau (eastern Turkey) and the surrounding regions*


### ABSTRACT

We use Pn phase travel time residuals to invert for mantle lid velocity and anisotropy beneath northern Arabia-eastern Anatolia continent-continent collision zone. The primary phase data were obtained from the temporary 29-station broadband PASSCAL array of the Eastern Turkey Seismic Experiment. These data were supplemented by phase data from available stations of the Turkish National Seismic Network, the Syrian National Seismic Network, the Iranian Long Period Array, and other stations around the southern Caspian Sea. In addition, we used carefully selected catalog data from the International Seismological Centre and the National Earthquake Information Center bulletins. Our results show that low (< 8 km/s) to very low (< 7.8 km/s) Pn velocity zones underlie the Anatolian plateau, the Caucasus, and northwestern Iran. Such low velocities are used to infer the presence of partially molten to absent mantle lid beneath these regions. In contrast, we observed a high Pn velocity zone beneath northern Arabia directly south of the Bitlis-Zagros suture indicating the presence of a stable Arabian mantle lid. This sharp velocity contrast across the suture zone suggests that Arabia is not underthrusting beneath the Anatolian plateau and that the surface suture extends down to the uppermost mantle.


---

*Willl be submitted to Geophysical Research Letters as "Tomographic Pn velocity and anisotropy structure beneath the Anatolian plateau (eastern Turkey) and the surrounding region" by Ali I. Al-Lazki, Eric Sandvol, Dogan Seber, Muawia Barazangi, Niyazi Turkelli, and Randa Mohamad.

## INTRODUCTION

This study focuses on the continent-continent collision zone between the Arabian and Eurasian plates and the resultant Anatolian-Iranian plateau (Figure 3.1). Crustal processes at the Arabian-Eurasian convergent boundary and the nearby regions received extensive analysis (e.g., Dewey et al., 1986; Reilinger et al., 1997). However, the state of the mantle lithosphere and lithospheric dynamics of this young continent-continent collision zone are still debated (e.g., McKenzie, 1972; Rotstein and Kafka, 1982; Dewey et al., 1986).

The tectonic history of the region is complex. A two-phase extension episode in Late Eocene and Early Pliocene (Hempton, 1987) initiated the split of the Arabian plate from the African plate along the Red Sea and the Gulf of Aqaba regions. Arabia's continued northward motion and further separation from the African plate along the Dead Sea Fault (DSF) in the Miocene/Pliocene resulted in the reorganization of relative plate motions in the Anatolian Plateau (Bozkurt, 2001). In Early Pliocene, this resulted in the westward extrusion of the Anatolian plate along the North Anatolian Fault (NAF) and the East Anatolian Fault (EAF) zones (McKenzie, 1972; Sengor and Yilmaz, 1981; Sengor et al., 1985). Farther north, the Lesser and Greater Caucasus regions which are believed to partially accommodate the Arabian plate northward motion (Philip et al., 2001) are undergoing thrust and strike-slip deformation.

Terminal suturing of the Arabian and Eurasian plates along the Bitlis Suture (BS) is thought to have happened in the Middle Miocene (Yilmaz, 1993). The Arabian-Eurasian collision is associated with extensive volcanism in eastern Anatolia, starting in the Late Miocene and continuing to historical times (Yilmaz, 1990; Keskin et al., 1998). The source of this volcanism is possibly derived form the lower portion of the lithospheric mantle (Pearce et al., 1990). GPS data (Reilinger et al., 1997) have shown that the Anatolian plate is escaping to the west and that there is horizontal

**Figure 3.1.** Simplified tectonic boundaries (black lines) of northern Arabian and Eurasian plates atop hit counts base-map for every 1/6$^{o}$ cell size. 1 = White triangles are Eastern Turkey Seismic Experiment (ETSE) stations, and black triangles are Syrian National Seismic Network (SNSN) stations; white hexagons are Turkish National Seismic Network stations, black hexagons are temporary stations of the southern Caspian experiment; white stars are the temporary station of the Iranian Long Period Array (ILPA); and open triangles are other local stations obtained from the ISC catalouge. 2 = Thrust, and 3 = strike-slip fault boundaries. BS = Bitlis Suture and ZS = Zagros Suture, GC = Greater Caucasus, LC = Lesser Caucasus, NAF = North Anatolian Fault, EAF = East Anatolian Fault, DSF = Dead Sea Fault.

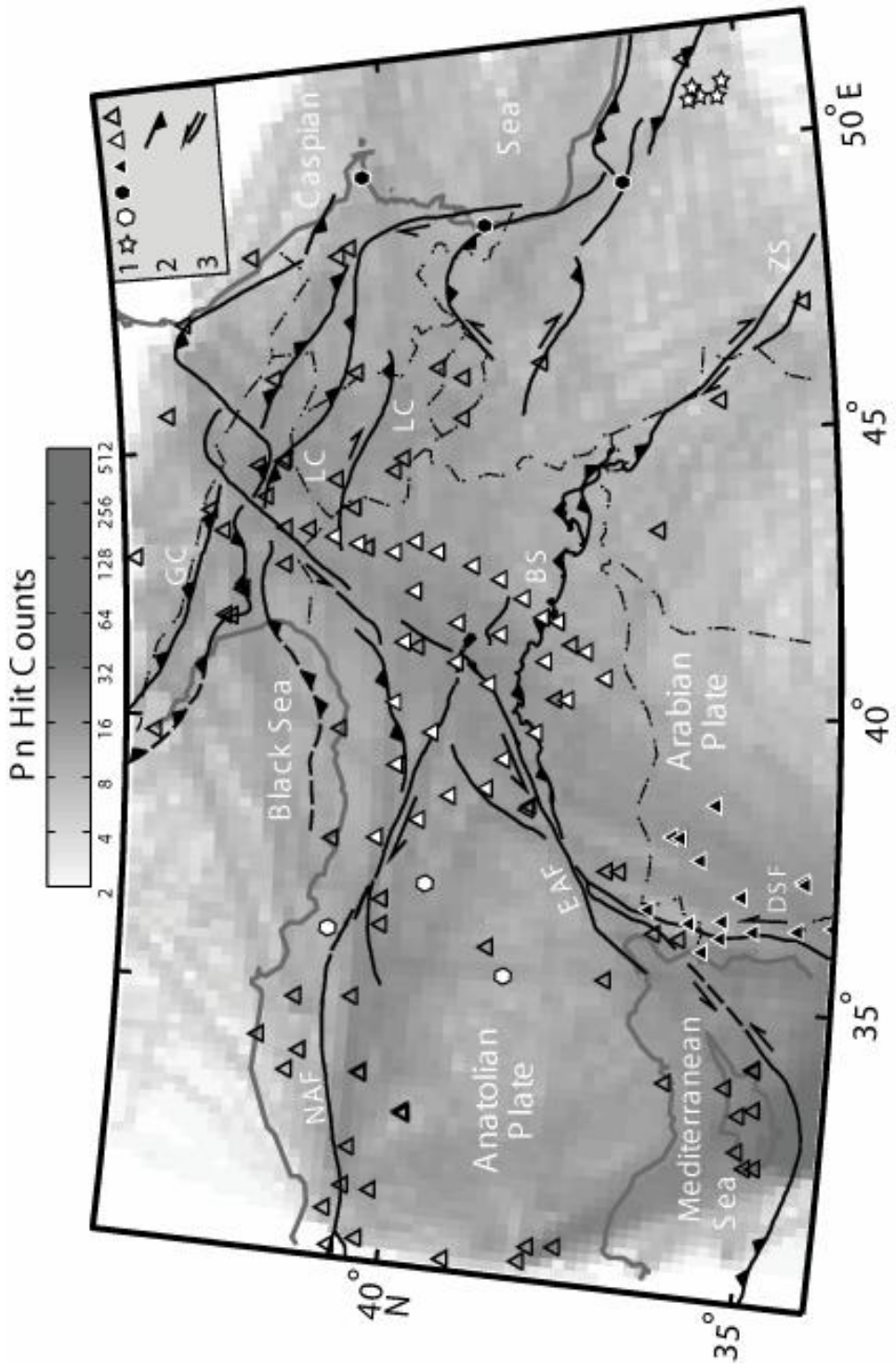
Pn Hit Counts
2
4
8
16
32
64
128
256
512
1
2
3
Caspian
Sea
Black Sea
Anatolian
Plate
Arabian
Plate
Mediterranean
Sea
NAF
EAF
DSF
GC
TC
LC
BS
ZS
40°
N
35°
40°
45°
50°E
35°

shortening across eastern Anatolia. The contribution of the mantle lid to convergence dynamics across the collision zone and the extent of Arabia's underthrusting beneath Eurasia are still not well-understood. This study aims at providing additional constraints for the models of the upper mantle dynamics in the region. Our results provide a much higher resolution Pn velocity model with anisotropy that significantly improves an earlier Pn velocity model of Hearn and Ni (1994) beneath the Anatolia-Arabia continent-continent collision zone and its surroundings.

## DATA AND INVERSION METHOD

We utilized two major Pn phase data sets in this study. The fewer, but high quality data are obtained by manually reading 7,414 Pn phases from 29 PASSCAL broadband stations of the Eastern Turkey Seismic Experiment (ETSE), 5 short period stations of the Turkish National Seismic Network, 20 short period stations of the Syrian National Seismic Network, 5 broadband stations in the southern Caspian region, and 5 stations of the Iranian Long Period Array (ILPA) located in northern Iran (Figure 3.1). The uncertainty of the Pn phase readings is less than one second. To include these data in our inversion we required a minimum of 10 different events per station and a minimum of 5 stations recording a single event. The larger quantity, but probably less reliable data were also obtained from the existing seismic catalogues of the International Seismological Centre (ISC) and the National Earthquake Information Center (NEIC) to provide ray coverage where the high quality data were sparse. In this case, we used strict data selection criteria to select Pn phase data from these catalogues. We screened phase data for potential location errors by using a maximum station gap of $150^{o}$, a minimum of 20 recording stations per event, and less than 10 seconds of location residuals for each station. A total of about 51,000 Pn phase data

were then used in the Pn tomography inversion for the area covering $30^o$ to $55^o$ E and $30^o$ to $45^o$ N.

A tomography method developed by Hearn (1996) is used to invert for Pn wave velocity, anisotropy, as well as station and event delays. This method uses a least squares algorithm (Paige and Saunders, 1982) to iteratively solve for all event-station pairs to obtain slowness, anisotropy, and station and event delays (Hearn, 1996). The method includes damping parameters on both velocity and anisotropy to regularize solution and reduce noise artifacts. P-wave travel time residuals (<10 s) from sources at $1.8^o$ to $16^o$ were used to invert for uppermost mantle velocity and anisotropy models at a $1/6^o$ cell size. For this tomography inversion we used mean uppermost mantle velocity of 8 km/s and assumed a crustal thickness of 35 km and a crustal velocity of 6.2 km/s. Figure 3.1 shows seismic stations atop hit counts map for the study region (Figure 3.1).

## TOMOGRAPHY RESULTS

A broad zone of low (< 8 km/s) Pn velocity underlies northwestern Iran, Turkey, and the Caucasus region. Within this broad low velocity anomaly, pockets of very low (< 7.8 km/s) Pn velocity zones are observed in the Caucasus and eastern Anatolia (Figure 3.2a). On the other hand, high Pn velocities underlie most of northern Arabia, the Caspian Sea and Azerbaijan (eastern Greater Caucasus), the Black Sea, and northeastern Mediterranean Sea (Figure 3.2a). In addition, smaller zones with high Pn velocity are observed in areas in northwestern Iran, central Anatolia plate, and central Greater Caucasus (Figure 3.2a).

To test the resolution of our tomographic inversion and the reliability of the anomalies obtained (Figure 3.2a) we constructed a synthetic checkerboard model with alternating high and low velocities in $2^o$x$2^o$ cells. We added 1 second random noise to

**Figure 3.2. (a)** A map showing inverted tomographic image of Pn velocity of the study area. Red tones represent low Pn velocity zones (unstable to partially molten mantle lid regions), while blue tones represent high Pn velocity (indicate stable mantle lid regions). A broad scale low (< 8 km/s) Pn velocity anomaly underlies northwestern Iran, the Caucasus region, Turkey, and northwestern Arabia, while smaller scale very low (< 7.8 km/s) Pn velocity anomalies underlie the Lesser Caucasus, western Greater Caucasus, and the easternmost portion of the NAF. High Pn velocity (> 8 km/s) zones underlie northern and northeastern Arabia, the Caspian and Azerbaijan (eastern Greater Caucasus), the Black Sea, and northeastern Mediterranean Sea. 1= Neaogene/Quaternary volcanoes, 2= Thrust boundary, and 3= Strike-slip boundary. **(b)** Checkerboard test results for $2^{o}$x$2^{o}$ cells inverted using the same station and event distribution used in the velocity and anisotropy model shown in Figure 3.2a. Most of the study area shows resolved checkerboard cells except for the northwestern Iran and the southern Caspian Sea where partial NW-SE smearing is observed to influence inverted Pn velocity and anisotropy directions.

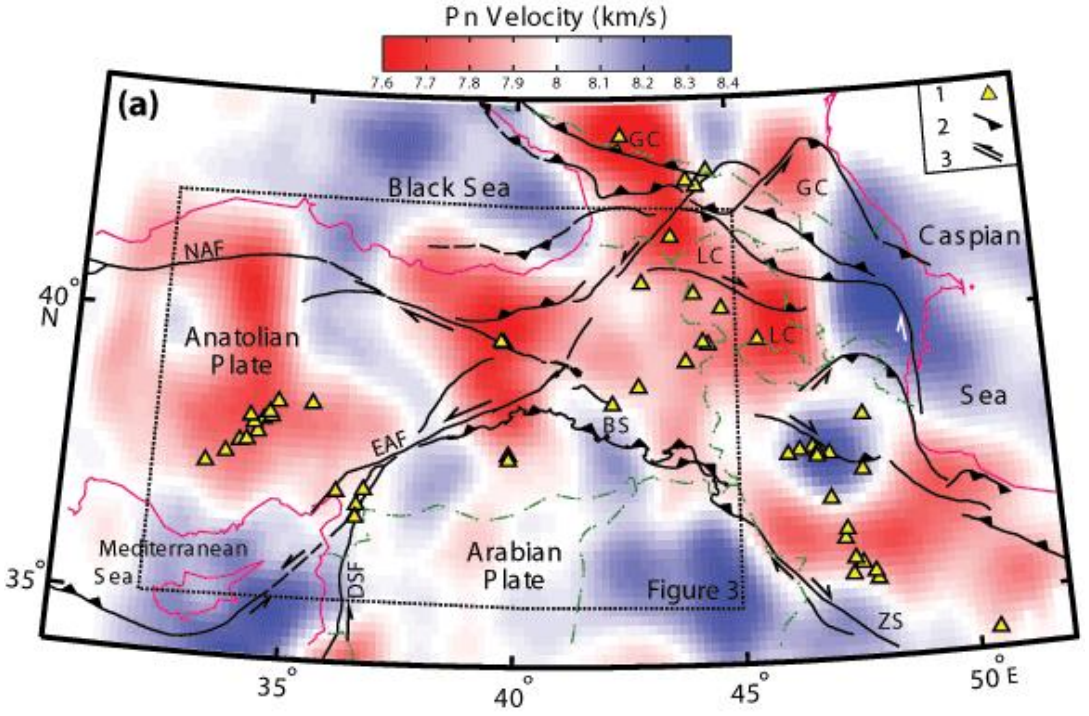
Pn Velocity (km/s)
7.6 7.7 7.8 7.9 8 8.1 8.2 8.3 8.4
(a)
1
2
3
Black Sea
GC
GC
Caspian
NAF
LC
LC
Anatolian
Plate
Sea
BS
EAF
Mediterranean
Sea
DSF
Arabian
Plate
Figure 3
ZS
40° N
35°
35°
40°
45°
50° E

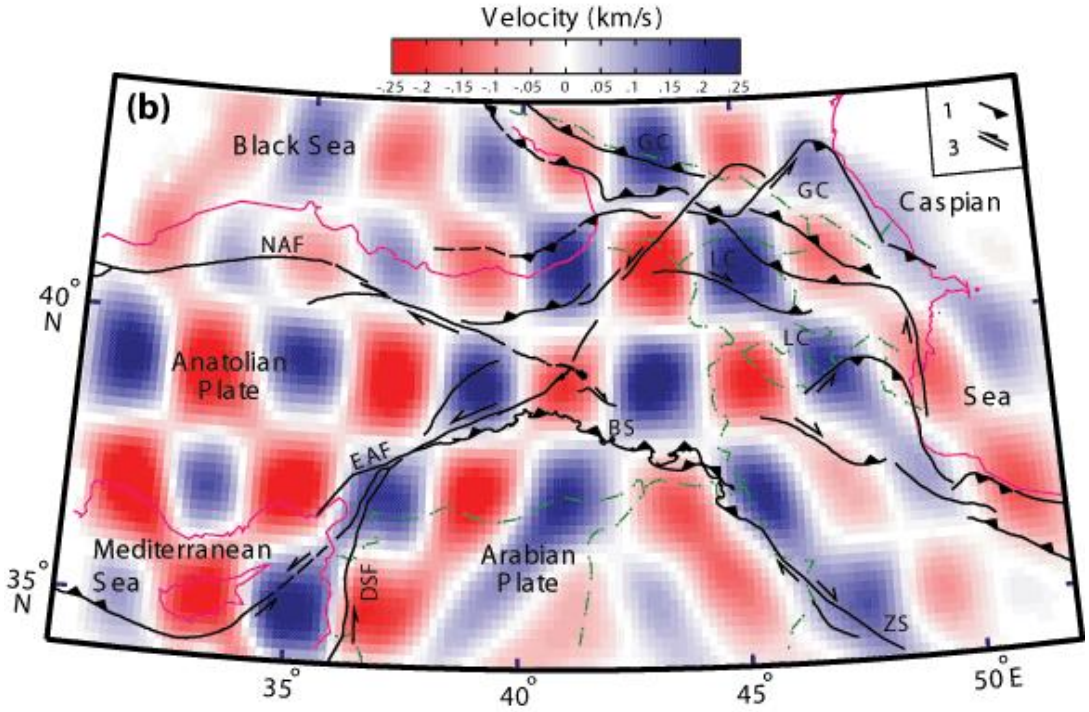
Velocity (km/s)
-.25 -.2 -.15 -.1 -.05 0 .05 .1 .15 .2 .25
(b)
1
3
Black Sea
GC
GC
Caspian
NAF
LC
LC
Anatolian
Plate
Sea
BS
EAF
Mediterranean
Sea
DSF
Arabian
Plate
ZS
40° N
35° N
35°
40°
45°
50° E

the synthetic travel times obtained from the checkerboard model. We used the same earthquake and station distribution as in the observed data and inverted the synthetic travel time anomalies using the same inversion parameters used (Figure 3.2b). The checkerboard anomalies in most of the study area are well resolved except for moderate smearing observed in northwestern Iran, the Caspian Sea, the Black Sea, and southern parts of northern Arabia (Figure 3.2b). In these regions smearing is more severe in the anisotropy resolution indicating that anisotropy orientations in these regions are not reliable.

The event and station distributions in the study area are not uniform. While the ETSE and Syrian National Seismic Network (SNSN) stations provide very dense coverage in a small region, additional stations cover other parts of the region sparsely. In order to take advantage of the high density station coverage of the ETSE and SNSN and to obtain a higher resolution Pn image along the collision zone we conducted a special, focused study by only using data from the ETSE and SNSN. All phase picks for these stations came from digital data and read by the authors. This data set is clearly higher quality than the global phase database in this region. Using this higher quality subset of our data set we obtained a detailed Pn velocity image at this segment of the collision zone (Figure 3.3a). We used the earlier model cell size ($1/6^{o}$) and used a smaller damping value (100 rather than 1000) on this data set since the noise in this subset of data set is much lower. This resulted in a clearly defined northernmost boundary of the Arabian plate along the EAF and the BS zones (Figure 3.3a). Figure 3.3b shows checkerboard test results obtained for this subset of data. In this case we used $1.5^{o}$x$1.5^{o}$ sized checkerboard anomalies. The synthetic results show that the resolution is high along the BS and the EAF zones (the area of interest) and at the junction of the North and East Antolian Fault zones.

**Figure 3.3. (a)** A map showing our tomographic image of Pn velocity using only the data picked and read by the authors. The upper bounds of high Pn velocity zone along the EAF and the eastern BS are used to define the northern extent of the Arabian plate boundary. **(b)** A map showing $1.5^{o}$x$1.5^{o}$ checkerboard test results inverted using the same stations and events distribution for Figure 3a. The best resolution is along the EAF, eastern BS zones, and at the intersection zone between the EAF and NAF zones. Symbols are as in Figure 3.2.

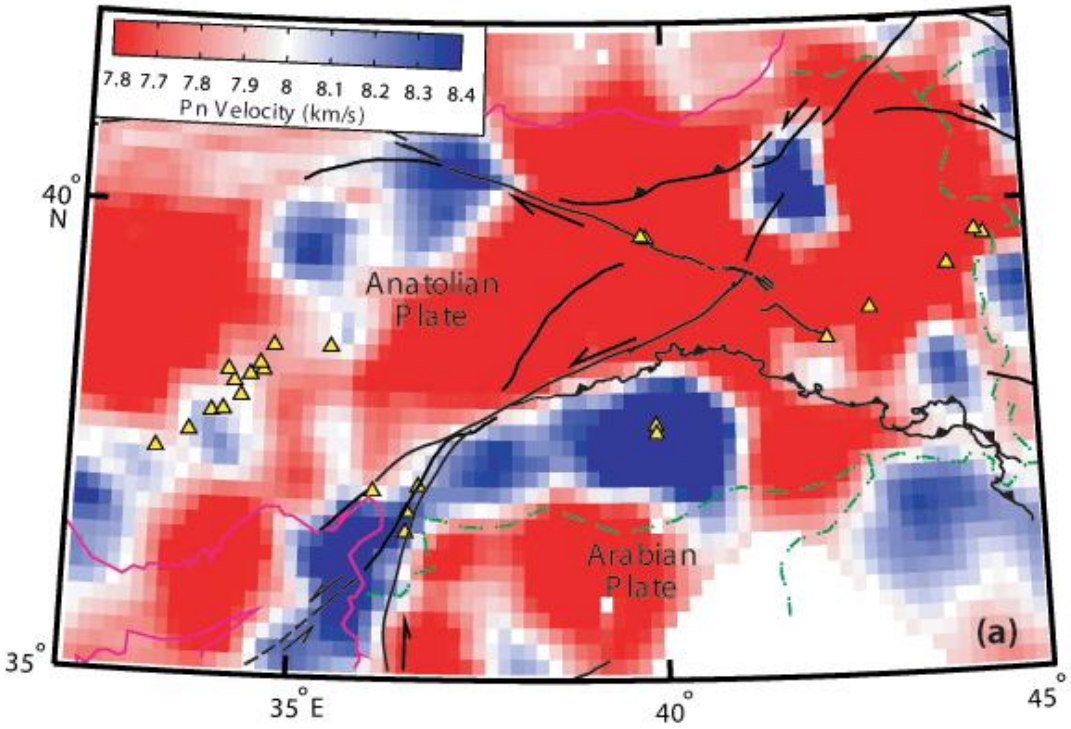
7.8 7.7 7.8 7.9 8 8.1 8.2 8.3 8.4
Pn Velocity (km/s)
40° N
Anatolian Plate
Arabian Plate
(a)
35°
35° E
40°
45°

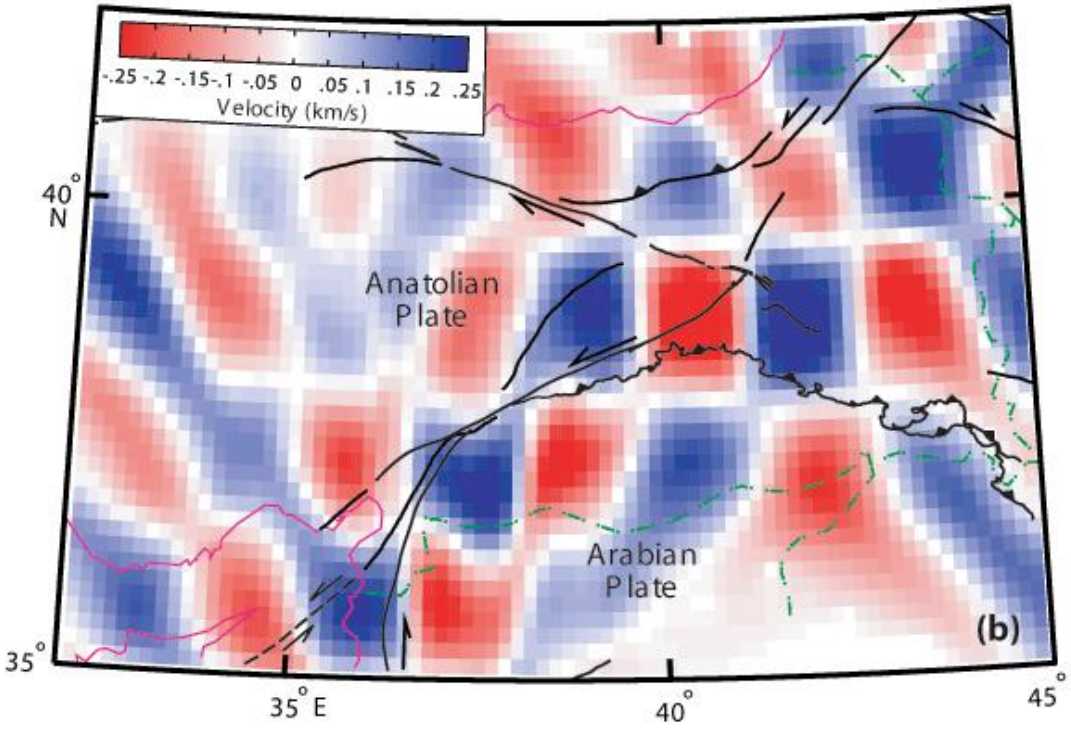
-.25 -.2 -.15 -.1 -.05 0 .05 .1 .15 .2 .25
Velocity (km/s)
40° N
Anatolian Plate
Arabian Plate
(b)
35°
35° E
40°
45°

Observed anisotropy orientations simultaneously inverted with Pn velocity show a higher degree of lateral variability compared to Pn velocity (Figure 3.4). Anisotropy orientations within the Anatolian plate and along the NAF vary from predominantly E-W in the center to more N-S in the western parts of Turkey (Figure 3.4). Zones of NE-SW anisotropy orientations surround the easternmost portion of the NAF zone, and along the Lesser Caucasus region. The latter two NE-SW anisotropy orientations spatially correlate with zones of very low Pn velocities, and show anisotropy magnitudes that are larger than their surroundings (Figure 3.4). In addition to upper mantle velocity and anisotropy values, station delays simultaneously inverted with Pn velocity and anisotropy are used to identify potential crustal velocity and thickness variations from the preliminary model (velocity 6.2 km/s and thickness 35 km). A station delay of 1 second corresponds to ~10 km difference in crustal thickness or 0.7 km/s crustal velocity change from the assumed model. Observed station delays vary from -2 to 2 seconds, these delays could not be explained independently by velocity or thickness variation only, but in most cases are explained by a combination of velocity and thickness variations as well as possible location and picking errors in the data set (Figure 3.5). We observed clusters of systematic positive or negative station delays in parts of the study area (Figure 3.5). The central stations of the western leg of the ETSE array show minor station delays (<0.5 s) and their values decrease towards the northwest (Figure 3.5). The eastern leg of the ETSE array, however, shows relatively uniform ~1 second station delays. A cluster of negative station delays occupies the Lesser Caucasus and western Greater Caucasus region (Figure 3.5). This cluster of negative station delays corresponds with the very low Pn velocity beneath the Lesser and western Greater Caucasus.

**Figure 3.4**. A map showing Pn anisotropy inverted simultaneously with the velocity model. See Figure 3.2a for text abbreviation in map.

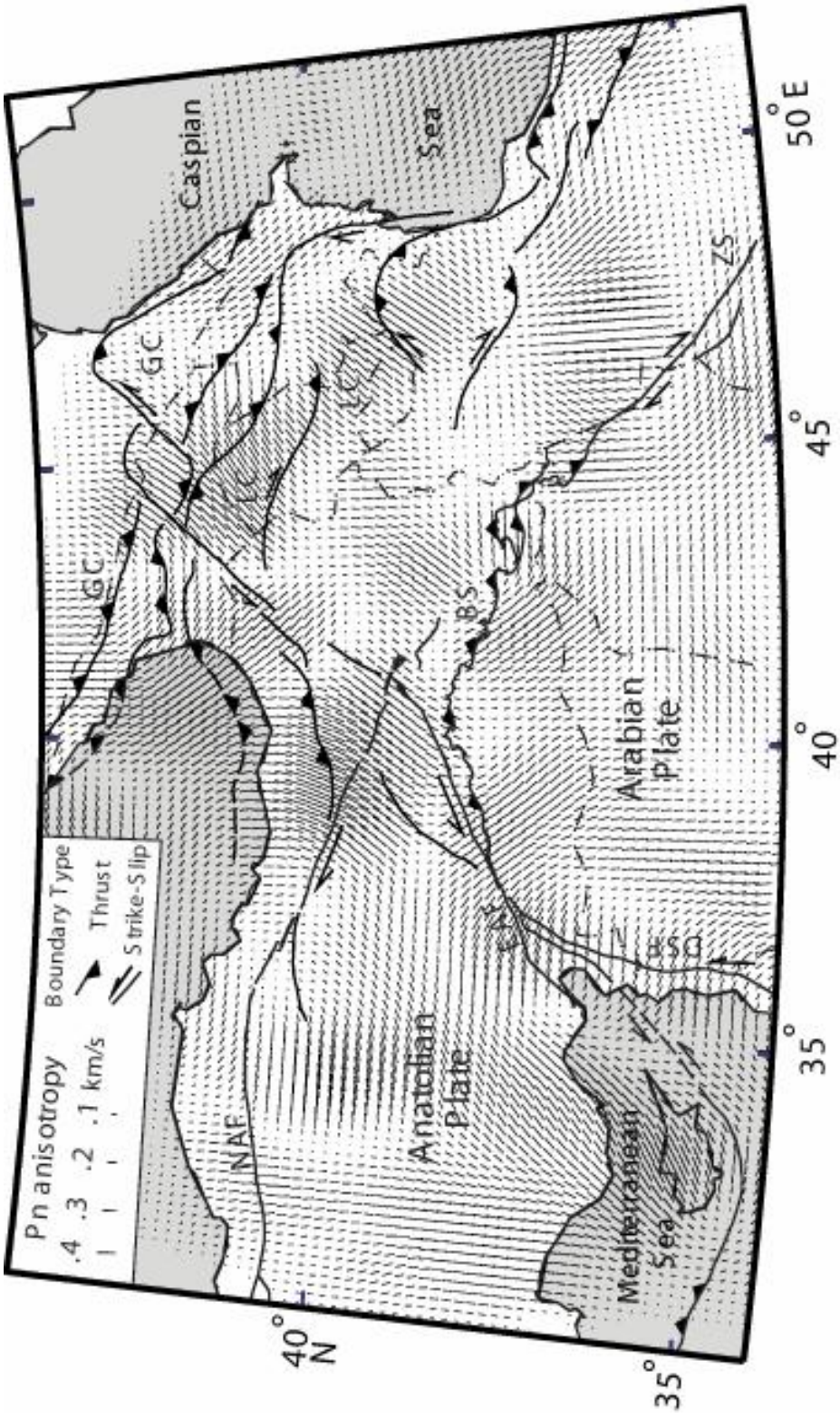
Pn anisotropy
.4 .3 .2 .1 km/s
Boundary Type
Thrust
Strike-Slip
Caspian
Sea
GC
GC
BS
ZS
NAF
Anatolian
Plate
Arabian
Plate
Mediterranean
Sea
BSO
40°
N
35°
35°
40°
45°
50° E

**Figure 3.5**. A map of station delays representing the station leg residuals relative to the assumed velocity model. Squares are positive station delays and indicate thick and/or slow crust. Circles are negative station delays and indicate fast and/or thin crust relative to the assumed velocity and thickness model of the crust. For abbreviated text, see Figure 3.1. Eastern Turkey Seismic Experiment (ETSE) array shows a general decrease in delay magnitudes from east to west. Stations located in the Caucasus region show negative station delays.

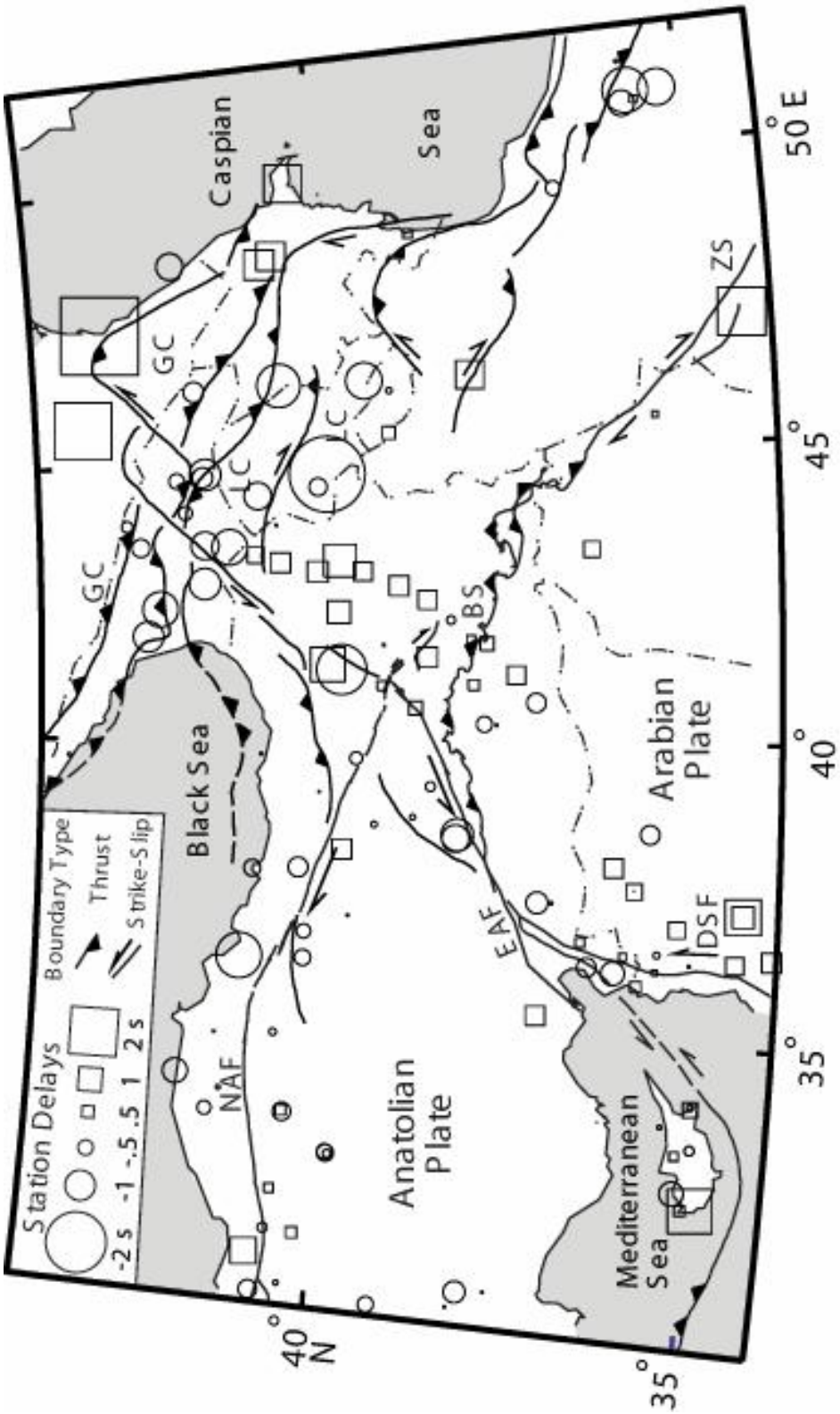
Caspian
Sea
GC
GC
GC
ZS
BS
Black Sea
NAF
EAF
DSF
Anatolian
Plate
Arabian
Plate
Mediterranean
Sea
Station Delays
-2 s -1 -.5 .5 1 2 s
Boundary Type
Thrust
Strike-Slip
40°
N
35°
35°
40°
45°
50 E

## DISCUSSION AND CONCLUSIONS

The geodynamic model governing the accommodation of the Arabian plate's northward motion has been the subject of an ongoing debate (McKenzie, 1972; Rotstein and Kafka, 1982; Dewey et al., 1986). In this study, we presented evidence on the state of the lithospheric mantle beneath this young continent-continent collision zone. Geologic data from eastern Anatolia and the Caucasus indicate that the latest stage of collision related volcanism started in the Late Miocene and continued until historical times (Yilmaz, 1990; Keskin et al., 1998). Upper mantle instability in this region is also evidenced by young calc-alkaline and alkaline volcanism (Figure 3.2a) (Innocenti et al., 1976; Pearce et al., 1990). At the present time, we observe a broad scale low and smaller scale very low Pn velocity anomalies beneath northwestern Iran, Eastern Anatolian plateau, the Caucasus region, and most of the Anatolian plate (Figure 3.2a). Comparably, Sn wave propagation anomalies in this region also show high attenuation beneath the Anatolian plate, the Anatolian plateau, and the Caucasus region (Gok et al., 2000; Sandvol et al., 2001). These results are also consistent with mantle lid instability interpretation beneath the Eurasian side of the collision (i.e., northwestern Iran, eastern Anatolia, the Caucasus, and Anatolia plate). We interpret that partially molten to eroded mantle lid exists in regions underlain by very low Pn velocity anomalies, such as the easternmost portion of the NAF, and the Lesser and western Greater Caucasus regions (Figure 3.2a). The very low Pn velocity may even be interpreted to indicate the complete absence of mantle lid in these regions, and that asthenospheric material is directly located beneath the crust. This interpretation rules out the earlier proposed idea of mantle thickening of the lithosphere (Dewey et al., 1986) beneath the Anatolian plateau and the Caucasus region. If there were ever a lithospheric thickening in these regions, either delamination or convective removal of the thickened mantle lithosphere might have eliminated the thick lithosphere.

Our results also invalidate the idea of Arabian plate subduction or underthrusting beneath the eastern Anatolian plateau as suggested by Rotstein and Kafka (1982). Stable mantle lid regions as identified by high Pn velocities underlie only the northernmost portion of the Arabian plate. This stable region sharply stops along the Bitlis suture zone (Figure 3.2a). Using a higher resolution subset of data we show that the northern bounds of Arabia's stable mantle lid velocities follow the western BS and the EAF lines relatively well (Figure 3.3a).

In continental settings anisotropy orientations are commonly described to mimic regional tectonic trends (e.g., Kendall, 2000). Compared to Pn velocity, mantle lid Pn anisotropy shows relatively more variations within a single plate (e.g., Anatolian plate) or along a single tectonic boundary (e.g., NAF). Observed Pn anisotropy orientations do not seem to follow the tectonic trends. The more sudden anisotropy variations in eastern Turkey and the Caucasus region may possibly reflect more complex deformation processes in this region.

**ACKNOWLEDGMENTS**

The authors are grateful for the help and assistance of our colleagues E. Zor, R. Gok, T. Bekler, R. Kay, S. Kuleli, K. Al-Damegh, C. Brindisi, and F. Gomez. We are thankful for the help of the federal and local governments of Turkey. This research is supported by the National Science Foundation (Grant No. EAR-9804780) and Bogazici University Research Fund (Grant No. 99T206).

## REFERENCES

Bozkurt, E. 2001. Neotectonics of Turkey - a synthesis. Geodinamica Acta : The Europian Journal of Geodynamics, v. 14, no. 1-3, p. 3-30.

Dewey, J.F., M.R. Hempton, W.S.F. Kidd, F. Saroglu and A.M.C. Sengor 1986. Shortening of continental lithosphere: the neotectonics of Eastern Anatolia - a young collision zone. In M.P. Coward and A.C. Ries (Eds.), Collision Tectonics, Geological Society Special Publication, No. 19, p. 3-36.

Gok, R., N. Turkelli, E. Sandvol, D. Seber and M. barazangi 2000. Regional wave propagation in Turkey and surrounding regions. Geophysical Research Letters, v. 27, no. 3, p. 429-432.

Hearn, T.M. 1996. Anisotropic Pn tomography in the western United States. Journal of Geophysical Research, v. 101, no. B4, p. 8403-8414.

Hearn, T.M. and J.F. Ni 1994. Pn velocities beneath continental collision zones: the Turkish-Iranian Plateau. Geophysical Journal International, v. 117, p. 273-283.

Hempton, M.R. 1987. Constraints on Arabian plate motion and extensional history of the Red Sea. Tectonics, v. 6, no. 5, p. 687-705.

Innocenti, P., R. Mazzuoli, G. Pasquare, F.R.D. Brozolo and L. Villare 1976. Evolution of the volcanism in the area of interaction between Arabian, Anatolian and Iranian plates (Lake Van, eastern Turkey). J. Volcan. Geotherm. Res, v. 1, p. 103-112.

Kendall, J.-M. 2000. Seismic anisotropy in the boundary layers of the mantle. In S.-i. Karato, A.M. Forte, R.C. Liebermann, G. Masters and L. Stixrude (Eds.), Deep Earth Interior: Mineral physics and tomography from the atomic to the global scale, American Geophysical Union, Geophysical Monograph 117, p. 115-159.

Keskin, M., J.A. Pearce and J.G. Mitchell 1998. Volcano-stratigraphy and geochemistry of collision-related volcanism on the Erzurum-Kars Plateau, northeastern Turkey. Journal of Volcanology and Geothermal Research, v. 85, p. 355-404.

McKenzie, D. 1972. Active tectonics of the Mediterranean region. Geophysical Journal of the Royal Astronomical Society, v. 30, p. 109-185.

Paige, C.C. and M.A. Saunders 1982. LSQR: Sparse linear equations and least squares problem. ACM Transactions on Mathematical Software, v. 8, no. 2, p. 195-209.

Pearce, J.A., J.F. Bender, S.E. Delong, W.S.F. Kidd, P.J. Low, Y. Guner, F. Saroglee, Y. Yilmaz, S. Moorboath and J.G. Mitchell 1990. Gensis of collisional volcanism in eastern Anatolia, Turkey. J. Volc. geotherm. Res., v. 44, p. 189-229.

Philip, H., A. Avagyan, A. Karakhanian, J.-F. Ritz and S. Rebai 2001. Estimating slip rates and recurrence intervals for strong earthquake along an intracontinental fault: example of the Pambak-Sevan-Sunik fault (Armenia). Tectonophysics, v. 343, p. 205-232.

Reilinger, R.E., S.C. McClusky, M.B. Oral, R.W. King, M.N. Toksoz, A.A. Barka, I. Kinik, O. Lenk and I. Sanli 1997. Global Positioning System measurements of present-day crustal movements in the Arabia-Africa-Eurasia plate collision zone. Journal of Geophysical Research, v. 102, no. B5, p. 9983-9999.

Rotstein, Y. and A.L. Kafka 1982. Seismotectonics of the southern boundary of Anatolia, eastern Mediterranean region; subduction, collision, and arc jumping. Journal of Geophysical Research, v. 87, no. 9, p. 7694-7706.

Sandvol, E., K. Al-Damegh, A. Calvert, D. Seber, M. Barazangi, R. Mohamad, R. Gok, N. Turkelli and C. Gurbuz 2001. Tomographic imaging of Lg and Sn propagation in the Middle East. Pure and Applied Geophysics, v. 158, p. 1121-1163.

Sengor, A.M.C., N. Gorur and F. Sargolu 1985. Strike-slip faulting and related basin formation in zones of tectonic escape: Turkey as a case study. In K.T. Biddle and N. Christie-Blick (Eds.), Strike-slip faulting and basin formation, Society of Econ. Paleontol. Mineral. Special Publication, 37, p. 227-264.

Sengor, A.M.C. and Y. Yilmaz 1981. Tethyan evolution of Turkey: a plate tectonic approach. Tectonophysics, v. 75, p. 181-241.

Yilmaz, Y. 1990. Comparison of young volcanic associations of western and eastern Anatolia formed under a compressional regime: a review. Journal of Volcanology and Geothermal Research, v. 44, p. 69-87.

Yilmaz, Y. 1993. New evidence and model on the evolution of the southeast Anatolian orogen. Geological Society of America Bulletin, v. 105, no. 2, p. 251-271.

# CHAPTER FOUR

## Pn tomographic imaging of mantle lid velocity and anisotropy at the junction of the Arabian, Eurasian, and African plates*


### ABSTRACT

The Arabian plate's interaction with the Eurasian plate has played a major role in building the young mountain belts along the Zagros-Bitlis continent-continent collision zone. Arabia's northward motion is considered to be the primary driving force behind the present-day westerly escape of the Anatolian plate along the North and East Anatolian fault zones as well as the formation of the Turkish and the Iranian plateaus. In this study we mapped Pn wave velocity and anisotropy structures at the junction of the Arabian, Eurasian, and African plates in order to elucidate the upper mantle dynamics in this region. Pn is a wave that propagates within the mantle lid of the lithosphere and is often used to infer the rheology and fabric of the mantle lithosphere. Using a strict selection criterion we used arrival times of 166,000 Pn phases to invert for velocity and anisotropy in the region. Using a least squares tomographic code, these data were analyzed to simultaneously solve for both velocity and azimuthal anisotropy in the mantle lithosphere. We found that most of the continental regions in our study area are underlain by low Pn velocity structures. Broad scale (~500 km) zones of low (< 8 km/s) Pn velocity anomalies underlie the Anatolian plate, the Anatolian plateau, the Caucasus region, northwestern Iran, and northwestern Arabia and smaller scale (~200 km), very low (< 7.8 km/s) Pn velocity


---

*Submitted to Geophysical Journal International on October 14, 2002 as "Pn tomographic imaging of mantle lid velocity and anisotropy at the junction of the Arabian, Eurasian, and African plates" by Ali I. Al-Lazki, Eric Sandvol, Dogan Seber, Muawia Barazangi, Niyazi Turkelli, and Randa Mohamad.

zones underlie southern Syria, the Lesser Caucasus, the Isparta Angle, central Turkey, and the northern Aegean Sea. The broad scale low velocity regions are interpreted to be hot and unstable mantle lid zones, whereas very low Pn velocity zones are interpreted to be regions of no mantle lid. The low and very low Pn velocity zones in eastern Turkey, northwestern Iran, and the Caucasus region may be associated with the latest stage of intense volcanism that has been active since the Late Miocene. The low Pn velocity zones beneath the Anatolian plate, eastern Turkey, and northwestern Iran may in part be a result of the subducted Tethyan oceanic lithosphere beneath Eurasia. We also found a major low velocity zone beneath northwestern Arabia and the Dead Sea fault system. We interpret this anomaly to be a possible extension of the hot and anomalous upper mantle of the Red Sea and East Africa rift system. High Pn velocities (8.1 - 8.4 km/s) are observed to underlie the Mediterranean Sea, the Black Sea, the Caspian Sea, and central and the eastern Arabian plate. Observed Pn anisotropy showed a higher degree of lateral variations in comparison to the Pn velocity structure. Though the Pn anisotropy varies even in a given tectonic region, in eastern Anatolia very low Pn velocity and Pn anisotropy structures appear to be coherent.

## INTRODUCTION

The study area is located at the junction of the Arabian, Eurasian, and African plates. This region encompasses diverse active plate boundaries and relatively modest active intraplate deformation. Present-day boundaries of the Arabian plate are of several types (Figure 4.1). In the southwest, a divergent plate boundary (Red Sea) exemplifies early stages of continental rifting and sea floor spreading. In the northwest, the Dead Sea Fault (DSF) transform system separates the Arabian plate from the Sinai and Levantine subplates (Figure 4.1). In the north and northeast the boundary zone is a

**Figure 4.1.** Simplified tectonic map of the study area showing main plate boundaries. AP: Anatolian Plate, BS: Bitlis Suture, CA: Cyprean Arc, CIM: Central Iranian Microplate, DSF: Dead Sea Fault, EAF: East Anatolian Fault, GC: Greater Caucasus, HA: Hellenic Arc, IA: Isparta Angle, KD: Kopeh Dagh, LC: Lesser Caucasus, LB: Lut Block, SL: Sinai and Levantine subplate, NAF: North Anatolian Fault, NWIP: North West Iranian Plate, TC: Transcaucasus, and ZS: Zagros Suture.

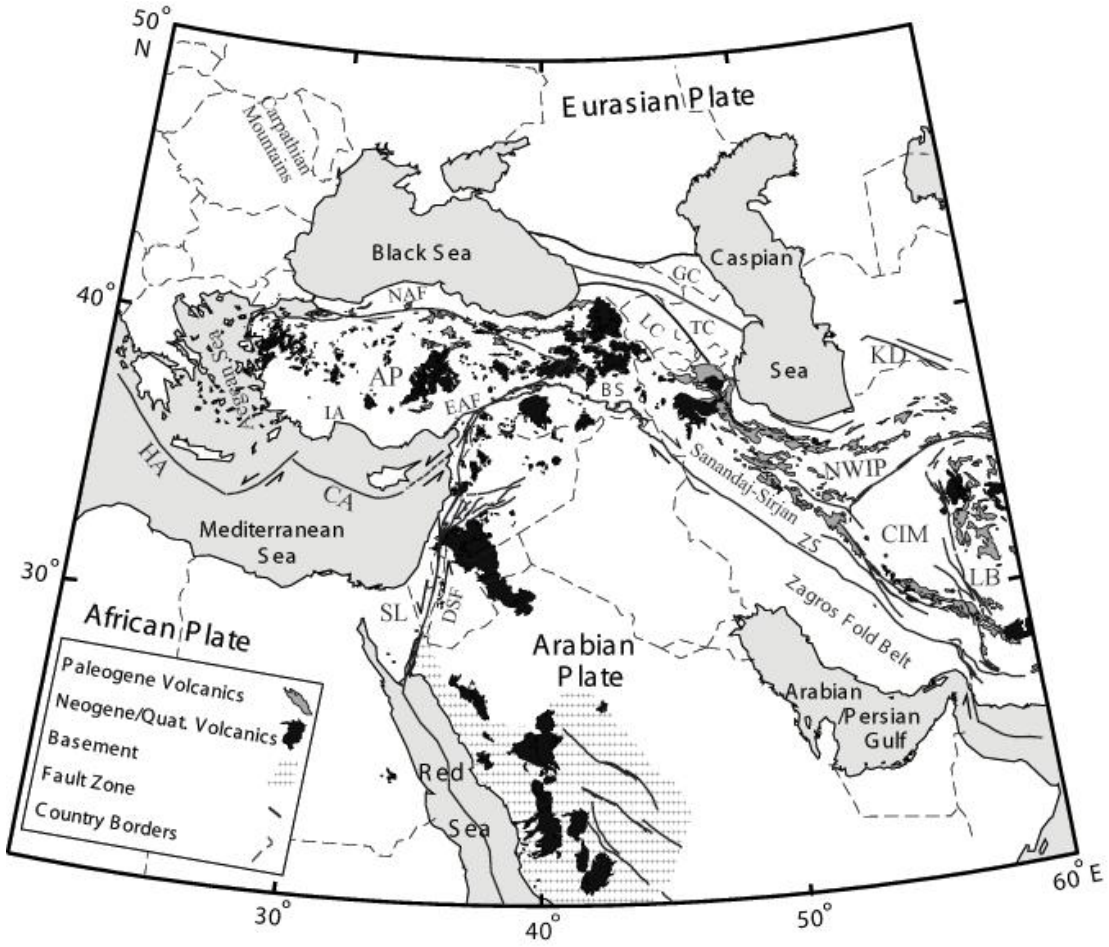
50° N
40°
30°
60° E
30°
40°
50°
Eurasian Plate
Carpathian Mountains
Black Sea
Caspian Sea
Caspian
GC
NAF
LC
TC
KD
AP
IA
EAF
BS
HA
CA
Mediterranean Sea
Sanandaj-Sirjan ZS
NWIP
CIM
LB
Zagros Fold Belt
SL
DSF
African Plate
Arabian Plate
Arabian/Persian Gulf
Red Sea
Paleogene Volcanics
Neogene/Quat. Volcanics
Basement
Fault Zone
Country Borders

continent-continent collision, where the Arabian plate is colliding with the Eurasian plate along the Bitlis Suture (BS) and the Zagros Suture (ZS) zones (Figure 4.1). Northward motion of Arabia is partially accommodated by the westerly extruding Anatolian plate along the North Anatolian Fault (NAF) and the East Anatolian Fault (EAF) zones (McKenzie, 1972; Sengor and Yilmaz, 1981; Sengor et al., 1985). The escaping Anatolian plate is bounded in the west and south by the subduction zones of the Hellenic and Cyprean arcs, respectively.

In this paper we use the Pn phase to study the mantle lid velocity and infer the state of the lithosphere at the junction of the Arabian, Eurasian, and African plates. Pn phase is a guided high-frequency compressional wave that propagates within a high velocity mantle lid which acts like a wave-guide bounded by the low velocity zone (LVZ) below and the crust above (e.g., Menke and Richards, 1980; Beghoul et al., 1993). Pn wave velocity is often used to infer uppermost mantle rheology. Variations in Pn velocities are caused by changes in the physical parameters of uppermost mantle rocks. Changes in temperature and composition, as well as presence of water and volatiles are the main causes of velocity changes. Pn velocities are generally the highest in oceanic lithosphere and could reach up to 8.4 km/s (Walker, 1977). Continental lithosphere Pn velocities, however, vary significantly depending on the rheology of the mantle lid. Higher Pn velocities (> 8 km/s) imply a tectonically stable mantle lid, while very low Pn velocities (< 7.8 km/s) are usually an indication of partial melt (Hearn, 1999; Calvert et al., 2000).

Pn velocities also show azimuthal variations. Seismic anisotropy has been observed in the upper mantle in both oceanic (Backus, 1965) and continental settings (Beghoul and Barazangi, 1990). Earlier studies have concluded that most of the anisotropy occurs in the upper mantle, whereas between 600 km depth and the D" discontinuity the mantle appears to be relatively isotropic (e.g., Savage, 1999;

Kendall, 2000). Studies of Rayleigh and Love surface waves (e.g., Anderson, 1961), shear wave splitting of phases like SKS (e.g., Silver and Chan, 1988), and Pn phase (e.g., Hearn, 1996; Smith and Ekstrom, 1999) have provided abundant evidence for the presence of upper mantle seismic anisotropy. The major cause of seismic anisotropy in the upper mantle is lattice preferred orientation caused by plastic deformation (e.g., Mainprice and Nicolas, 1989; Karato, 1998). It is well established that the strength of lattice preferred orientation (LPO) is a function of finite strain and hence seismic anisotropy should evolve with deformation history (Savage, 1999; Mainprice et al., 2000). In continental settings, the length and scale over which anisotropy varies mimic regional trends at the surface (e.g., Smith and Ekstrom, 1999; Kendall, 2000), suggesting coupling between the mantle and crust during orogenic deformation. In contrast, the upper mantle anisotropy in oceanic settings appears to reflect larger scale patterns, such as plate spreading direction (Kendall, 2000).

A previous study in the same region by Hearn and Ni (1994) used 70,755 Pn phases to invert for Pn velocities without anisotropy consideration. Their study had good ray coverage within the Aegean region, but in the regions south of the Caspian Sea and within the Arabian plate only sparse data were available. A similar upper mantle study by Hearn (1999) on the uppermost mantle Pn velocity and anisotropy of the European region covered only parts of the Aegean Sea. In this study we use a similar technique to that of Hearn (1999) and tomographically invert for Pn velocity and anisotropy in the region. This study uses significantly larger number of seismic stations and events especially in the Arabian-Eurasian collision zone. The use of the temporary 29-station broadband network of the Eastern Turkey Seismic Experiment and the 20-station short period seismic network in Syria provide critical and high resolution data that are crucial in understanding the complex tectonics of this region.

## TECTONIC BACKGROUND

Along the northern and northeastern boundary of Arabia the opening of the Neo-Tethys ocean began in the Late Permian and continued until the Late Cretaceous times. Consumption of the Neo-Tethys oceanic lithosphere by subduction began in Early Cretaceous along the eastern and northeastern boundaries of the Arabian-African plate. The timing of collision between Arabia and Eurasia along the Bitlis and the Zagros sutures is still being debated, with proposed ages ranging from Late Cretaceous (Takin, 1972) to Pliocene (Dewey et al., 1973). Hempton (1982, 1985) proposed an initial suturing to have begun in Middle to Late Eocene.

Along the present-day southwestern boundary of the Arabian plate, the opening of the Red Sea and the Gulf of Aden is thought to have occurred in two extensional episodes, one in the Middle-Late Eocene period and the other occurred in the Early Pliocene (e.g., Hempton, 1987). This separation of Arabia from Africa is accommodated by the left lateral DSF system and is also considered to be responsible for the reorganization of relative plate motions in the Anatolian plateau (Bozkurt, 2001). In the Early Pliocene, continued N-S convergence between Arabia and Eurasia resulted in the extrusion of the Anatolian plate along the North Anatolian Fault (NAF) and the East Anatolian Fault (EAF) zones (e.g., Sengor and Yilmaz, 1981; Sengor et al., 1985). The two fault systems separate an eastern domain experiencing mainly N-S compression from the westerly escaping Anatolian plate. The tectonic domains east of NAF and EAF are comprised of several sub-domains from north to south: Greater Caucasus, Transcaucasus depression, Lesser Caucasus, the east Anatolian plateau, and the Arabian platform (Kocyigit and Erol, 2001).

Extension behind the Aegean subduction system began in the middle to late Miocene (13-10 Ma) (Le Pichon and Angelier, 1979; Jackson, 1994) or possibly as recent as 6 Ma (Mckenzie, 1978). Extension of up to 100% is thought to have affected

the Aegean region in an N-S direction (Mckenzie, 1978), with the greatest extensional strains located in the southern Aegean, north of Crete (Angelier et al., 1982; Jackson, 1994). Present-day extension occurring on the northern Aegean extending to ~31$^{o}$ E within the Anatolian plate (Angelier et al., 1982) is believed to be associated with the retreating subduction of the African oceanic lithosphere (eastern Mediterranean) beneath the Hellenic arc. This extension dies out in the area north of ~42$^{o}$ N in Bulgaria and northern Greece (Figure 4.1).

**METHOD**

P-wave travel time residuals from sources at 1.8$^{o}$ to 16$^{o}$ distances were inverted to obtain the uppermost mantle velocity model for the region. A tomography method based on observed travel time residuals developed by (Hearn, 1996) is used to invert for Pn wave velocity, anisotropy, as well as event and station delays. The method uses Pn travel time model paths between event-station pairs. This path includes three legs: an event leg, a mantle leg, and a station leg. The three segments of Pn travel time path are described by the following travel time equation (Hearn, 1996):

$$t_{ij} = a_i + b_j + \sum d_{ijk} (S_k + A_k \cos 2\Phi + B_k \sin 2\Phi ) \quad (4.1)$$

where $a_i$ is the station time leg for i station, $b_j$ is the event time leg for the j event, $d_{ijk}$ is the distance traveled between j event and i station for cell k, $\Phi$ is the back azimuth angle, $S_k$ is the slowness value for the k cell and $A_k$ and $B_k$ are anisotropy coefficients for the k cell (Hearn, 1996). Equation (4.1) is iteratively solved for all event-station pairs using LSQR algorithm that solves sparse linear equations and least squares problems (Paige and Saunders, 1982) to obtain slowness, anisotropy, and station and event delays (Hearn, 1996). This method then separates station and event leg travel

times based on the assumed crustal model. We assumed a 35 km thick crust with a 6.2 km/s average velocity and an upper mantle velocity of 8.0 km/s to calculate travel times for each station and event leg. In our inversion we used cell sizes of $0.25^{o}$x$0.25^{o}$ for the region, similar to previous studies.

Since travel-time data include a certain degree of noise and uneven ray coverage, a damping parameter is used to regularize the solution (Paige and Saunders, 1982) and reduce noise artifacts. In this case damping parameters for both velocity and anisotropy were used to control image smoothness and reduce artifacts in the model (Hearn, 1996). In our inversion process, after a series of tests, we chose a final damping value of 1000 for both velocity and anisotropy. This value was found to best remove erroneous data noise and best balance the contribution of both anisotropy and velocity on the inverted model. Damping values of less than 1000 were found to produce spurious velocity anomalies, while values lager than 1000 significantly reduced our model resolution.

**DATA**

In this study two categories of Pn phase data were used. The first are phase data picked by the authors from the Eastern Turkey Seismic Experiment (29 PASSCAL broadband stations), the Syrian National Seismic Network (20 short period stations), the southern Caspian broadband stations (5 stations), the Iranian Long Period Array (ILPA) (5 stations), and the Turkish National Network (5 short period stations) data (Figure 4.2a). The second category is phase data that were extracted from the International Seismological Centre (ISC) and the National Earthquake Information Center (NEIC) earthquake catalogs (Figures 4.2a and 4.2b). The second category of Pn phase data include 729,819 phases that were extracted from the ISC data catalogue and 95,716 phases from the NEIC data catalogue. A total of 7,414 Pn phase picks

**Figure 4.2a.** Map showing seismic stations used in this study. CA: southern Caspian Sea stations, ETSE: Eastern Turkey Seismic Experiment stations, ILPA: Iran Long Period Array, SN: Syrian National network, and TN: Turkish National network. Open triangles correspond to selected stations from the National Earthquake Information Center (NEIC) and the International Seismological Centre (ISC) catalogues. (See Figure 4.1 for geographic locations).

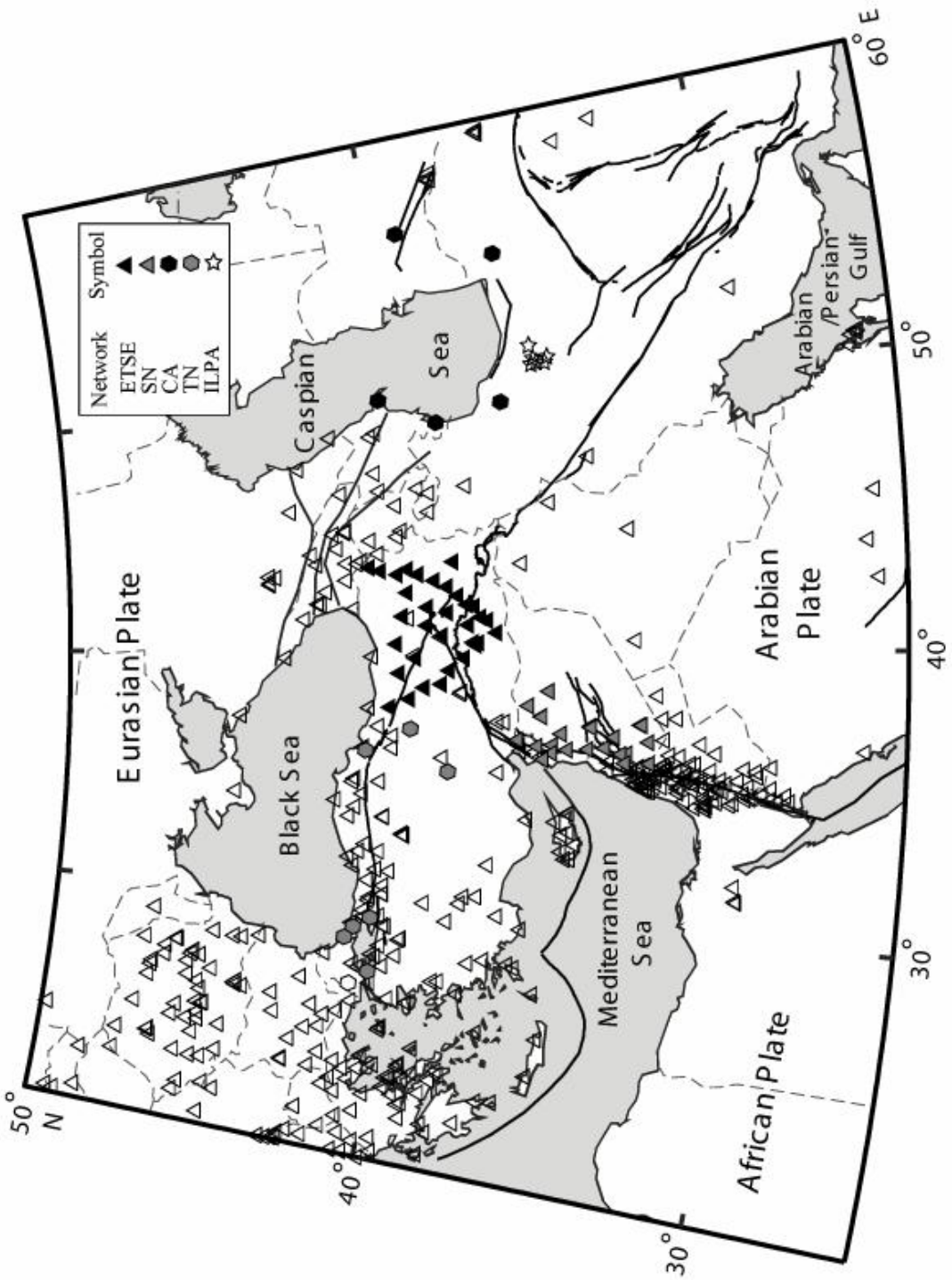
Network
Symbol
ETSE
SN
CA
TN
ILPA
Caspian Sea
Black Sea
Mediterranean Sea
Arabian Plate
Arabian /Persian Gulf
Eurasian Plate
African Plate
50° N
40°
30°
50°
60° E

**Figure 4.2b.** Map showing seismic events (in circles) used in the Pn velocity and anisotropy tomography inversion. (See Figure 4.1 for geographic locations).

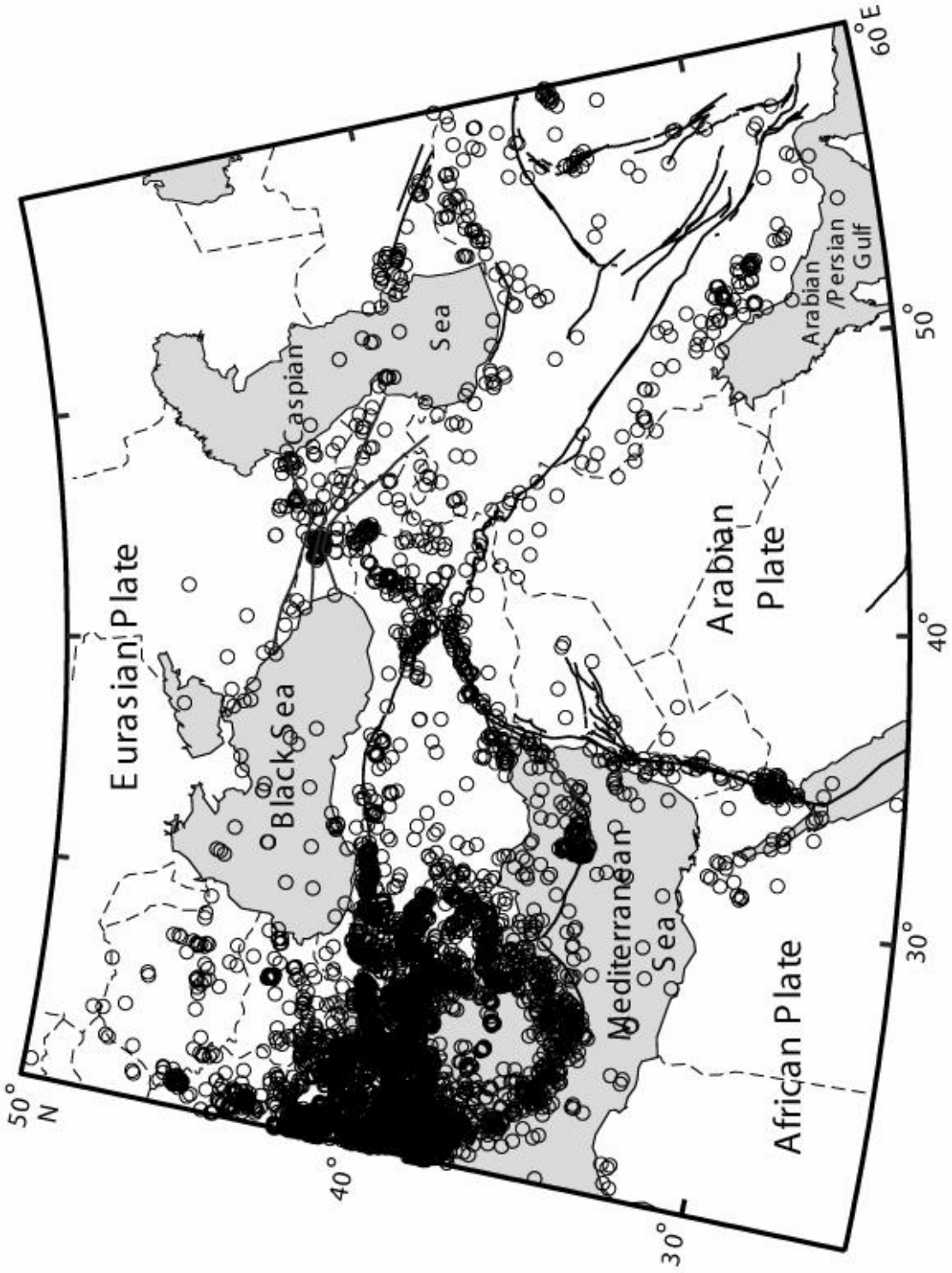
Eurasian Plate
Black Sea
Caspian Sea
Arabian Plate
Arabian /Persian Gulf
Mediterranean Sea
African Plate
50° N
40°
30°
30°
40°
50°
60° E

were read by the authors using the data from the ETSE, Syria network, ILPA, Caspian stations, and the Turkish network. In addition, ETSE stations (Figure 4.2a) were used to locate local seismicity in eastern Turkey. These local events amounted to a total of 2,715 phase picks, which provided a dense coverage within the 29-station array (Figures 4.2a and 4.2b).

Since the phase data might include many erroneous readings, especially those obtained from catalogues, a rigorous selection method was used. In assessing data quality and integrity we used 13 criteria to filter out possible erroneous phase data at three levels. We screened phase data for both large location errors, pick precision, and travel time errors. To minimize location errors, we used events only with location azimuthal gaps less than $150^{o}$, recorded by a minimum of 25 stations. We have experimented with a number of more strict criteria in our ISC and NEIC data and found that in regions where we maintained sufficient ray coverage and resolution our resulting model was not affected. For the data picked by the authors, in terms of picking precision we only used phases with estimated accuracy of one second or better. Out of 8,944 events (Figure 4.2b) and their associated stations a total of 166,000 phases were selected using a maximum of 10 second travel time residual (Figure 4.3a). Our tomographic inversion achieved a 35 % variance reduction from the initial linear fit (Figure 4.3b).

The station density used in the Pn velocity inversion is highly variable in the study area (Figure 4.4). High station density areas are located along the DSF system, eastern Turkey, in and around the Caucasus mountain belts, in and around the Aegean Sea and within the Bulgarian and Romania territories (Figure 4.2a). There is sparse station coverage in central and northeastern Arabia platform and east of $45^{o}$ E

meridian (Figure 4.2a). The highest event density occurred in the Aegean region and the lowest within the Arabian plate (Figure 4.2b). Path density for those

**Figure 4.3. (a)** Input travel time residuals (corrected for a 2-D velocity fit). A 10 seconds cutoff is used in the Pn tomography inversion. The travel time residuals are calculated using the study area's Pn average velocity (8 km/s). **(b)** Travel time residuals obtained using the Pn tomography results. A 35 % variance reduction is obtained compared to the input 2-D fit residuals. (See Figure 4.1 for geographic locations).

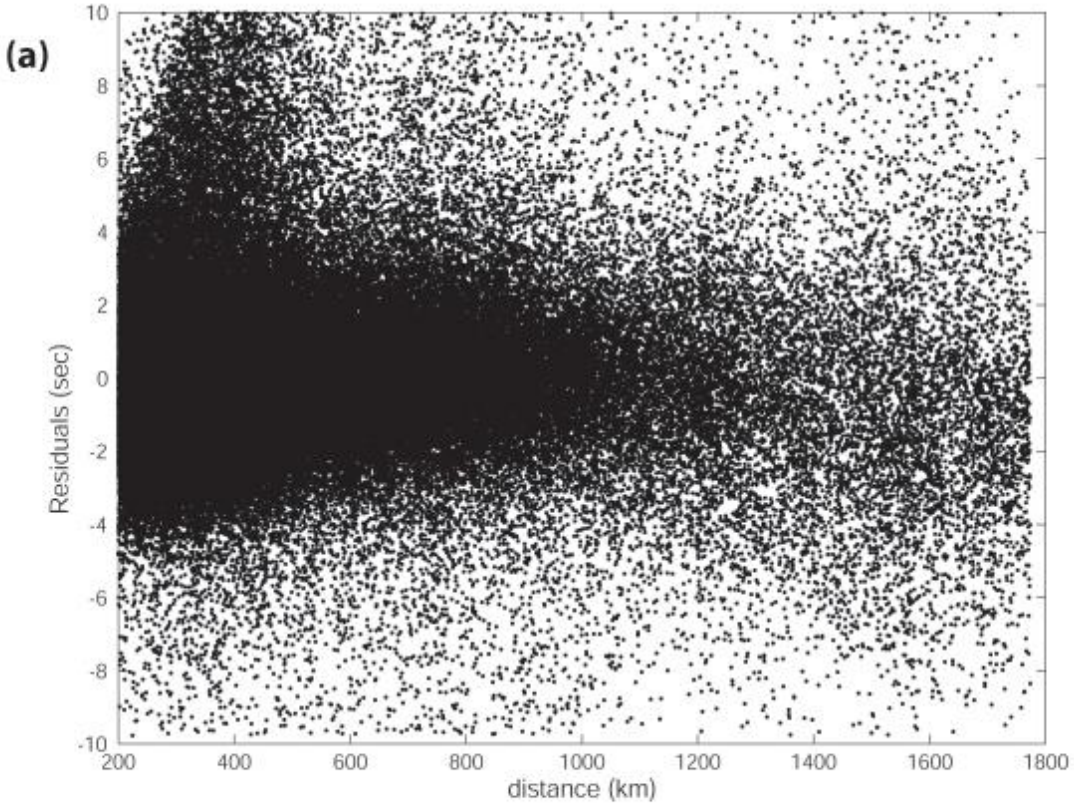
(a)
Residuals (sec)
distance (km)
10
8
6
4
2
0
-2
-4
-6
-8
-10
200
400
600
800
1000
1200
1400
1600
1800

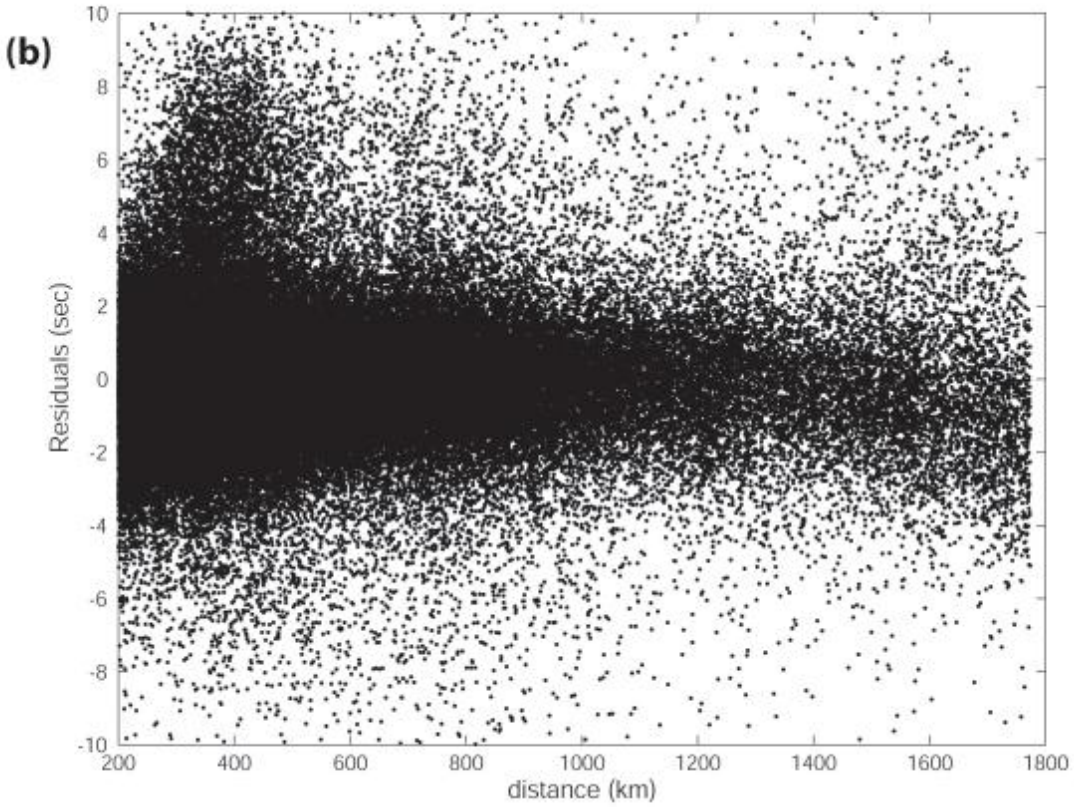
(b)
Residuals (sec)
distance (km)
10
8
6
4
2
0
-2
-4
-6
-8
-10
200
400
600
800
1000
1200
1400
1600
1800

**Figure 4.4.** Hit map coverage of the study area. Shades of gray show the number of rays passing through a single $0.25^{o}$x$0.25^{o}$ cell.

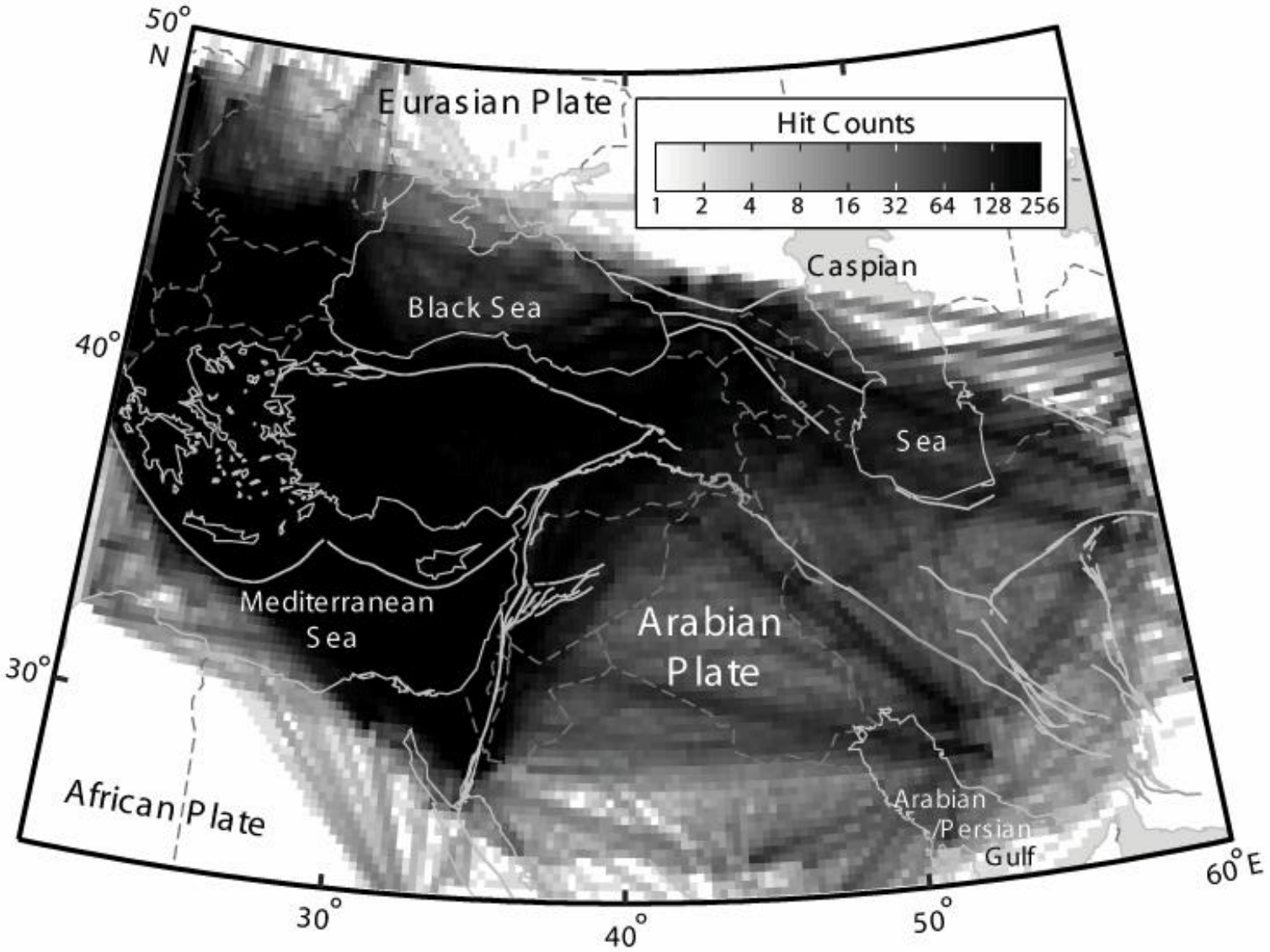
50°
N
Eurasian Plate
Hit Counts
1 2 4 8 16 32 64 128 256
Caspian
Black Sea
40°
Sea
Mediterranean
Sea
Arabian
Plate
30°
African Plate
Arabian
/Persian
Gulf
60° E
30°
40°
50°

events recorded at various stations is shown in Figure 4 as hit counts for each $0.25^{o}$x$0.25^{o}$ cell. Regions with the highest cell hit counts, > 64 hits, cover most of the area west of the Caspian Sea including Turkey, Greece, the Aegean Sea, southern Romania, eastern Mediterranean Sea, and the DSF system (Figure 4.4). Areas with fewer number of ray hits, between 2-64 hits, occupy parts of northern Arabia, Iran, southern Caspian Sea, central and northern Romania, and central and northern Black Sea (Figure 4.4).

**RESOLUTION ANALYSIS**

Although it is customary to discuss resolution analysis after presenting the inversion results, we will start discussing resolution analysis beforehand in order to give the reader a feeling of the data resolution capacity in the study area. A synthetic checkerboard model ($2^{o}$x$2^{o}$), including a Gaussian random noise of one second amplitude, was used to test data coverage resolution using the same damping parameters of the tomographic model inversion. The input synthetic velocity checkerboard (Figure 4.5a) is made of alternating high (+ 0.25 km/s) and low (-0.25 km/s) velocity anomalies, while the anisotropy checkerboard (Figure 4.6a) was made of alternating E-W and N-S fast directions with 0.25 km/s magnitude for both orientations.

The velocity checkerboard test results could be categorized into two end-member levels of resolution in the study area. The highest level of resolution is in regions where checkers' shape, magnitude, and polarity are well resolved. This level occurs in the Aegean region and western Turkey. The lowest level of resolution where no shape, nor magnitude, nor polarity is clearly resolved occurs only in a small portion of the border zone between Iraqi and Saudi Arabian territories and at the model edges (Figure 4.5b) due to lack of data coverage in these regions. We have reasonably good

**Figure 4.5a.** Checkerboard synthetic velocity anomalies used to test the ability of the available stations and events coverage to resolve a $2^{o}$x$2^{o}$ velocity checkers. The anomaly amplitudes alternate between -0.25 km/s and +0.25 km/s velocity. (See Figure 4.1 for geographic locations).

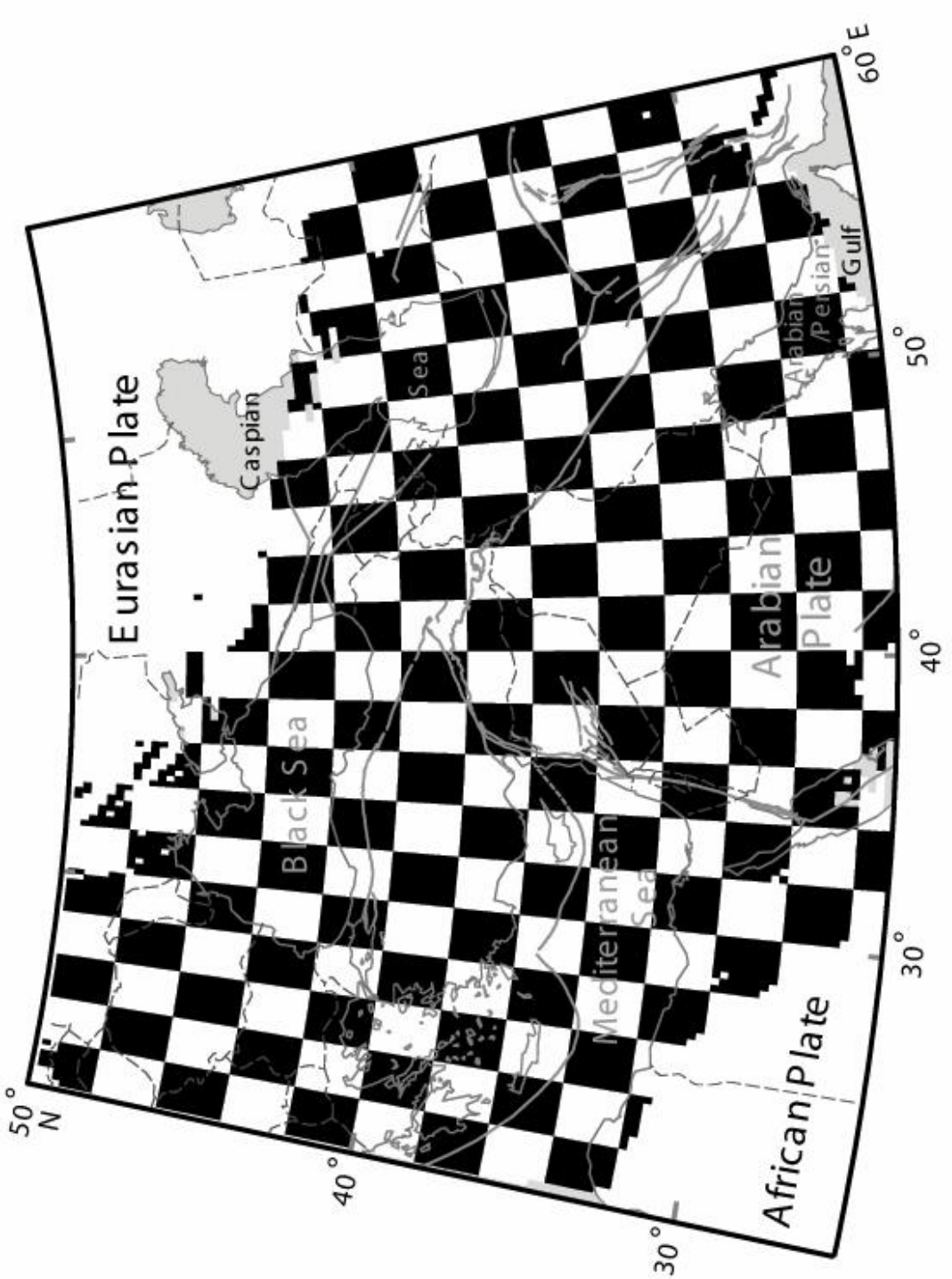
Eurasian Plate
Caspian Sea
Black Sea
Mediterranean Sea
Arabian Plate
Arabian/Persian Gulf
African Plate
50° N
40°
30°
30°
40°
50°
60° E

**Figure 4.5b.** Pn velocity checkerboard test result. (See Figure 4.1 for geographic locations).

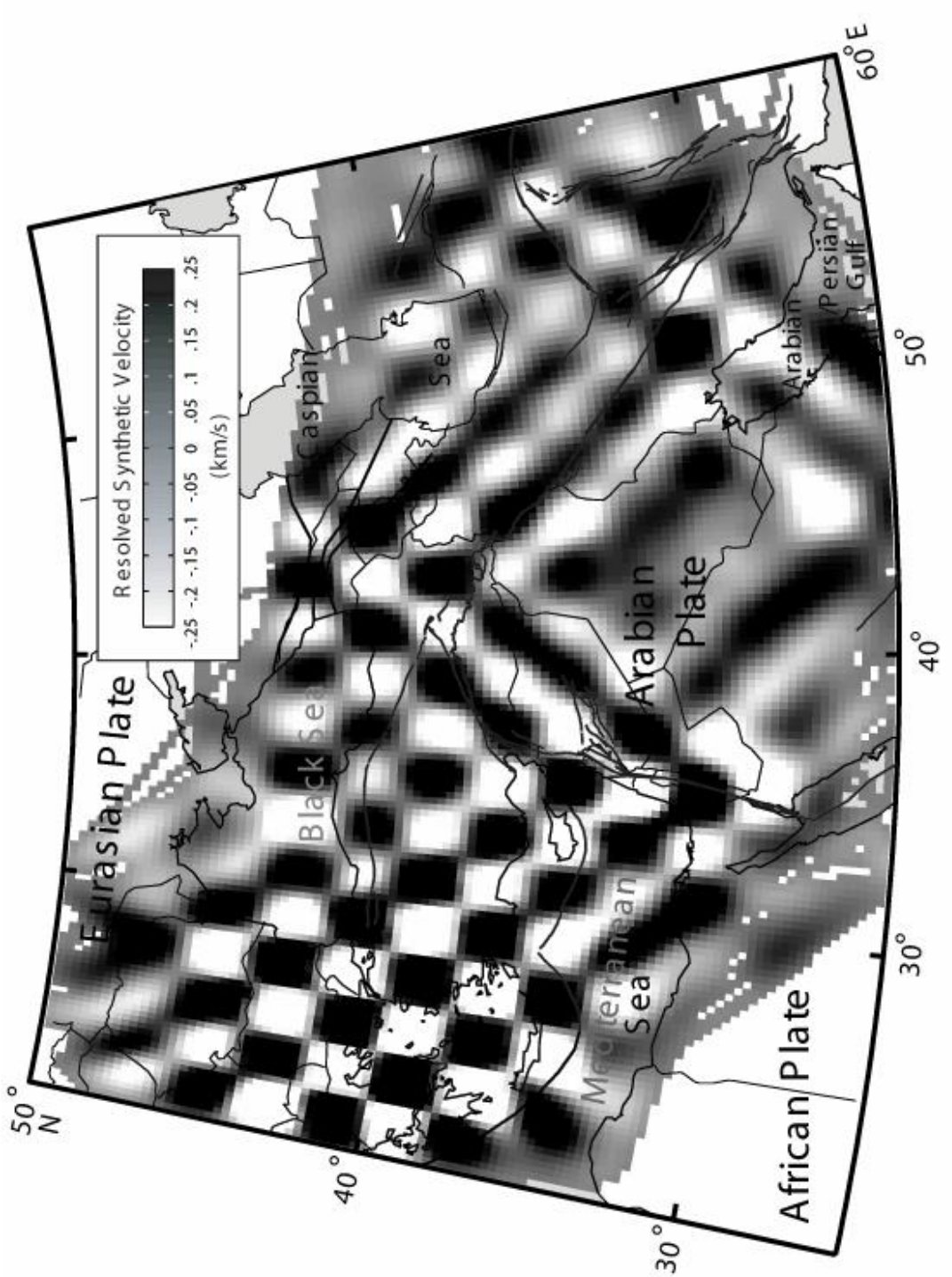
Resolved Synthetic Velocity
-.25 -.2 -.15 -.1 -.05 0 .05 .1 .15 .2 .25
(km/s)
Eurasian Plate
Black Sea
Caspian Sea
Arabian Plate
Arabian Sea
Persian Gulf
African Plate
Mediterranean Sea
50° N
40°
30°
30°
40°
50°
60° E

**Figure 4.6a.** Checkerboard synthetic anisotropy anomalies used to test the ability of available stations and events coverage to resolve a $2^{o}$x$2^{o}$ anisotropy checkers. The checkers are made of alternating N-S and E-W anisotropy orientations of a 0.25 km/s magnitude. (See Figure 4.1 for geographic locations).

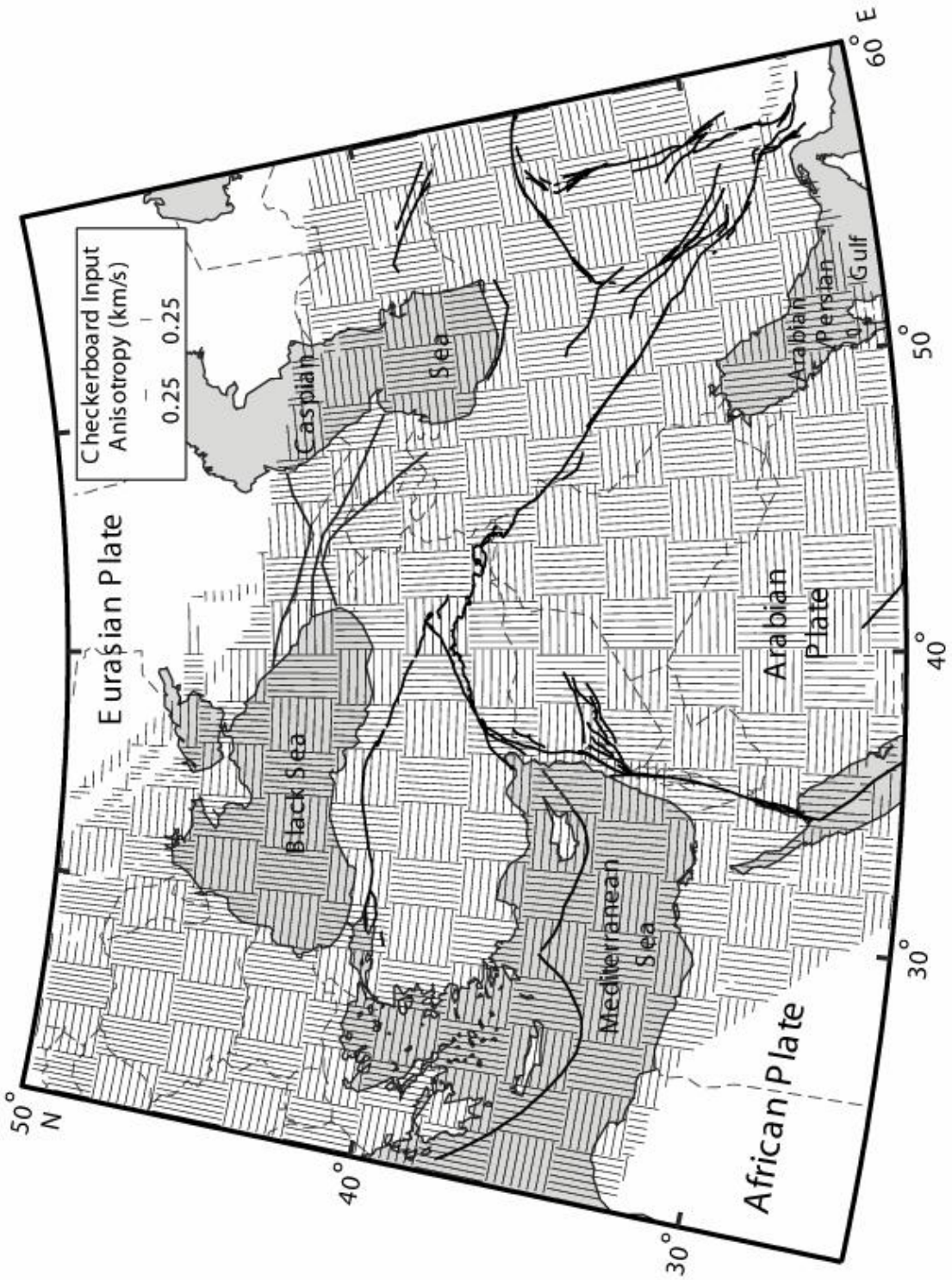
Checkerboard Input
Anisotropy (km/s)
0.25 0.25
Eurasian Plate
Caspian Sea
Black Sea
Mediterranean Sea
Arabian Plate
Arabian Persian Gulf
African Plate
50° N
40°
30°
50°
40°
30°
60° E

**Figure 4.6b.** Pn anisotropy checkerboard test result. (See Figure 4.1 for geographic locations).

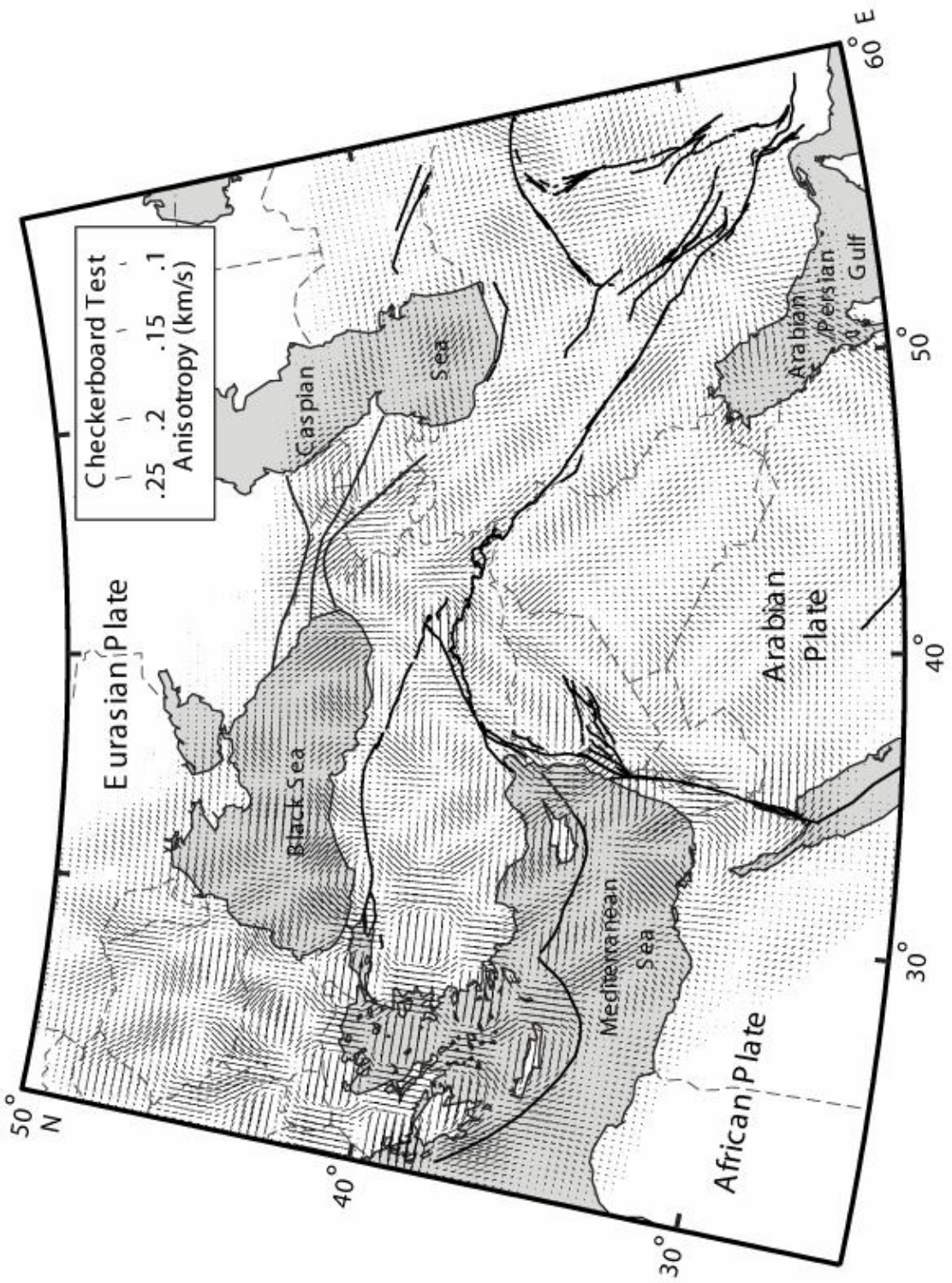
Checkerboard Test
.25 .2 .15 .1
Anisotropy (km/s)
Eurasian Plate
Caspian Sea
Black Sea
Mediterranean Sea
Arabian Plate
Arabian Peninsula
Persian Gulf
African Plate
50° N
40°
30°
30°
40°
50°
60° E

resolution of both the shape and magnitude of our test anomalies in central and eastern Turkey. However, our model appears to have poor resolution in central and northern Iran. The resolution is higher in southern and northeastern Iran in regions directly northeast of the Arabian/Persian Gulf (Figure 4.5b).

The two end-member resolution levels also apply to the anisotropy checkerboard test results (Figure 4.6b). The highest level of resolution, with complete recovery of shape, magnitude, direction and polarity occurs within the Aegean region, Greece, and western Turkey (Figure 4.6b). Reasonably good anisotropy resolution is obtained along the DSF system, central to eastern Turkey, Romania, Bulgaria, and the Caucasus region. Within these areas there is some smearing of our test anomalies. One example is the southwestern portion of EAF zone where anisotropy directions are NE-SW oriented (Figure 4.6b). Because anisotropy involves the determination of orientations, it is more prone to smearing effects due to uneven station and event distributions. This is exemplified in northern Iran, where unresolved anisotropy orientations form parallel zones of similar anisotropy orientations along the same areas with the velocity smearing paths (Figure 4.6b). A zone with relatively improved shape and orientation resolutions, but smaller magnitudes occupies the region directly northeast the Arabian/Persian Gulf.

## INVERSION RESULTS

### Pn velocity anomalies

Pn velocity tomography with an anisotropy component shows two scales of low Pn velocity anomalies (Figure 4.7a). First, a broader scale (~500 km) low (< 8 km/s) Pn velocity anomaly underlies northwestern Iran, eastern Anatolia, the Caucasus, and most of the Anatolian plate. These broad scale low Pn velocity

**Figure 4.7a.** A map showing the Pn velocity tomographic results including Pn anisotropy. The image shows a broader scale low Pn velocity (< 8 km/s) anomaly underlying the boundary zone of Arabia and most of the Anatolian plate. Within the broader low velocity zone anomalies shorter scale very low Pn velocity (< 7.8 km/s) anomalies underlie southern Syria, the Lesser Caucasus region, the Isparta Angle, and central Turkey. (See Figure 4.1 for geographic locations).

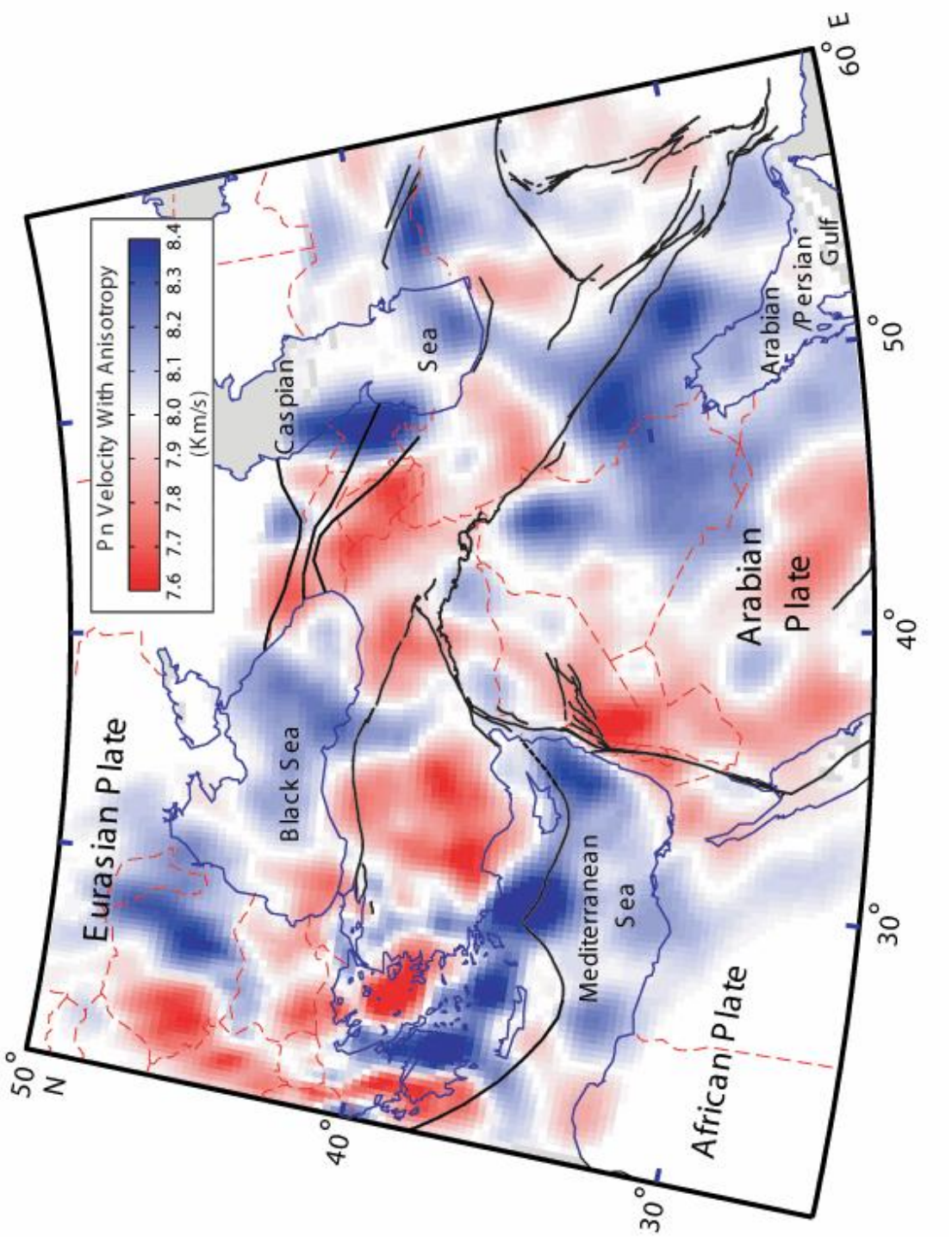
Pn Velocity With Anisotropy
7.6 7.7 7.8 7.9 8.0 8.1 8.2 8.3 8.4
(Km/s)
Eurasian Plate
Black Sea
Caspian
Sea
Mediterranean
Sea
Arabian
Plate
Arabian
Persian
Gulf
African Plate
50° N
40°
30°
30°
40°
50°
60° E

anomalies occupy regions within the Eurasian side of the Eurasia-Arabia collision zone. In central Iran fast Pn velocities appear to extend beyond the Zagros suture line, while in northwestern Iran and eastern Turkey the high Pn velocities are limited to the region immediately south of the Bitlis suture and the EAF zone (Figure 4.7a). At the northwestern boundary of the Arabian plate a broad, low Pn velocity anomaly underlies the DSF system and western Arabia plate proper (Figure 4.7a). Farther south the latter broad anomaly extends to underlie the Sinai and Levantine region (Figure 4.7a). Northwestern Arabia's broad low Pn velocity anomaly extends only as far north as central and western Syria. Minor low velocity tongues, partly caused by smearing, extend within the fast velocity zone south of the BS and EAF zone.

Second, five smaller scale (~200 km) anomalies with Pn velocities lower than 7.8 km/s are found to underlie areas within the broader scale low velocity anomalies. Those shorter scale anomalies occur beneath southernmost Syria and northern Jordan, the Lesser Caucasus, the Isparta Angle and central Turkey. An isolated shorter scale low velocity anomaly underlies a region in the northern Aegean Sea and parts of westernmost Turkey. Other low Pn velocity anomaly zones underlie western Greece, Bulgaria, western Romania and easternmost Yugoslavia (Figure 4.7a).

Zones of high Pn velocities (8-8.4 km/s) underlie the interior of the Arabian plate (including the Zagros fold belt), the southern Caspian Sea extending eastward beneath the Kopeh Dagh and westwards beneath Azerbaijan, the Black Sea, and most of the eastern Mediterranean Sea. Other regions showing high Pn velocity within the broad low velocity anomalies underlie regions within the Central Iranian Microplate (CIM) and a corridor directly south of the Caspian Sea that extends southwest to the Zagros fold belt (in northern Iran), and two corridors in the eastern and western parts of the Anatolian plate (Figure 4.7a). Also, we observe zones of very high Pn velocity (> 8.2 km/s) beneath regions directly north of the Hellenic arc, the intersection

between the Cyprean and the Hellenic arcs, in eastern Romania, and Azerbaijan (western Greater Caucasus).

We found only subtle differences in Pn velocities when not including anisotropy in our tomographic inversion (Figure 4.7b). Anisotropy effect appears to be the strongest under the Anatolian plate, Aegean Sea, Hellenic arc, and under the Black Sea. Generally, including the anisotropy component in the Pn velocity inversion focuses anomalies. For example, the northern Aegean Sea shorter scale, very low Pn velocity anomaly (Figure 4.7a) becomes spread out within the Aegean Sea and western Turkey in the isotropic model (Figure 4.7b). Including an anisotropy component laterally displaces the anomalies. For example, in the isotropic model (Figure 4.7b), the high velocity anomaly southwest of the Hellenic Arc is displaced to the northeast of the Hellenic Arc, within the Aegean Sea (Figure 4.7a). Similarly, the low velocity anomaly along western Greece (Figure 4.7a) is replaced by a high velocity anomaly at the corresponding area in the isotropic model (Figure 4.7b). Because of the fewer paths in the eastern parts of the study area, we observe no significant differences between the isotropic and anisotropic models. The high velocity corridor, directly south of the southern Caspian Sea, is caused by including anisotropy (Figure 4.7a) in the inversion and therefore it needs to be interpreted cautiously since that region does not show good azimuthal coverage of ray paths.

To further test for possible uncertainties in the inverted anisotropic Pn velocity model, we used a bootstrap technique used by Hearn (1996). The bootstrap method iteratively re-samples the data pool and reruns the inversion using the standard deviation in bootstraped velocities as proxies for errors of the model. Bootstrap errors for our Pn velocity model are typically less than 0.05 km/s throughout the study area (Figure 4.8). Few zones showed errors higher than 0.05 km/s. Those regions with large

**Figure 4.7b.** A map showing the optimal isotropic Pn velocity model. This model shows minor differences from the anisotropic model of Figure 4.7a. Notice the difference in the Aegean Sea region, where higher velocities south of the Hellenic arc are displaced northwards inside the Sea of Crete and southern Aegean Sea. (See Figure 4.1 for geographic locations).

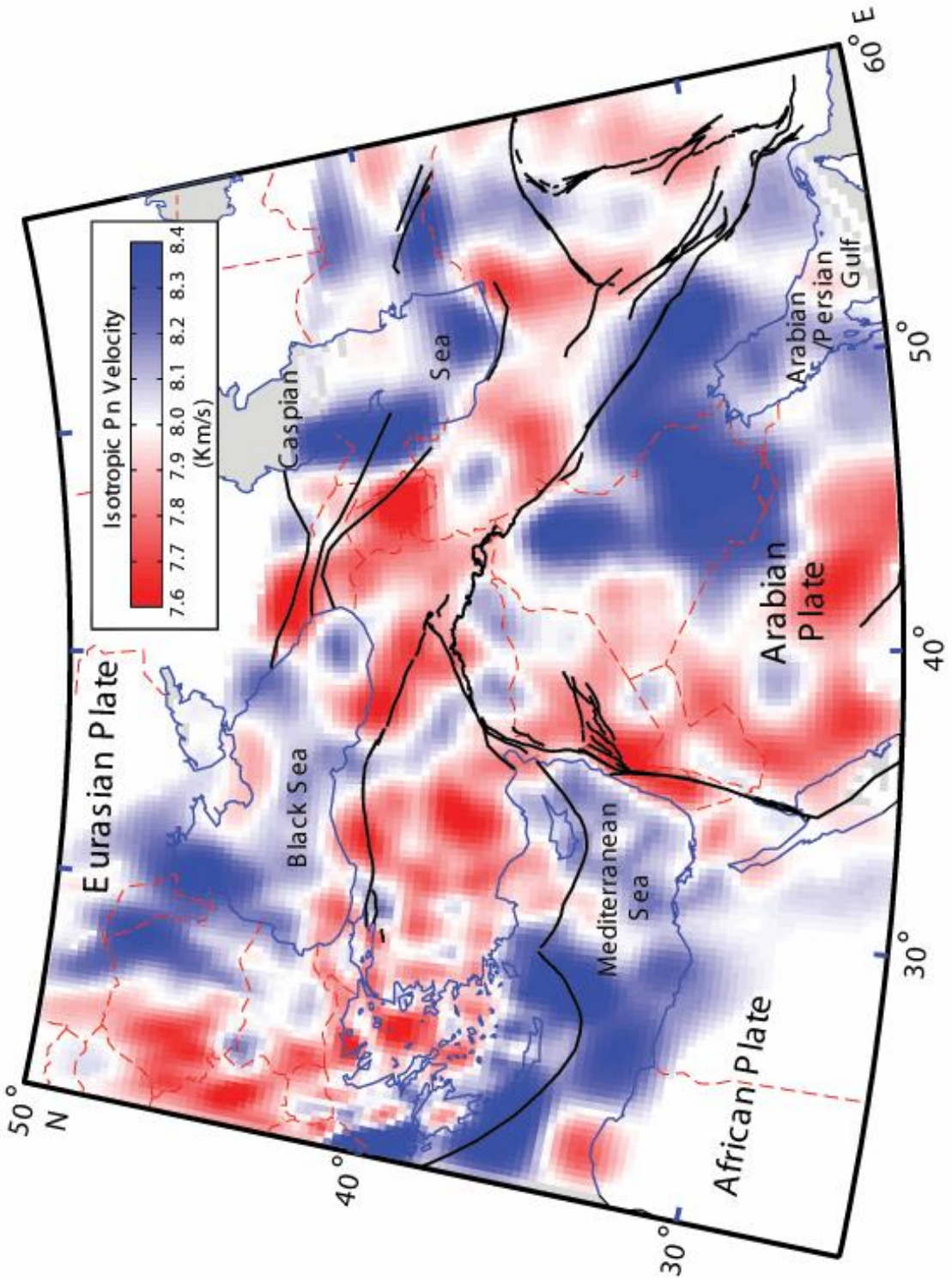
Isotropic Pn Velocity
(Km/s)
7.6 7.7 7.8 7.9 8.0 8.1 8.2 8.3 8.4
Eurasian Plate
Black Sea
Caspian Sea
Mediterranean Sea
Arabian Plate
Arabian Persian Gulf
African Plate
50° N
40°
30°
30°
40°
50°
60° E

**Figure 4.8.** A map showing Pn velocity errors calculated using 100 bootstrap iterations. (See Figure 4.1 for geographic locations).

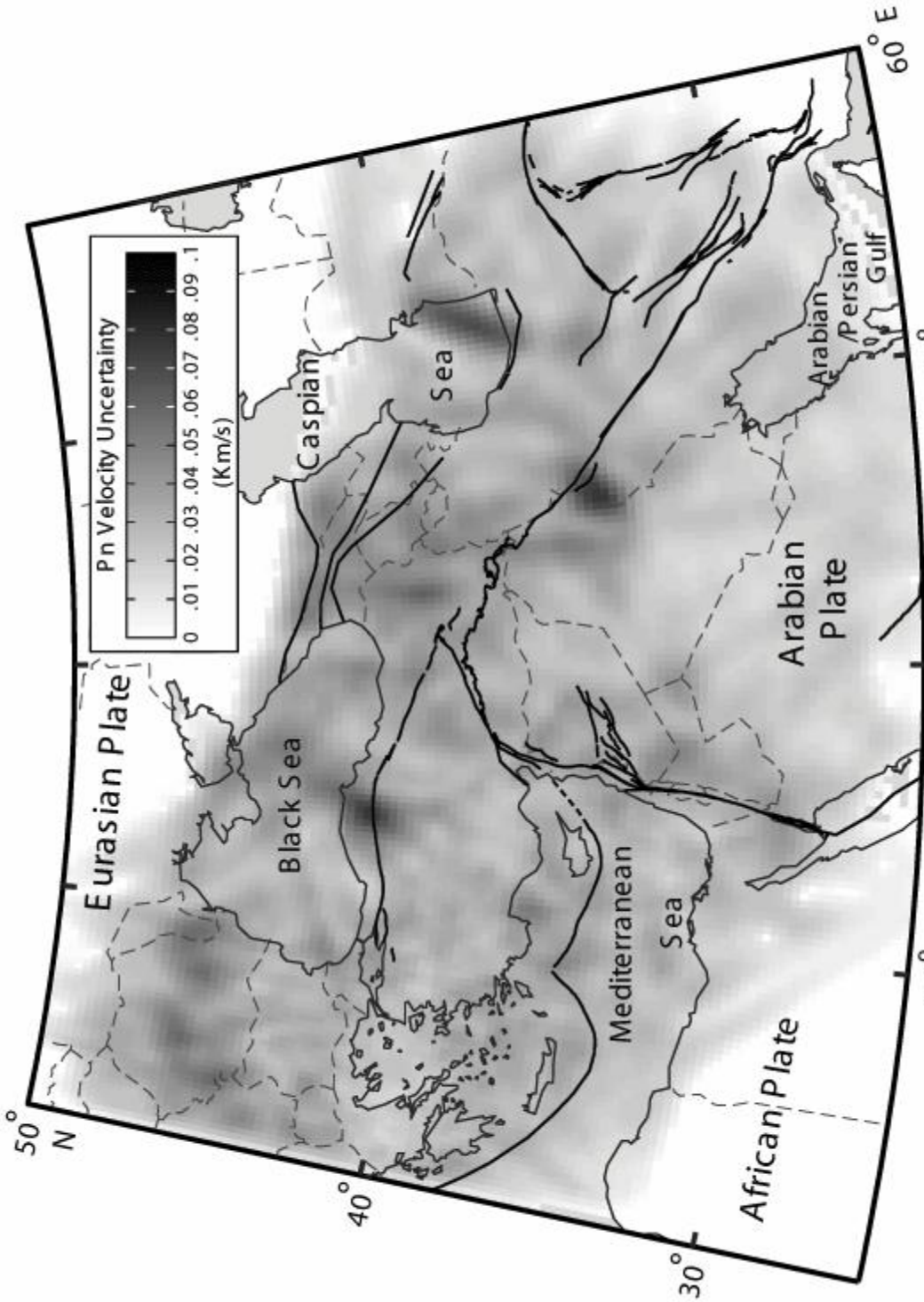
Pn Velocity Uncertainty
0 .01 .02 .03 .04 .05 .06 .07 .08 .09 .1
(Km/s)
Eurasian Plate
Black Sea
Caspian Sea
Mediterranean Sea
Arabian Plate
Arabian Persian Gulf
African Plate
50° N
40°
30°
30°
40°
50°
60° E

errors included the southeastern tip of the Caspian Sea, a small area along the northern Zagros Fold Belt, and a small area along the NAF zone (Figure 4.8).

**Pn anisotropy**

Figure 4.9 shows the resulting anisotropy magnitudes and directions inverted simultaneously with Pn velocity. Observed anisotropy magnitudes varied between 0.0 to 0.65 km/s. The largest anisotropy values occur within the Aegean Sea (~0.6 km/s), the Hellenic arc (~0.65 km/s), southern portion of the Dead Sea fault system (~0.45 km/s), and across the easternmost segment of the NAF zone (~0.5 km/s). Smaller anisotropy (~0.2 km/s) magnitudes are observed within the Arabian plate and the zones east of it (Figure 4.9). These variations in anisotropy magnitudes could be in part due to the uneven data coverage (i.e. we have damped our inversion in such a way that in regions with poor resolution tend to have smaller anisotropy magnitudes).

Unlike the tomographic velocity anomalies, observed anisotropy anomalies show a higher degree of lateral variability. We observed sudden anisotropy changes across plates and along plate boundaries. Since not all anisotropy values are well resolved we will address only those regions with good anisotropy resolution. Within the Anatolian plate anisotropy fast axes are predominantly E-W in the east, N-S at the center and E-W in western Turkey. Similar sudden changes in anisotropy are observed along the DSF system, where two different trends of anisotropy orientations are observed (Figure 4.9). A predominantly E-W fast anisotropy orientation is present along the northern parts of the DSF system. A NE-SW anisotropy orientation is imaged along the southern portion of the DSF system. Anisotropy orientations along the DSF system show consistency along a narrower band in the inland regions. This contrasts with wider zones of consistency in the Mediterranean Sea side (Figure 4.9). The zone parallel to the DSF system's restraining bend in southern Syria marks the

**Figure 4.9.** A map showing Pn azimuthal anisotropy orientations. Compared to Pn velocity of Figure 4.7a, Pn anisotropy orientations display a higher degree of lateral variations in the region. (See Figure 4.1 for geographic locations).

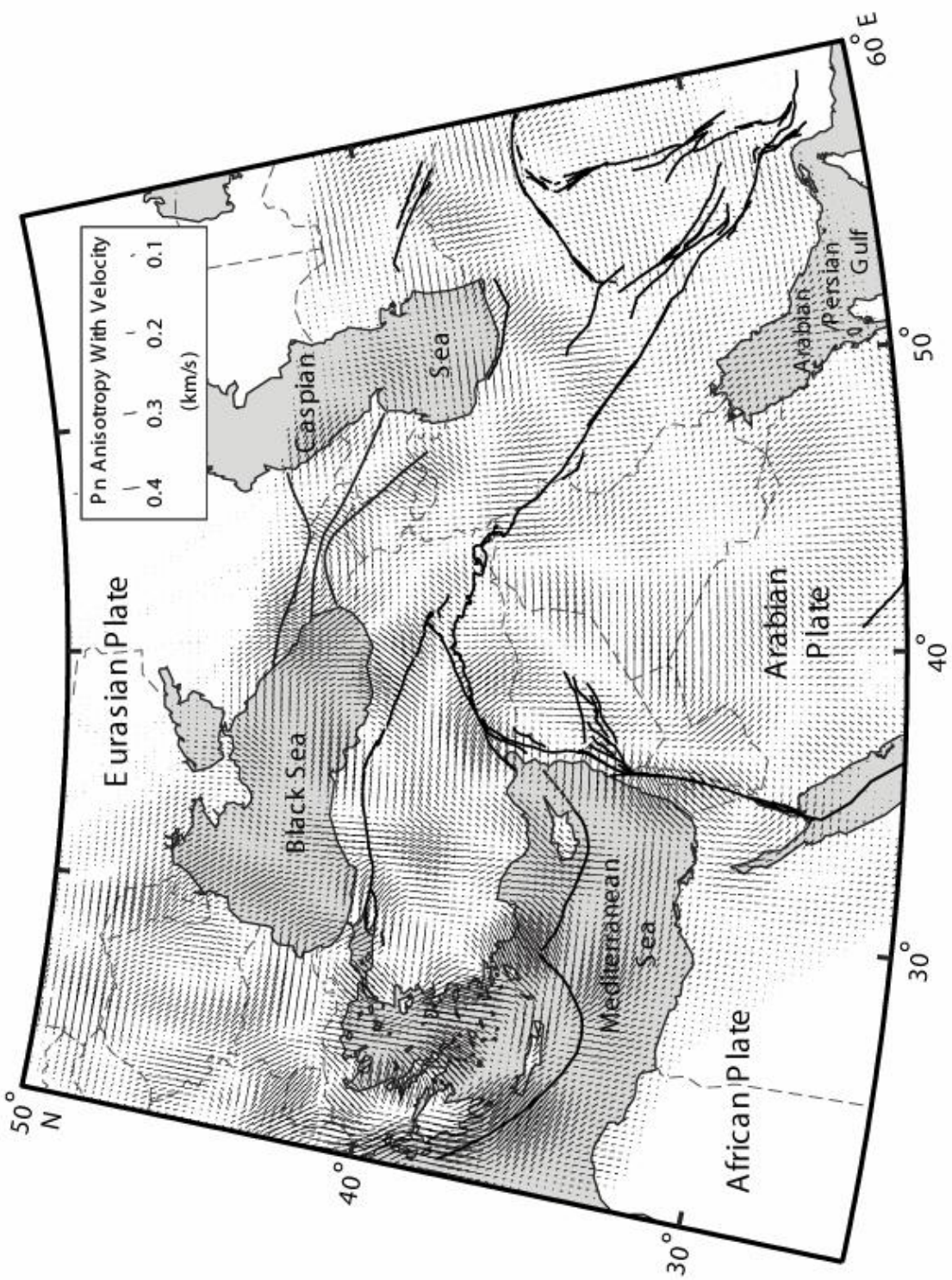
Pn Anisotropy With Velocity
0.4
0.3
0.2
0.1
(km/s)
Eurasian Plate
Caspian Sea
Black Sea
Mediterranean Sea
Arabian Plate
Arabian Persian Gulf
African Plate
50° N
40°
30°
30°
40°
50°
60° E

change in anisotropy orientation from a NE-SW in the south to an E-W orientation in the north (Figure 4.9). East of the DSF, in central Arabia platform and along the northern Zagros fold belt, the anisotropy orientations are regarded erroneous due to the limited ray coverage (Figure 4.9).

The Aegean region shows considerable variations in anisotropy orientation. In the south, anisotropy orientations are parallel to the Hellenic Arc (arc parallel anisotropy). Within the Aegean Sea anisotropy is dominantly N-S oriented except for a zone in the northern Aegean Sea, where anisotropy is NW-SE oriented. In eastern Greece and farther southeast in the Aegean Sea anisotropy is NE-SW oriented. The Sea of Crete shows the smallest anisotropy magnitudes, dominantly E-W oriented.

Overall tomographic azimuthal Pn anisotropy shows reasonable correlation with azimuthal anisotropy obtained based on the two station method (Smith and Ekstrom, 1999) in the Aegean region, the Dead Sea fault region and in central and eastern Turkey.

We applied a bootstrap error analysis on observed Pn anisotropy as well. Comparably low (< 0.05 km/s) errors are also observed for the anisotropy portion of the model with almost equal magnitude velocity errors (Figure 4.10). This may be due to the fact that we used the same damping on both velocity and anisotropy solutions (Figure 4.10).

**Pn station delays**

Assuming excellent ray coverage, station delays contain the integrated information about the crustal thickness and average velocity variations of the crust (Figure 4.11). Considering that the delay is due to the crustal structure near the station, a station delay of ±1 second corresponds to ~10 km difference in crustal thickness or ~0.7 km/s velocity difference from the assumed crustal velocity model. Station delays

**Figure 4.10.** A map showing Pn anisotropy errors using 100 bootstrap iterations. (See Figure 4.1 for geographic locations).

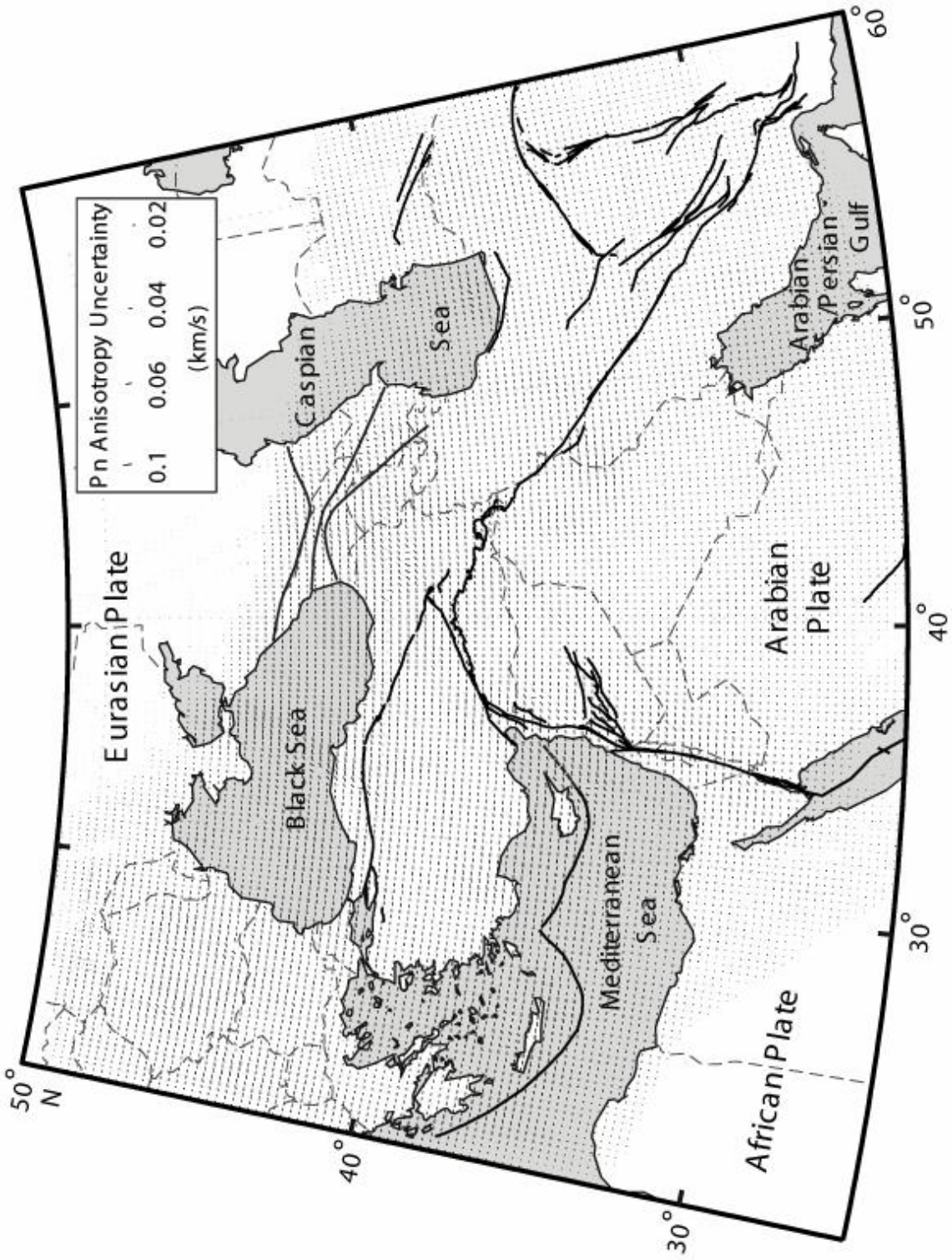
Pn Anisotropy Uncertainty
0.1 0.06 0.04 0.02
(km/s)
Eurasian Plate
Black Sea
Caspian Sea
Mediterranean Sea
Arabian Plate
Arabian Persian Gulf
African Plate
50° N
40°
30°
30°
40°
50°
60°

**Figure 4.11.** A map showing stations delay. Squares represent thick and/or slow crust, circles represent fast and/or thin crust (See Figure 4.1 for geographic locations).

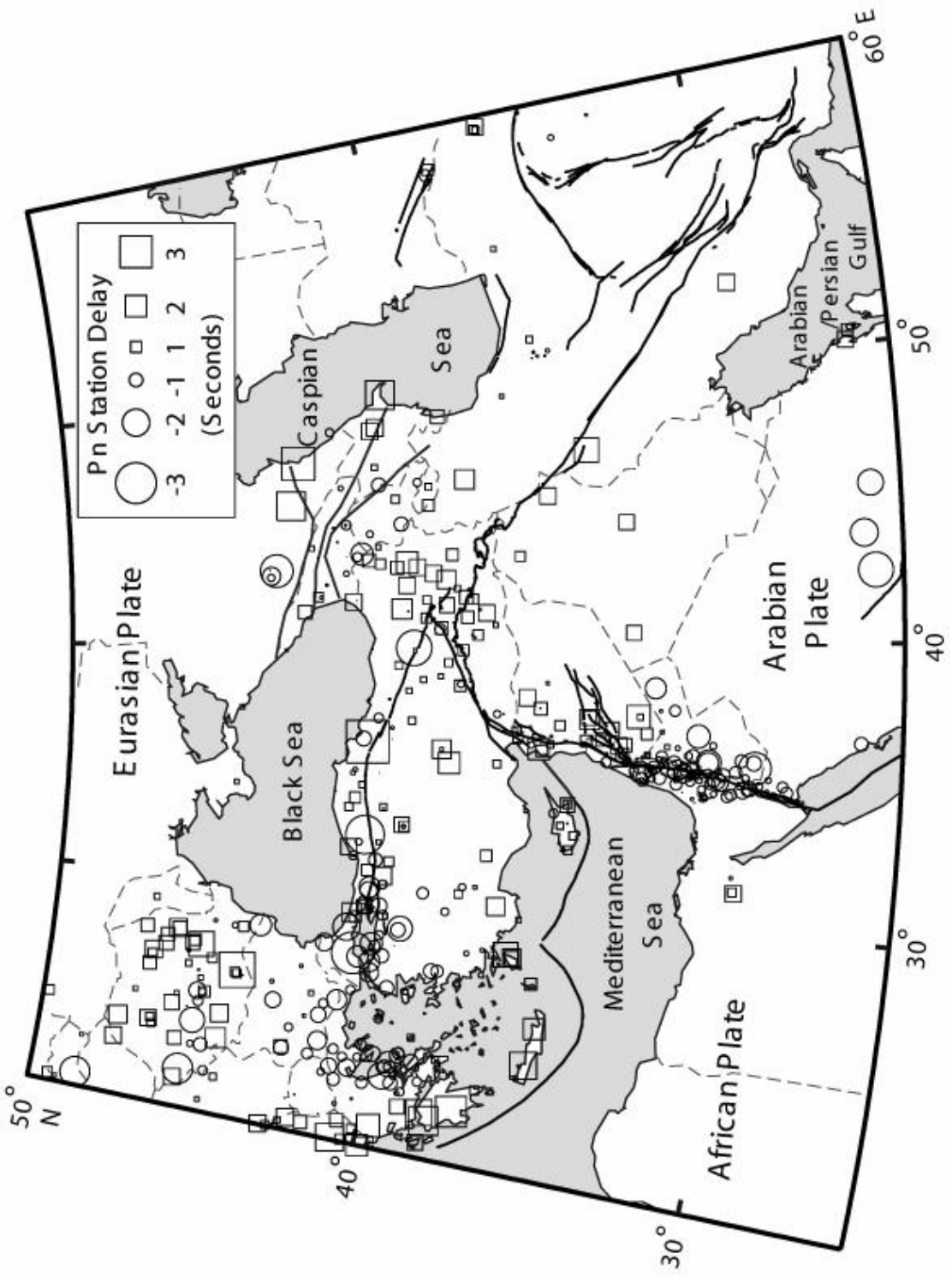
Pn Station Delay
-3 -2 -1 1 2 3
(Seconds)
Eurasian Plate
Caspian Sea
Black Sea
Mediterranean Sea
Arabian Plate
Arabian Persian Gulf
African Plate
50° N
40°
30°
50°
40°
30°
60° E

obtained in our inversion varied between -3 seconds to +3 seconds. Anomalous station delays in excess of 3 seconds are observed at a few stations and may indicate systematic phase picking errors and/or systematic clock problems at those stations (Grand, 1990; Hearn, 1996).

Clusters of systematic positive, negative, or mixed station delays observed at different regions of the study area may bear some information about the crustal structure (Figure 4.11). Positive station delays are mainly indicative of thick and/or slow crust compared to the assumed model. Regions showing clusters of positive station delays are located along the northern segment of the Dead Sea fault system, in eastern Turkey (mostly ETSE stations), along the Cyprean and the Hellenic arcs, and within Romanian territory (Figure 4.11). Negative station delays are indicative of a thin and/or fast crust compared to the assumed model. Zones with negative station delay clusters are those found in the northern Aegean Sea and areas around it including eastern and northern Greece and northwestern Turkey (around the Sea of Marmara), and along the southern portion of the DSF system (Figure 4.11).

## DISCUSSION AND CONCLUSIONS

### Rheology and structure

The Pn velocity results provide detailed insights about the rheology and dynamics of the mantle processes in the region. High (> 8 km/s) Pn velocity zones found in portions of Arabia, the Mediterranean, Black, and Caspian Seas are used to infer the presence of stable mantle lid in these regions. Low Pn velocities found beneath the junction of the Arabian, Eurasian, and African plates are used to infer the presence of anomalously hot and/or thin mantle lid (Figure 4.12). The broad scale, low

**Figure 4.12**. A comparative map showing Pn velocity with anisotropy (base map, red-blue color, see Figure 4.7a), volcanic outcrops in green and pink polygons filled with plus signs, Sn attenuation zones in yellow lines hatched areas enclosed by a solid gray line (after Khaled Al-Damegh, personal communication, June 2002), and volcanoes in yellow triangles. (See Figure 4.1 for geographic locations).

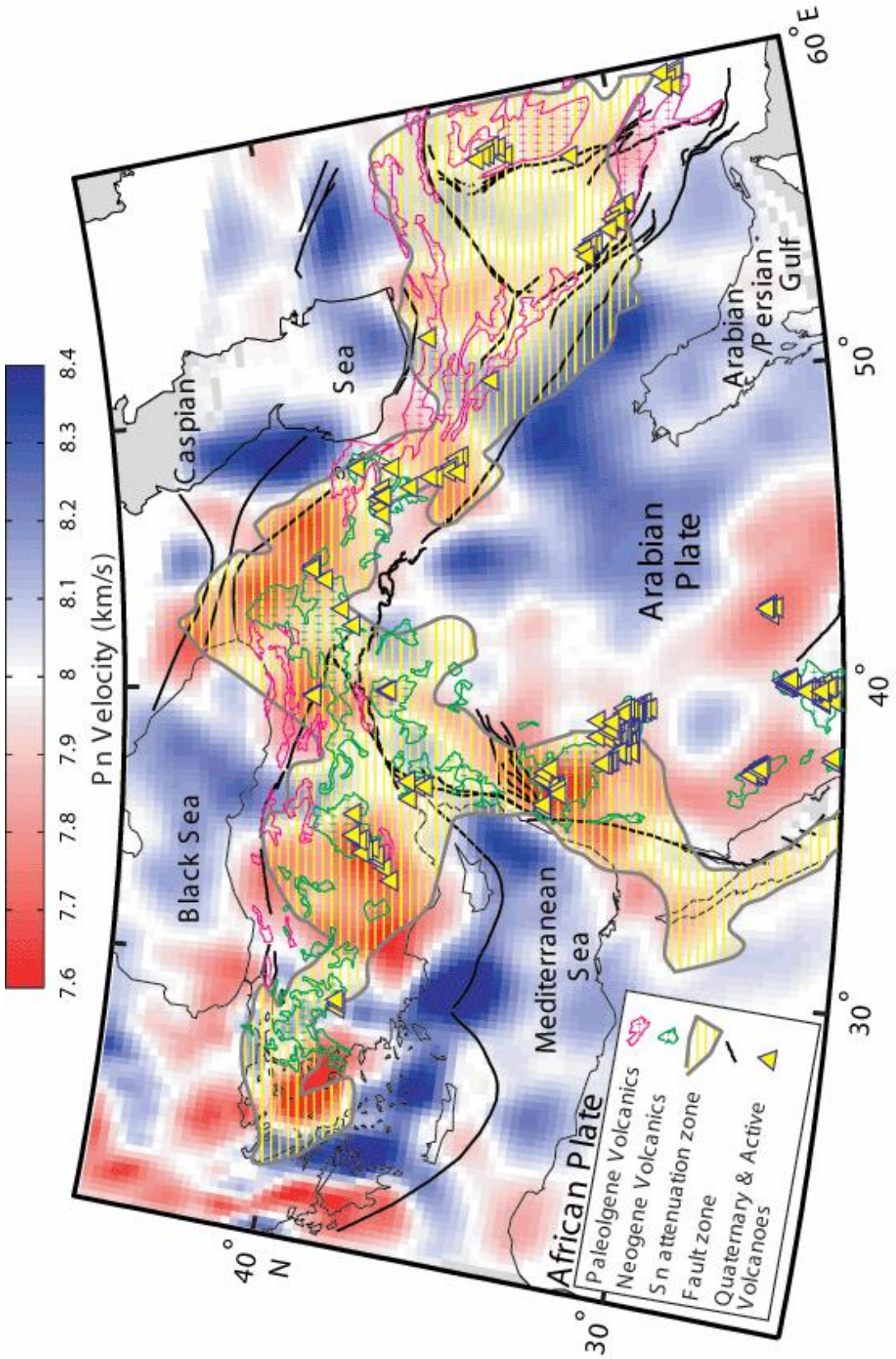
Pn Velocity (km/s)
7.6
7.7
7.8
7.9
8
8.1
8.2
8.3
8.4
Black Sea
Caspian
Sea
Mediterranean
Sea
Arabian
Plate
Arabian
/Persian
Gulf
African Plate
Paleolgene Volcanics
Neogene Volcanics
Sn attenuation zone
Fault zone
Quaternary & Active
Volcanoes
40°
N
30°
30°
40°
50°
60° E

Pn velocity anomalies beneath northwestern Iran, the Caucasus, and eastern Anatolia is interpreted to originate from a different geodynamic process compared to the low Pn velocity anomaly beneath the northwestern Arabia plate (Figure 4.12). The regions of the Lut Block (LB) and the Central Iranian Microplate (CIM) are associated with volcanic activity throughout the Paleogene and most of the Neogene times (Figures 4.1 and 4.12). However, a later stage of volcanic activity in eastern Turkey and northwestern Iran is known to have started in the Late Miocene and continued to historical times (e.g., Yilmaz, 1990; Keskin et al., 1998). This volcanic activity is possibly related to earlier subduction of the Neo-Tethys oceanic lithosphere. A lithospheric delamination event in the Plio-Quaternary time may also significantly contribute to the observed widespread volcanism. Such processes may explain the anomalous nature of the lithosphere in these regions. Within the broad low Pn velocity anomalies, zones of high Pn velocity (implying stable mantle lid) underlie the central CIM, a corridor directly south of the Caspian Sea, and a small area in northwestern Iran (Figures 4.1 and 4.12). The corridor directly south of the Caspian Sea is observed only in the model with anisotropy and therefore should be considered cautiously due to the poorly resolved anisotropy in that region (Figures 4.6b and 4.7b).

A careful examination of the boundary of the high Pn velocity zone beneath the southern Zagros shows that the high velocity area extends for ~100 km northeast of the Zagros suture line (Figures 4.12 and 4.7a). We interpret this region of high Pn velocity to possibly indicate that stable Arabia is underthrusting the southern parts of the Sanandaj-Sirjan region (Eurasia). This interpretation is in agreement with Snyder and Barazangi (1986) who concluded that Arabia is being underthrust beneath the southern parts of the Sanandaj-Sirjan region. The checkerboard resolution tests, however, in this region show that our spatial resolution is poor, and, hence, this interpretation may be incorrect. Farther north the high Pn velocity zone underlies only

regions directly south of the Zagros-Bitlis suture line. We are confident based on our resolution tests that in the northern parts of the Zagros-Bitlis region underthrusting of Arabia is very limited or absent as evidenced by a sudden change in Pn velocities across the suture line.

One of the most important results of this study is the discovery of a low Pn velocity zone beneath the Dead Sea fault system and the northwestern Arabian plate. Sandvol et al. (2001a) showed that Sn is attenuated beneath the entire Dead Sea fault system, but the extent and location of the anomaly was ambiguous due to limited resolution. In this study, we use better event-station distribution in the region to quantify the mantle lid velocity beneath northwestern Arabia and the DSF system. We find the broad, low Pn velocity anomaly is not centered along the DSF system, but rather extends a considerable distance within the Arabian plate proper. Also, the very low Pn velocity anomaly beneath southern Syria and northern Jordan is located east of the DSF system axis. The anomalous low Pn velocity zone is asymmetrical relative to the DSF. Whether or not this anomalous lithospheric mantle is a direct result of the development of the DSF system is arguable. We argue against this possible interpretation owing to the velocity anomaly's asymmetry with respect to the DSF plate boundary and its extent eastwards beneath the northwestern Arabia plate proper. The broad low Pn velocity zone underlying the DSF system and northwestern Arabia coincides at the surface with relatively young volcanic outcrops (Neogene/Quaternary), while the very low Pn velocity (7.6 km/s) anomaly is overlain by Quaternary and Holocene volcanoes. We interpret the low Pn velocity anomaly beneath the DSF system and northwestern Arabia as a possible northward extension of the anomalous mantle beneath the Red Sea spreading system. This broad region of thin, hot mantle lithosphere may have facilitated the development of the DSF system in the Neogene time.

The presence of partial melt lowers normal lithospheric mantle velocities by at least five to six per cent (Sato et al., 1989). If we are to consider 8.2 km/s is the normal Pn velocity, then 6% slower Pn velocity would allow us to consider the smaller scale very low Pn velocity anomalies beneath southern Syria, the Isparta Angle, central Turkey, the Lesser Caucasus, and the northern Aegean Sea as zones of possible partial melt, i.e. the lithospheric mantle is absent (Figure 4.12). These very low Pn velocity anomalies correspond at the surface with Holocene volcanoes (Figure 4.12). The very low Pn velocity (7.5 km/s) centered at the northern Aegean Sea is a region where the largest present-day extensional strain rates are observed (Sonder and England, 1989). The northern Aegean back arc extension region extends up to ~42$^{o}$ N and 31$^{o}$ E (Angelier et al., 1982; Jackson, 1994), which is inclusive of the small very low Pn velocity anomaly. The very low Pn velocity (~7.5 km/s) and the thinned crust (26-32 km) beneath the Aegean (Makris and Vees, 1977) is comparable to a rifting system, such as the East African rift system beneath Lake Turkana (Keller et al., 1994). This very low Pn velocity reflects perhaps very thin to absent mantle lid, where Pn propagation is actually sampling asthenospheric rather than lithospheric mantle.

Regions showing stable upper mantle (high Pn velocities) underlie central and eastern Arabia, the southern Caspian Sea extending eastwards beneath the Kopeh Dagh and westward underlying most of Azerbaijan (eastern Greater Caucasus), most of the Black Sea, eastern portions of the Mediterranean Sea, the Sea of Crete and the southern Aegean Sea (Figure 4.7a). The Zagros fold belt is underlain by fast Pn velocity (Figure 4.7a). This is not surprising since the Zagros fold belt is geologically an integral part of the leading edge of the Arabian plate. We also observed zones of very high Pn velocity (> 8.3 km/s) beneath regions directly north of the Hellenic arc, the intersection between the Cyprean and the Hellenic arcs, in eastern Romania, and Azerbaijan (western Greater Caucasus). Finally, zones of high Pn velocity indicative

of stable upper mantle form corridors that divide the Anatolian plate into eastern, central, and western regions, all of which are underlain by low and very low Pn velocity zones (Figures 4.7a and 4.12). The origin and cause of these stable mantle lid corridors is unclear, but the location of the corridor at ~30$^{o}$ E (Figure 4.12) coincides at the surface with the easternmost limit of the region undergoing extensional tectonic in western Turkey and the northern Aegean Sea region.

To further analyze our Pn tomography results we utilized available Sn phase attenuation in the region. Sn is the shear wave comparable to Pn phase traveling within the lithospheric mantle (mantle lid), but is more sensitive to temperature and the presence of melt. Figure 4.12 shows that zones of high Sn attenuation (Khaled Al-Damegh, personal communication, June 2002) correlate spatially with zones of low and/or very low Pn velocity.

**Pn anisotropy and station delays: tectonic implications**

Upper mantle seismic anisotropy is generally attributed to the alignment of olivine (the dominant upper mantle mineral) crystal axes in lattice preferred orientations (LPO) (Ismail and Mainprice, 1998). In continental settings seismic anisotropy often mimics regional tectonic trends observed at the surface (e.g., Hearn, 1996; Savage, 1999; Smith and Ekstrom, 1999), suggesting that during orogenic processes crust and mantle deformation are coupled (e.g., Kendal, 2000).

In this study Pn anisotropy shows a higher degree of lateral variations compared to observed Pn velocity (Figure 4.13). To avoid interpreting artifacts and smearing effects on observed anisotropy orientations, we will focus our interpretations on the Anatolian plate, northwestern Arabia, the Aegean region and the eastern Mediterranean Sea, where anisotropy structure is better resolved. In regions such as the Isparta Angle and the northern Aegean Sea, zones of very low Pn velocity

**Figure 4.13.** A comparative map showing Pn anisotropy in solid blue lines (see Figure 4.9), SKS shear wave splitting in green solid lines (after Sandvol *et al*. 2001b), and GPS vector direction in pink solid lines (after McClusky *et al.* 2000). (See Figure 4.1 for geographic locations).

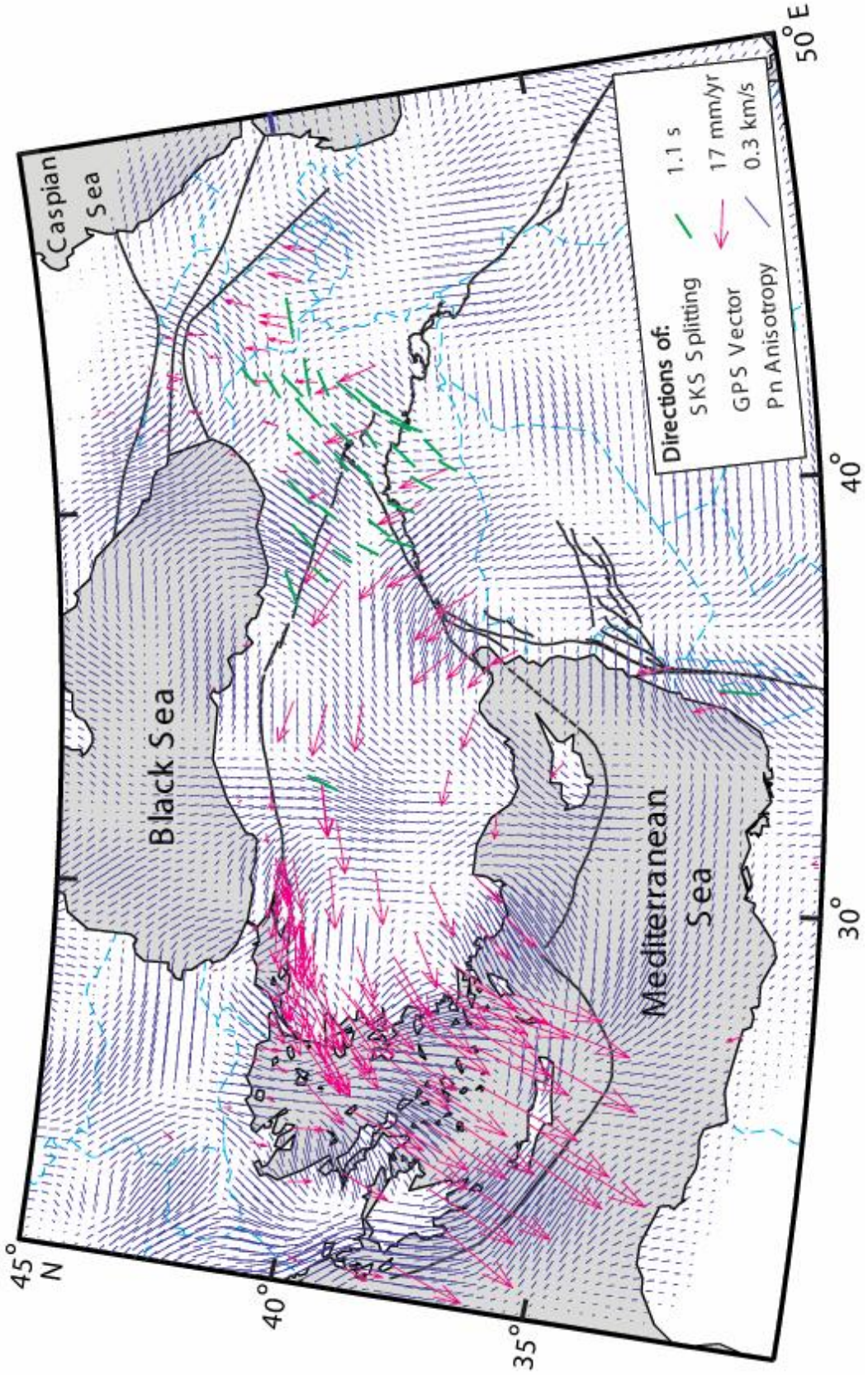
Caspian Sea
Black Sea
Mediterranean Sea
Directions of:
SKS Splitting
GPS Vector
Pn Anisotropy
1.1 s
17 mm/yr
0.3 km/s
45° N
40°
35°
30°
40°
50° E

anomalies showed spatial correlation with zones of distinct and localized Pn anisotropy orientations in the same region. At the convergent boundary between the African and Anatolian plates Pn anisotropy is parallel to the arc trend (arc parallel) between the Hellenic trench and its arc extending to ~$40^{O}$ N, while no clear arc parallel anisotropy is observed south of the Cyprean arc (Figure 4.13).

Along the major strike slip faults (i.e. the NAF and DSF) of the region anisotropy also changes significantly along strike. Anisotropy orientations along the NAF change from NE-SW in the east, to E-W and N-S in the central parts, and to NW-SE in the west close to the Sea of Marmara. Similarly, NE-SW oriented fast axis in the southern portion of the DSF changes to E-W directions north of the restraining bend of the DSF. This change in anisotropy orientations at the restraining bend coincides with changes in the polarity of station delays (Figures 4.11 and 4.13), where the southern segment shows negative station delays and the northern segment shows positive station delays (Figure 4.11). The negative station delays clustered along the southern segment of the DSF system may partly be due to a thinned crust. The systematic change of both station delay clusters and anisotropy orientations might suggest that similar processes (influencing stations delays) influence anisotropy orientations at depth. The station delays for the entire region are shown in Figure 4.11. Although these delays can be used as a first order indication for crustal thickness and/or velocity variations in the crust, a cautious approach is needed in interpreting these results as noise and site effects may also influence the results.

While Pn anisotropy is a measure of azimuthal anisotropy in the uppermost mantle, shear wave (SKS) splitting results available in the region provide polarization anisotropy information within the entire upper mantle. Fast SKS shear wave splitting determined for ETSE stations in eastern Turkey and a station in central Turkey (Sandvol et al., 2001b) generally showed NE-SW fast orientations, while a station in

the southern segment of the DSF system shows about N-S orientation (Figure 4.13). Along the NAF zone and farther southeast in eastern Turkey azimuthal Pn anisotropy matched polarized anisotropy of SKS fast splitting orientations, while no obvious match is observed in the rest of ETSE stations. NE-SW anisotropy orientations surrounding the easternmost segment of the NAF also correspond with a zone of relatively very low Pn velocity (Figures 4.12 and 4.13). This implies a thinned or absent mantle lid in the region surrounding the easternmost portion of the NAF and farther southeast directly north of BS, and that Pn anisotropy and SKS splitting are both sampling asthenospheric deformation. While SKS orientations in central Turkey show very good match with Pn azimuthal anisotropy, the stations along the southern segment of the DSF system show clear discrepancy.

We also used available GPS measurements in the region to possibly relate observed surface plate motion with Pn anisotropy orientations. Eurasia fixed GPS vector directions (McClusky et al., 2000) within the Anatolian plate do not show a clear relationship with observed Pn anisotropy orientations (Figure 4.13). The observed sudden variations of Pn anisotropy orientations beneath the Anatolian plate contrasts with the relatively uniform GPS observed westward motion of the Anatolian plate.

Within the Aegean Sea N-S oriented anisotropy conforms to observed N-S extension of the Aegean region (Mckenzie, 1978; Jackson, 1994). This suggests that the observed anisotropy orientations within the mantle of the Aegean are influenced by the dynamics of back-arc processes beneath the Aegean Sea.

The lack of simple and consistent correlation between plate motion and Pn anisotropy orientations possibly suggests that more complex processes seem to influence Pn anisotropy orientations within the mantle lid. These processes could include both crustal (nearby dominant tectonic stresses) and upper mantle deformation

(e.g. mantle flow). This interpretation is based on the following observations: (1) anisotropy orientations that appear to be localized in regions underlain by very low Pn velocity zones (e.g. the northern Aegean and the Isparta Angle), (2) anisotropy orientations along the easternmost segment of the NAF zone are possibly sampling a larger scale asthenospheric anomaly beneath thin to absent mantle lid, and (3) rapid anisotropy variations.

**ACKNOWLEDGMENTS**

The authors are grateful for the help and assistance of our colleagues E. Zor, R. Gok, T. Bekler, S. Kuleli, K. Al-Damegh, G. Brew, A. Calvert, C. Brindisi, and F. Gomez. Special thanks to T. Hearn for his help and assistance in using the Pn tomography code. We are thankful for the help of the federal and local governments of Turkey during the installation of our seismic network. We also acknowledge the very helpful field assistance provided by the engineers of the IRIS/PASSCAL Instrument Center at New Mexico Tech. This research is supported by the National Science Foundation (Grant No. EAR-9804780) and Bogazici University Research Fund (Grant No. 99T206).

**REFERENCES**

Anderson, D.L. 1961. Elastic wave propagation in layered anisotropic media. Journal of Geophysical Research, v. 66, p. 2953-2963.

Angelier, J., N. Lyberis, X.L. Pichon and P. Huchon 1982. The tectonic development of the Hellenic arc and the Sea of Crete: A synthesis. Tectonophysics, v. 86, p. 159-196.

Backus, G.E. 1965. Possible forms of seismic anisotropy of the uppermost mantle under oceans. Journal of Geophysical Research, v. 70, no. 14, p. 3429-3439.

Beghoul, N. and M. Barazangi 1990. Azimuthal anisotropy of velocity in the mantle lid beneath the Basin and Range Province. Nature, v. 348, no. 6301, p. 536-538.

Beghoul, N., M. Barazangi and B.L. Isacks 1993. Lithospheric structure of Tibet and western North America; mechanisms of uplift and a comparative study. Journal of Geophysical Research, v. 98, no. 2, p. 1997-2016.

Bozkurt, E. 2001. Neotectonics of Turkey - a synthesis. Geodinamica Acta : The Europian Journal of Geodynamics, v. 14, no. 1-3, p. 3-30.

Calvert, A., E. Sandvol, D. Seber, M. Barazangi, F. Vidal, G. Alguacil and N. Jabour 2000. Propagation of regional seismic phases (Lg and Sn) and Pn velocity structure along the Africa-Iberia plate boundary zone: tectonic implications. Geophysical Journal International, v. 142, p. 384-408.

Dewey, J.F., W.C. Pitman, W.B.F. Ryan and J. Bonnin 1973. Plate tectonics and the evolution of the Alpine system. Geological Society of America Bulletin, v. 84, p. 3137-3180.

Grand, S.P. 1990. A possible station bias in travel time measurement reported to ISC. Geophysical Research Letters, v. 17, p. 17-20.

Hearn, T.M. 1996. Anisotropic Pn tomography in the western United States. Journal of Geophysical Research, v. 101, no. B4, p. 8403-8414.

Hearn, T.M. 1999. Uppermost mantle velocities and anisotropy beneath Europe. Journal of Geophysical Research, v. 104, no. B7, p. 15,123-15,139.

Hearn, T.M. and J.F. Ni 1994. Pn velocities beneath continental collision zones: the Turkish-Iranian Plateau. Geophysical Journal International, v. 117, p. 273-283.

Hempton, M.R. 1982. The North Anatolian Fault and complexities of continental escape. Journal of Structural Geology, v. 4, p. 502-504.

Hempton, M.R. 1985. Structure and deformation history of Bitlis suture near lake Hazar, southeastern turkey. Bulletin of Geological Society of America, v. 96, p. 233-243.

Hempton, M.R. 1987. Constraints on Arabian plate motion and extensional history of the Red Sea. Tectonics, v. 6, no. 5, p. 687-705.

Ismail, W.B. and D. Mainprice 1998. An olivine database: An overview of upper mantle fabric and seismic anisotropy. Tectonophysics, v. 296, p. 145-157.

Jackson, J. 1994. Active tectonics of the Aegean region. Annual Review of Earth and Planetary Sciences, v. 22, p. 239-271.

Karato, S.-I. 1998. Seismic anisotropy in the deep mantle, boundary layers and the geometry of mantle convection. Pure and Applied Geophysics, v. 151, p. 565-587.

Keller, G.R., C. Prodehl, J. Mechie, K. Fuchs, M.A. Khan, P.K.H. Maguire, W.D. Mooney, U. Achauer, P.M. Davis, R.P. Meyer, L.W. Braile, I.O. Nyambok and G.A. Thompson 1994. The East African Rift system in the light of KRISP 90. Tectonophysics, v. 236, p. 465-483.

Kendall, J.-M. 2000. Seismic anisotropy in the boundary layers of the mantle. In S.-i. Karato, A.M. Forte, R.C. Liebermann, G. Masters and L. Stixrude (Eds.), Deep Earth Interior: Mineral physics and tomography from the atomic to the global scale, American Geophysical Union, Geophysical Monograph 117, p. 115-159.

Keskin, M., J.A. Pearce and J.G. Mitchell 1998. Volcano-stratigraphy and geochemistry of collision-related volcanism on the Erzurum-Kars Plateau, northeastern Turkey. Journal of Volcanology and Geothermal Research, v. 85, p. 355-404.

Kocyigit, A. and O. Erol 2001. A tectonic escape structure: Erciyes pull-apart basin, Kayseri, centarl Anatolia, Turkey. Geodinamica Acta, v. 14, no. 1-3, p. 133-145.

Le Pichon, X. and J. Angelier 1979. The Hellenic arc and trench system: A key to the neotectonic evolution of the eastern Mediterranean area. Tectonophysics, v. 60, p. 1-42.

Mainprice, D., G. Barruol and W.B. Ismail, Eds. (2000). The seismic anisotropy of the Earth's mantle: From single crystal to polycrystal. Earth's Deep Interior: Mantle physics and tomography from the atomic to the global scale, American Geophysical Union.

Mainprice, D. and A. Nicolas 1989. Development of shape and lattice preferred orientations: application to the seismic anisotropy of the lower crust. Journal of Structural Geology, v. 11, p. 175-189.

Makris, J. and R. Vees 1977. Crustal structure of the central Aegean Sea and the islands of Evia and Crete, obtained by refractional seismic experiments. J. Geophys., v. 42, p. 329-341.

McClusky, S., S. Balassanian, et al. 2000. Global positioning system constraints on plate kinematics and dynamics in the eastern Mediterranean and Caucasus. Journal of Geophysical Research, v. 105, no. 3, p. 5695-5719.

McKenzie, D. 1972. Active tectonics of the Mediterranean region. Geophysical Journal of the Royal Astronomical Society, v. 30, p. 109-185.

Mckenzie, D. 1978. Active tectonics of the Alpine-Himalayan belt: The Aegean Sea and surrounding regions. Geophys. J. R. Astron. Soc., v. 55, p. 217-254.

Menke, W.H. and P.G. Richards 1980. Crust-mantle whispering gallery phases: A deterministic model of teleseismic Pn wave propagation. Journal of Geophysical Research, v. 85, no. B10, p. 5416-5422.

Paige, C.C. and M.A. Saunders 1982. LSQR: Sparse linear equations and least squares problem. ACM Transactions on Mathematical Software, v. 8, no. 2, p. 195-209.

Sandvol, E., K. Al-Damegh, A. Calvert, D. Seber, M. Barazangi, R. Mohamad, R. Gok, N. Turkelli and C. Gurbuz 2001a. Tomographic imaging of Lg and Sn propagation in the Middle East. Pure and Applied Geophysics, v. 158, p. 1121-1163.

Sandvol, E., D. Seber, A. Al-Lazki, M. Barazangi, N. Turkelli, E. Zor, R. Gok, T. Bekler, G. Orgulu, H. Karabulut, C. Gurbuz, S. Kuleli and S. Bayraktutan 2001b. Crustal and upper mantle seismic velocity structure in eastern Anatolia: results from the eastern Turkey PASSCAL seismic experiment. Eos, Trans. Am. Geoph. Un, v. 82, no. 47.

Sato, H., I.S. Sacks and T. Murase 1989. The use of laboratory data for estimating temprature and partial melt fraction in the low velocity zone: Comparison with heat flow and electrical conductivity studies. Journal of Geophysical Research, v. 94, p. 5689-5704.

Savage, M.K. 1999. Seismic anisotropy and mantle deformation: What have we learned from shear wave splitting? Reviews of Geophysics, v. 37, no. 1, p. 65-106.

Sengor, A.M.C., N. Gorur and F. Sargolu 1985. Strike-slip faulting and related basin formation in zones of tectonic escape: Turkey as a case study. In K.T. Biddle and N. Christie-Blick (Eds.), Strike-slip faulting and basin formation, Society of Econ. Paleontol. Mineral. Special Publication, 37, p. 227-264.

Sengor, A.M.C. and Y. Yilmaz 1981. Tethyan evolution of Turkey: a plate tectonic approach. Tectonophysics, v. 75, p. 181-241.

Silver, P.G. and W.W. Chan 1988. Implication for continental structure and evolution from seismic anisotropy. Nature, v. 335, p. 34-39.

Smith, G.P. and G. Ekstrom 1999. A global study of Pn anisotropy beneath continents. Journal of Geophysical Research, v. 104, no. B1, p. 963-980.

Snyder, D. and M. Barazangi 1986. Deep crustal structure and flexure of the Arabian plate beneath the Zagros collisional mountain belt as inferred from gravity observations. Tectonics, v. 5, no. 3, p. 361-373.

Sonder, L.J. and P.C. England 1989. Effects of a temperature-dependent rheology on large-scale continental extension. Journal of Geophysical Research, v. 94, no. B6, p. 7603-7619.

Takin, M. 1972. Iranian Geology and continental drift in the Middle East. Nature, v. 235, p. 147-150.

Walker, D. 1977. High-frequency Pn phases observed in the Pacific at great distances. Science, v. 19, p. 257-259.

Yilmaz, Y. 1990. Comparison of young volcanic associations of western and eastern Anatolia formed under a compressional regime: a review. Journal of Volcanology and Geothermal Research, v. 44, p. 69-87.